



National Library
of Canada

Bibliothèque nationale
du Canada

Canadian Theses Service

Service des thèses canadiennes

Ottawa, Canada
K1A 0N4

NOTICE

The quality of this microform is heavily dependent upon the quality of the original thesis submitted for microfilming. Every effort has been made to ensure the highest quality of reproduction possible.

If pages are missing, contact the university which granted the degree.

Some pages may have indistinct print especially if the original pages were typed with a poor typewriter ribbon or if the university sent us an inferior photocopy.

Previously copyrighted materials (journal articles, published tests, etc.) are not filmed.

Reproduction in full or in part of this microform is governed by the Canadian Copyright Act, R.S.C. 1970, c. C-30.

AVIS

La qualité de cette microforme dépend grandement de la qualité de la thèse soumise au microfilmage. Nous avons tout fait pour assurer une qualité supérieure de reproduction.

S'il manque des pages, veuillez communiquer avec l'université qui a conféré le grade.

La qualité d'impression de certaines pages peut laisser à désirer, surtout si les pages originales ont été dactylographiées à l'aide d'un ruban usé ou si l'université nous a fait parvenir une photocopie de qualité inférieure.

Les documents qui font déjà l'objet d'un droit d'auteur (articles de revue, tests publiés, etc.) ne sont pas microfilmés.

La reproduction, même partielle, de cette microforme est soumise à la Loi canadienne sur le droit d'auteur, SRC 1970, c. C-30.

THE UNIVERSITY OF ALBERTA

QUANTIFICATION OF TRABECULAR BONE DENSITY USING SINGLE AND
DUAL ENERGY X-RAY COMPUTED TOMOGRAPHY

BY

SATYAPAL RATHEE

A THESIS

SUBMITTED TO THE FACULTY OF GRADUATE STUDIES AND RESEARCH
IN PARTIAL FULFILLMENT OF THE REQUIREMENTS FOR THE DEGREE OF
MASTER OF SCIENCE

IN

DEPARTMENT OF APPLIED SCIENCES IN MEDICINE

(Bio-medical Engineering)

EDMONTON, ALBERTA

FALL 1988

Permission has been granted to the National Library of Canada to microfilm this thesis and to lend or sell copies of the film.

The author (copyright owner) has reserved other publication rights, and neither the thesis nor extensive extracts from it may be printed or otherwise reproduced without his/her written permission.

L'autorisation a été accordée à la Bibliothèque nationale du Canada de microfilmer cette thèse et de prêter ou de vendre des exemplaires du film.

L'auteur (titulaire du droit d'auteur) se réserve les autres droits de publication; ni la thèse ni de longs extraits de celle-ci ne doivent être imprimés ou autrement reproduits sans son autorisation écrite.

ISBN 0-315-45775-9

THE UNIVERSITY OF ALBERTA
RELEASE FORM

NAME OF AUTHOR

SATYAPAL RATHEE

TITLE OF THESIS

QUANTIFICATION OF TRABECULAR
BONE DENSITY USING SINGLE AND
DUAL ENERGY X-RAY COMPUTED
TOMOGRAPHY

DEGREE FOR WHICH

THESIS WAS PRESENTED

MASTER OF SCIENCE

YEAR THIS DEGREE GRANTED

FALL 1988

Permission is hereby granted to THE UNIVERSITY OF ALBERTA
LIBRARY to reproduce single copies of this thesis and to lend or sell such copies of this
thesis for private, scholarly, or scientific research purposes only

The author reserves other publication rights, and neither the thesis nor
extensive extracts from it may be printed or otherwise reproduced without the author's
written permission.

(SIGNED) *Satyapal*

PERMANENT ADDRESS

1004 Lake Wood Road North

Edmonton, Alberta

T6K 3C1

Dated.. *Oct 18*, 1988.

THE UNIVERSITY OF ALBERTA
FACULTY OF GRADUATE STUDIES AND RESEARCH

The undersigned certify that they have read, and recommend to the Faculty of Graduate Studies and Research, for acceptance a thesis entitled QUANTIFICATION OF TRABECULAR BONE DENSITY USING SINGLE AND DUAL ENERGY X-RAY COMPUTED TOMOGRAPHY submitted by SATYAPAL RATHEE in partial fulfillment of the requirements for the degree of MASTER OF SCIENCE in APPLIED SCIENCES IN MEDICINE (Bio-medical Engineering).

W. Mount

Supervisor

Donald McLean

J. J. Koles

J. F. Flynn

DATED...Oct 14,.....1988

Abstract

The importance of bone mass measurements for the early detection and in treatment monitoring of osteoporosis is now well accepted. Computed Tomography (CT) is the preferred method for measuring bone mass since cortical and trabecular bone density can be separately quantitated with good precision and accuracy.

A special purpose X-ray fan-beam computed tomography scanner (X-CT), designed and constructed in this department, represents a significant technological advance for the non-invasive measurement of trabecular bone density for skeletal diagnosis and treatment monitoring. This thesis describes the calibration procedure developed for this scanner system, and the implementation of both single and dual energy approaches to the quantification of trabecular bone density, *in-vivo*, and *in-vitro*.

Data acquisition and scanner control for calibration and image data collection for the X-CT system use a VAX 11/750 minicomputer connected through a Computer Automated Measurement and Control (CAMAC) system and TMS9900-based microcomputer. The photon detection system which consists of 26 PMT/NaI(Tl) detectors, used in the photon counting mode, is calibrated for spectral matching, deadtime and beam hardening at X-ray tube potentials of 50kV and 80kV. The geometrical parameters for the fan-beam, such as source to center-of-rotation distance and detector angles, which are required for the image reconstruction process, are experimentally determined. Data collected in multiple 360° rotations of the linearly shifted, asymmetric fan-beam is reordered into a parallel beam format. The number of data points in a reordered parallel projection is determined by the number of rotations of the scanner. After reordering, a parallel beam, filtered back-projection method is used for image reconstruction. Due to the variable source to center-of-rotation distance, the X-CT scanner can be used to provide high resolution, 2-dimensional images of objects of diameter from 75mm to 220mm.

Procedures for high precision measurements of trabecular bone density have been

implemented on the X-CT scanner. These include: a method for precisely reproducing the axial measurement site in a bone using a digital radiograph, and an automatic algorithm for detecting the outer contour of cortical bone. These procedures help to precisely reproduce the measured bone volume in order to reduce errors resulting from the axial and transaxial variations in the distribution of trabecular bone.

Both single and dual energy scanning methods are possible with the X-CT scanner. The single energy method provides good measurement precision ($\pm 0.12\%$, *in-vitro* at 50kV) but is influenced by fat content in the measured bone volume. The dual energy method greatly improves the accuracy of the bone density measurement when unknown amounts of fat are present in measured volume. However, the increase in accuracy is offset by a decrease in precision.

Two approaches to dual energy scanning are presented: the pre-processing and the post-processing methods. Implementation of the pre-processing method makes it possible to unambiguously separate bone and soft tissue in bone cross-sections. Calibration methods for the pre-processing approach, and a fast bone and soft tissue reconstruction algorithm based on isotransmission lines have been developed and implemented. The post-processing dual energy method works with reconstructed images of the bone cross-sections at the two photon energies. This method provides separate measurements of the concentrations of the mineral and non-mineral parts of trabecular bone using two independently measured linear attenuation coefficients given by the pixel values in the two images. This procedure has been implemented to determine trabecular bone density from 50kV and 80kV images of bone.

Overall performance of the X-CT scanner, particularly with respect to accuracy and precision of bone mass measurement, *in-vitro*, and, *in-vivo*, has been evaluated.

Experimental verification of the improvements offered by the dual energy method to reduce the fat induced errors in the measurement of trabecular bone mass is presented, where measurements were made for standard solutions, and for cadaver femurs. The beam

hardening errors due to variable quantities of soft tissue surrounding the bone, are established by measuring appropriate experimental phantoms. Scattering and exponential edge gradient errors are also studied with standard solutions in other experimental phantoms.

The contributions of pixel noise, and of repositioning errors in the bone measurement volume to the overall precision of the measurement of bone mass, have been determined from repeated measurements of a standard K_2HPO_4 solution (c.v. 0.12%), and of the distal site of a cadaver femur (c.v. 0.67%), under the normal measurement conditions of the scanner. The standard error in the pixel values of the single and pre-processing images is determined for a number of scanner rotational angles.

Acknowledgements

I wish to thank my supervisor Dr. T. R. Overton for his guidance and support throughout this project, and also for reviewing this thesis. I have gained much from his experience in scientific research and writing.

I owe much debt to Dr. B. McClean who guided me through this project and assisted with most of the experiments.

A special thanks to Mr. R. Heath, Mr. R. Morse, Mr E. Haska and Mr. Narc Oullette for their assistance in frequent instrumental and software problems.

I would also like to thank my colleagues in this department who helped me various ways both scientifically and socially.

Financial support provided by the Alberta Heritage Foundation for Medical Research in the form of a studentship is gratefully acknowledged.

TABLE OF CONTENTS

CHAPTER		PAGE
1.	Introduction	1
2.	Background	6
2.1	Radiological Techniques of Bone Mass Measurement	6
2.1.1	Radiogrammetry	6
2.1.2	Photodensitometry	7
2.1.3	Single Photon Absorptiometry	8
2.1.4	Dual Photon Absorptiometry	9
2.1.5	Compton Scattering	9
2.1.6	Neutron Activation	10
2.1.7	Computed Tomography	11
2.1.7.1	Measurement of Bone Density using Commercial CT	12
2.1.7.2	Special Purpose Scanners for Measuring Bone Density	13
2.1.8	Radiological Analysis of Bone and Bone Biology	13
2.2	Bone Biology	14
2.2.1	Composition and Structure of Bone	14
2.2.2	Growth of Bone	16
2.2.3	Remodeling of Bone	16
2.2.3.1	Classification of Bone Disorders	19
2.2.3.2	Effects of Bone Composition and BMU-based Remodeling on Radiological Bone Assessment	20
3.	Fan-beam X-ray CT scanner for Quantitative Bone Density Measurement	22
3.1	System Description	24

3.1.1	X-ray Tube and High Voltage Generation	24
3.1.2	Photon Detection System	25
3.1.3	VAX and CAMAC Interface	26
3.1.4	Microcomputer and Scanner Control	27
3.1.4.1	Scanner Reset Position	28
3.1.4.2	Motor Movements in Data Collection	30
3.2	System Calibrations	30
3.2.1	X-ray Spectrum Matching	31
3.2.2	Deadtime Calibrations	34
3.2.3	Background Noise	36
3.2.4	Beam Hardening Calibrations	38
3.2.5	Centering Fan-beam	40
3.2.6	Geometric Calibrations	42
3.3	Data Collection and Image Reconstruction	47
3.3.1	Data Collection	47
3.3.2	Image Reconstruction	55
4.	Analysis Procedures for High Precision Measurement of TBD using CT	58
4.1	Reproducibility of Measurement Site	58
4.2	Reproducibility of Measurement Area	61
4.2.1	Bone Contour Detection	61
4.2.1.1	Pre-Bone Find	63
4.2.1.2	Auto-Bone Find	63
4.2.1.3	Post-Bone Find	67
4.3	TBD Analysis	69
5.	Methods for Bone Mass Measurement using CT	71

5.1	Single Energy Method for Bone Mass Measurement by CT (SECT)	71
5.1.1	Volume Fractions Method	71
5.1.2	Concentration Method	73
5.1.3	Calibration for K_2HPO_4 Solutions	76
5.2	Dual Energy Method for Bone Mass Measurement by CT (DECT)	79
5.2.1	Post-processing Method	80
5.2.1.1	Theoretical Considerations for Dual Energy CT	80
5.2.1.2	Procedure for Bone Mass Measurement	82
5.2.2	Pre-processing Method	82
5.2.2.1	Theoretical Considerations for Pre-processing Method	83
5.2.2.2	Procedures	85
5.2.2.2(a)	Conventional Approach	87
5.2.2.2(b)	Isotransmission Line Approach	88
5.2.2.2(b.1)	Isotransmission Line Calibrations	90
5.2.2.3	Bone and Soft Tissue Decomposition	95
5.2.2.4	TBD Measurement	99
6.	Performance of X-ray CT Scanner for TBD Measurement	101
6.1	Accuracy	101
6.1.1	Variable Fraction Fat Content	102
6.1.2	Beam Hardening	105
6.1.3	Scattering and Exponential Edge Gradient Effect	107
6.2	Precision	112
6.2.1	Precision of Linear Attenuation Coefficient	113
6.2.2	Comparison of Dual Energy Methods	115
6.2.3	Repositioning Errors	116
6.3	Results	119

6.3.1	Cadaver Femur Measurements	119
6.3.2	<i>In-vivo</i> Measurements	122
7.	Discussion	124
7.1	Scanner Performance	124
7.2	Accuracy	125
7.3	Precision	128
7.4	Cadaver Femur	129
8	Conclusions and Future Developments	131
8.1	Conclusions	131
8.2	Future Developments	132
8.2.1	Dual Energy Beam	134
8.2.2	Alternative Detectors and Data Acquisition System	134
9	References	136

List of Tables

Table No	Title	Page
5.2.1	Accuracy of basis decomposition	85
5.2.2	Calibration table for logarithmic attenuations at 50kV, 2.3mA.	91
5.2.3	Calibration table for logarithmic attenuations at 80kV, 1.75mA	92
6.1.1	Percentage errors in 50kV, 80kV, aluminum equivalent and monoenergetic images of beam hardening phantom for 150mg/ml K_2HPO_4 solution in the aluminum cylinder.	107
6.1.2	Scattering errors in 50kV, 80kV and aluminum equivalent images of constant internal diameter phantom for water in the aluminum cylinder.	109
6.1.3	Scattering errors in 50kV, 80kV and aluminum equivalent images of constant internal diameter phantom for K_2HPO_4 solution in the aluminum cylinder.	110
6.1.4	Simulated errors due to EEGE for water in the aluminum cylinder of constant internal diameter phantom at various photon energies and in aluminum equivalent images.	110
6.2.1	Percentage standard error in pixel value of a 100mg/ml K_2HPO_4 solution for various scanner speeds in 50kV, 80kV and aluminum equivalent images.	114
6.2.2	Coefficient of variation in pixel value of 200mg/ml K_2HPO_4 solution in 50kV, 80kV and aluminum images.	115
6.2.3	Standard error in measured concentration of a 100mg/ml K_2HPO_4 solution by pre- and post-processing DECT methods at various scanner speeds.	116

6.2.4	Volumetric TBD for six measurements at the distal femur site of a cadaver bone.	117
6.3.1	TBD measured at the distal femur, the proximal femur and the femoral neck sites of two cadaver bones using SECT (50kV, 80kV) and DECT (pre- and post-processing) methods.	121
6.3.2	TBD measured at the distal femur and the proximal tibia sites of two normal subjects using 50kV, SECT method.	122

List of Figures

Figure No	Title	Page
2.1	Bone remodeling.	17
3.1.1	System schematic of X-ray CT scanner.	23
3.2.1	Measured differential spectrum as a function of discriminator threshold level for (a) 50kV and (b) 80kV.	33
3.2.2	The observed counts as a function of X-ray tube current for experimental, paralyzable and non-paralyzable models.	35
3.2.3	Image of aluminum ring phantom with artifacts due to imperfect deadtime corrections.	37
3.2.4	Image of aluminum ring phantom without deadtime artifacts.	37
3.2.5	Logarithmic attenuation as a function of number of aluminum and plexiglass sandwiches (corrected and observed).	40
3.2.6	Geometric considerations of fan-beam centering.	41
3.2.7	Geometric considerations of determining SCR distance and detector angles.	43
3.3.1	Symmetrical and asymmetrical fan-beam, rotated from the reset position.	49
3.3.2	(a)- Filling of sample space for symmetrical fan-beam. (b)- Filling of sample space for asymmetrical fan-beam.	51
3.3.3	(a)- Asymmetrical and linearly shifted asymmetrical fan-beams, rotated from the reset position. (b) Filling of sample space for two 360° rotations of asymmetrical fan-beam.	52 53
3.3.4	Equivalent linear shifts for a rotation of detectors about	

	the source.	54
4.1.1	Variations in trabecular bone density and the bone area as a function of axial position at the distal femur site.	59
4.1.2	Digital radiograph over the distal femur and the proximal tibia.	60
4.2.1	CT image at the distal femur site of a normal male.	65
4.2.2	CT image at the proximal tibia site of a normal male	65
4.2.3	(a) A correlation kernel for cross-correlating radial profiles.	66
	(b) A radial profile from the CT image of a cadaver femur at the distal site.	67
	(c) The correlation function resulting from the cross-correlation of (a) and (b).	67
4.2.4	Image of figure 4.2.1 with cortical bone contour outlined.	68
4.2.5	Image of figure 4.2.2 with cortical contour for tibia bone outlined.	68
5.1.1	Constant internal diameter phantom (side view).	76
5.1.2	(a) A calibration line of pixel value as a function of the concentration of K_2HPO_4 solution at 50kV.	77
	(b) A calibration line of pixel value as a function of the concentration of K_2HPO_4 solution at 80kV.	77
5.2.1	Isotransmission line at 30keV for constant $T_{30keV} = 3.0$.	89
5.2.2	Flowgraph of isotransmission line calibrations.	93
5.2.3	Isotransmission lines at 50kV for constants	
	(a) $T_{50kV} = 1.10$ and (b) $T_{50kV} = 3.50$	96
5.2.4	(a) 50kV image of a cadaver femur at distal site	97
	(b) 80kV image of a cadaver femur at distal site	97

	(c) Bone equivalent CT image resulting from basis decomposition of (a) and (b)	98
	(d) Soft tissue equivalent CT image resulting from basis decomposition of (a) and (b)	98
5.2.5	A calibration line of pixel value of bone equivalent images of K_2HPO_4 solution as a function of its concentration.	100
6.1.1	Effect of adding ethyl alcohol to a 100mg/ml K_2HPO_4 solution on its mineral concentration measured by SECT (50kV, 80kV) and DECT (post-processing). Illustration of the effect of fat on measured trabecular bone density.	104
6.1.2	Effect of adding ethyl alcohol to a 100mg/ml K_2HPO_4 solution on its mineral concentration measured by SECT (50kV, 80kV) and DECT (pre-processing). Illustration of the effect of fat on measured bone density.	104
6.1.3	Beam hardening phantom (side view).	106
6.2.1	Digital radiograph over the distal site of a cadaver femur.	118
6.3.1	Digital radiograph over the proximal site of a cadaver femur.	120
6.3.2	Digital radiograph over the femoral neck site of a cadaver femur.	120

List of Abbreviations

CT	Computed Tomography
TBD	Trabecular Bone Density
SPA	Single Photon Absorptiometry
DPA	Dual Photon Absorptiometry
CS	Compton Scattering
NA	Neutron Activation
BSU	Basic Structural Unit
BMU	Basic Multicellular Unit
PMT	Photomultiplier Tube
CAMAC	Computer Automated Measurement and Control
IGOR	Input Gate/ Output Register
DC	Direct Current
VAX	Virtual Address Extension
PSC	Programmable Supply Controller
SCR	Source to Center-of-rotation
CPU	Central Processing Unit
I/O	Input/ Output
keV	Kilo Electron Volts
kV	Kilo Volts
BOFI	Bone Find
EDCORP	Edge Detection by Cross-correlation of Radial Profiles
SECT	Single Energy Computed Tomography
DECT	Dual Energy Computed Tomography
EEGE	Exponential Edge Gradient Effect

1.0 Introduction

For more than a century the human skeleton has been known to be both a framework for mechanical support and movement of the body, and a mineral storehouse for physiological needs. During the past 10-15 years, however, the human skeleton has become recognized as a complex organ, as distinct from its role merely as a structure.

A considerable body of evidence has now been accumulated demonstrating that the strength of bone tissue bears a close relationship to its mineral content [Bentzen et al., 1987; Ciarelli et al., 1986; Grag and Walker, 1986; McBroom et al., 1985]. New techniques for evaluating and monitoring skeletal status, through bone mineral measurement, have evolved along with the increase in biological knowledge about the skeleton. This new technology is able to measure small, *in-vivo*, changes in bone mass over time with good precision and accuracy. However, in order to investigate the effects of pharmacologic agents on the skeleton in the search for an effective treatment for a major skeletal disease- osteoporosis- even smaller changes in bone mass need to be determined with better precision and with a lower risk to the patient. The purpose of this thesis is the development of a new technology for skeletal assessment-- a special purpose X-ray computed tomography system (X-CT)-- and its application to the measurement of bone density, *in-vivo*, and *in-vitro*.

The discovery of X-rays in 1895 by Röntgen and theoretical studies of Radon in 1917 concerning the solution of gravitation equations by 'inversion formulae' provided the basic knowledge for the eventual development of computed tomography. In an independent restatement of the inversion theorem of Radon, Bracewell [Bracewell, 1956] developed methods for the reconstruction of microwave sources from their signals received on earth by antenna arrays which proved useful for the subsequent application of these techniques to reconstructive tomography. A major development in X-ray computed tomography (CT) occurred with the work of Cormack [Cormack, 1963; Cormack, 1964] which involved

theoretical and experimental studies of radiation transmission projections, and the reconstruction of a transaxial image of an object from these projections. At that time, however, Cormack was not able to implement his ideas for practical applications due to a lack of the computational power needed for data analysis. Hounsfield started his independent CT research early in the 1960's, and he produced the first commercial CT scanner -- the EMI CT -- in 1971 [Hounsfield, 1973]. Hounsfield and Cormack shared the 1973 Nobel Prize in medicine and physiology for their respective pioneering contributions to this revolutionary radiologic imaging development.

Since the development of the original EMI head scanner CT technology has evolved rapidly to the present such that precise, accurate and rapid measurements of linear attenuation coefficients in a two dimensional cross-section of an object are now routinely available. The technical applications of CT scanners are now wide-spread, making use of quantitative as well as qualitative information in the CT images. Currently the most important application of qualitative CT is for high contrast resolution visualization of anatomical structures for diagnostic purposes. Quantitative applications of CT scanners include: radiation therapy planning [McCullough, 1981]; blood flow measurements [Berninger and Redington, 1981]; functional surgery [Greitz and Bergström, 1981], and bone mineral analysis [Rüegsegger et al., 1974]. In radiation therapy quantitative CT images of a part of the body containing a tumor are used to generate isodose curves for field size definition in radiation therapy, and for subsequent follow-up of the efficacy of treatment procedures. CT scanners with very short scan times (<5seconds) also provide dynamic measures of the passage of an iodinated contrast medium through an organ for blood flow measurements. By applying stereotactic procedures to CT images geometrical information about small anatomical structures is obtained which is useful for functional surgery.

Quantitative measurement of bone mineral content, *in-vivo*, is a recent, very important application of CT. The human skeleton has the dual function of providing

mechanical support to the body and calcium storage; it is adapted to mechanical usage through regulation of its structural and material properties. After skeletal maturity, these adaptation properties are dynamically preserved through continuous skeletal renewal, a process known as "remodeling" [Frost, 1986]. The skeleton is constructed from many different bones, and each bone has several component parts. The outer shell of most bones is the cortical (or compact) bone which has an outer, periosteal surface and an inner, cortical-endosteal surface. The cortical bone contains Haversian systems which are interconnected through a vast system of communicating channels (the Volkmann's canals and the canaliculae) containing blood vessels and nutrient fluids. Within the volume contained by the cortical shell trabecular or 'spongy' bone is distributed along with hematopoietic and fatty marrow. In the appendicular skeleton trabecular bone lies mainly at the distal and proximal ends of the long bones, while it is generally uniformly distributed in the bones of the axial skeleton.

Osteoporosis and osteomalacia are two important bone disorders. Osteoporosis is the commonest bone dysfunction, particularly affecting post-menopausal women. It results from an increased loss of bone due to an imbalance between resorption and formation in the bone remodeling process. Osteomalacia is the result of a mineralizing defect in bone. As a result of these bone disorders, and of the normal aging process, bone loss occurs for all individuals after about 35 years of age. This bone loss is more prominent on the cortico-endosteal and trabecular bone surfaces than on the cortical Haversian and periosteal surfaces. Trabecular bone has a large surface area in contact with the marrow which contains metabolically active body fluids. Thus a larger bone loss, and also an increased sensitivity to disease and to therapy is seen for trabecular bone. Trabecular bone mineral content is thus a sensitive indicator of skeletal status.

There are a number of problems associated with the precise and accurate measurement of trabecular bone mineral content. The measurement only of trabecular bone requires the spatial separation of the cortical bone from the trabecular bone and the

surrounding soft tissue. The spatial variations in distribution of trabecular bone also require the analysis of a precisely reproducible volume of trabecular bone in serial studies. Among the radiological techniques (section 2.1) for measuring bone mineral content only the CT method can provide spatial separation between cortical and trabecular bone. However, a CT scanner capable of measuring trabecular bone mineral content with good precision must have special features including: very good spatial and contrast resolutions in bone images; reasonably short scan time to reduce errors due to patient movement, and a very low radiation dose to the subject. These features are generally not available in commercial CT scanners. In addition, corrections for non-linear detector response, beam hardening and scattering must be carried out for accurate quantitative measurement of trabecular bone mineral content by CT. The presence of variable amounts of fat in the trabecular bone space can also cause serious errors in single energy CT methods. Dual energy CT methods (pre- and post-processing) have been developed which reduce such errors.

The X-CT scanner described in this thesis is a multiple rotation device which uses 5 sequential, 360° rotations of a linearly shifted, asymmetric fan-beam to improve limited spatial resolution. Another important design feature of the X-CT scanner is its variable source to center-of-rotation (SCR) distance which provides the same physical, spatial resolution for different object sizes.

A brief description of the hardware and software implementations for the major sub-systems (X-ray generation, data acquisition, computer and control) of this scanner is given in section 3.1. The theory and the experimental procedures for detector system calibrations (spectral matching, deadtime and beam hardening corrections), and the geometric calibrations such as fan-beam centering, and evaluation of geometric parameters for the fan-beam are outlined in section 3.2. An analysis of the unique data collection procedure and an outline of the methods for reordering the fan-beam radiation transmission projections into a parallel beam format is given in section 3.3. Section 3.3 also illustrates the principle of achieving a variable spatial resolution by varying the number of scanner

rotations in the data collection procedure.

Good precision in the measurement of trabecular bone mineral content is possible only if a precisely reproduced volume of bone is measured and analyzed. For the X-CT scanner the procedures for repositioning the measured bone volume and for optimization of the CT images of bone to determine its volume averaged mineral content are presented in section 4.

The pixel values of the X-CT images represent the relative linear attenuation coefficients within the cross-section of bone; these pixel values are directly related to the mineral content of bone. The relationship between trabecular bone mineral content and the pixel values in X-CT images, assuming a two component (single energy method) and a three component model (pre- and post-processing dual energy methods) of trabecular bone are analyzed in section 5. The performance of this X-CT scanner with respect to the factors affecting accuracy and precision in clinical bone mass measurements is established through experimental and theoretical studies and these are described in section 6.

In order to better appreciate the significance of the X-CT scanner for measurement of trabecular bone density (TBD) a brief background of several other skeletal assessment methods precedes the description of the scanner.

2.0 Background

2.1 Radiological Techniques of Bone Mass Measurement

There are several techniques currently available for bone mass measurement using ionizing radiation. The clinical importance of a bone mass measurement method can be established in terms of its accuracy, precision and sensitivity to changes in bone mass, the radiation dose received by a patient, and the cost of the equipment. The accuracy of the bone mass measurement technique is the true representation of the quantity of bone tissue present in a measured volume. Precision is associated with variations between independent measurements of the same quantity of bone. The sensitivity of these methods can be defined in terms of the measured changes in bone mass relative to the real changes in the quantity of bone in the measured volume. The radiation dose given to the subject is also a very important consideration in longitudinal studies.

In general the most suitable measurement techniques are those which can separately measure the density of trabecular and cortical bone. Since trabecular bone turnover and its response to therapeutic intervention is much larger than that of cortical bone, changes in TBD can be measured with a higher precision and can be used as a sensitive indicator of skeletal response.

The various techniques for skeletal assessment are briefly discussed in the following sections.

2.1.1 Radiogrammetry

Radiogrammetry is the simplest of the quantitative radiological techniques for skeletal assessment. Increased cortico-endosteal resorption results in reduced cortical thickness in the appendicular skeleton. In the axial skeleton osteopenia- a state of reduced bone volume- is characterized by geometrically deformed vertebrae. Radiogrammetry

involves the evaluation of geometrical parameters such as cortical thickness relative to bone width, cross-sectional area of bone, and wedge angles of compressed vertebrae. High quality radiographs of particular bones are taken and the geometrical parameters measured from these films using a micrometer. In particular diseases resorption tunnels within the cortex can be seen in a magnified radiograph of the bone and this feature used as an additional indicator of skeletal status.

Considerable care must be taken in selecting and reproducing the site of cortical bone measurement. The results are normalized to bone width to compensate for variations in body size. The minimum level of cortical thinning that can be detected with this technique usually occurs only in advanced stages of bone disorders. The technique is therefore not suitable for identification of population at risk with respect to osteoporosis due to the relatively small changes in cortical bone thickness. The precision of the measurement of vertebral dimensions is $\pm 3.2\%$ [Riggs et al., 1982], and of the metacarpal cortical index (ratio of combined cortical thickness and total bone diameter) from ± 1.3 to $\pm 3.1\%$ [Dequeker, 1917].

2.1.2 Photodensitometry

Photodensitometry was the first approach to quantitative bone mass measurement. The underlying principle of this method is that the optical density of a radiograph has a fixed relationship to the number of X-ray photons detected, and consequently to the amount and type of material present in the beam path. The optical density corresponding to a particular beam path through the bone referenced to that of a calibration material is known as a projection point. The projection points along a line across the bone are summed for a slice thickness of 1cm to express the bone mass in units of gm/cm.

As the optical density of the bone image is dependent upon the amount of soft tissue in front of and behind the bone, some means must be found to correct for this. A water bath surrounds the bone and a radiograph is obtained with carefully controlled X-ray tube

voltage and current, film exposure and development. The radiation dose given to the subject is the same as for a normal radiograph. The precision of measurement is $\pm 4.7\%$ for metacarpal and $\pm 8\%$ for ulna [Shimmins et al., 1972; Cameron et al., 1963]. A small change in the trabecular bone mass cannot be detected with good precision because cortical bone mass is also included in the measurements.

2.1.3 Single Photon Absorptiometry (SPA)

In this technique photons transmitted through an object in a well collimated beam are counted as the photon source and detector assembly are moved across the object. The problems associated with film in photodensitometry are eliminated, and a calibration wedge is not required to be scanned with the object due to the inherent stability of the detector system. The most commonly used photon sources are ^{125}I and ^{241}Am with effective energies 29keV and 60keV respectively. The soft tissue compensation involves immersing the limb in a water bath. The results are expressed in gm/cm, as in photodensitometry, and can be normalized to the width of bone (gm/cm^2).

SPA can be used to measure appendicular sites where significant amounts of trabecular bone are present, e.g. distal radius, femur and proximal tibia. However, since bone mass changes very rapidly with axial position at these sites, repositioning errors can be very large thus giving a poor measurement precision for bone mass changes. Repositioning errors can be considerably smaller at the midshaft of the long bones where only uniform cortical bone is present. The precision of measurement for the radial diaphysis can vary from $\pm 1.4\%$ to $\pm 7.6\%$ [Hangartner, 1986] depending upon the repositioning errors and the site of measurement. SPA delivers a very low radiation dose (0.02mSv) to a small measurement area, and if the repositioning errors are controlled this technique can be a useful tool in the in-vivo study of bone mass. The accuracy of the measured mineral content is affected by variations in the amount of fat present in bone marrow and is between 5 to 6% [Cameron et al., 1968].

2.1.4 Dual Photon Absorptiometry (DPA)

The soft tissue compensation required in photodensitometry and SPA cannot be made in case of vertebral bone mass measurements due to unknown amounts of air present in lungs, stomach and bowel. In principle this problem is solved by using a dual energy source such as ^{153}Gd (44keV, 100keV) for measuring the projection at two energies. The data can then be analyzed to separately give the amount of bone and soft tissue, expressed in gm/cm^2 . The radiation dose delivered with this technique is very small (0.005-0.015 mSv) and is distributed over a large abdominal area for a spine measurement [Peppler and Mazess, 1981]. The accuracy of the technique is better than that of the SPA due to the use of two photon energies to compensate for variable soft tissue. However, the variable amount of fat present in bone marrow still causes an inaccuracy in the measured results. The precision and accuracy of the bone mass measurement has been quoted at $\pm 2.5\%$ and $\pm 4\%$ respectively [Peppler and Mazess, 1981]. Bone mineral content measurement in the lumbar spine (which contains a large amount of trabecular bone) is very sensitive to changes in skeletal status. Therefore, DPA can be used to detect and monitor osteopenia by measuring the changes in the vertebral bone mass.

2.1.5 Compton Scattering Technique (CS)

Measuring bone density by CS involves the use of two orthogonal photon beams. After the count rates of two photon beams through the object into two detectors have been measured, the apparatus is rotated through 180° and another set of readings is taken. These count rates allow computation of the physical density of the scattering volume. The number of scattered photons is proportional to the number of electrons in a given volume of a particular biological material, which in turn is proportional to the physical density of that material. Therefore, the density measurements include contributions from the organic and

the inorganic components of bone. An advantage of this technique is that the scattering volume can be located entirely within the trabecular bone. The practical limitations of high dose (1.6mSv) to the peripheral measurement site (calcaneus) [Kennett and Webber, 1976] and long scan time restrict the CS method application to measurement of a relatively large volume of bone. Since the repositioning of the scattering volume is relatively simple, the precision of the measurement is largely determined by the radiation dose. The precision of calcaneus bone mass measurement has been reported to be $\pm 1.5\%$ [Webber and Kennett, 1976].

There are several problems associated with the CS technique of bone mass measurement. One of the major problems with this technique is that the photons undergo multiple scattering. The number of multiply scattered photons can be calculated by Monte Carlo simulation of Compton scattering interactions of photons within a calibration phantom [Battista and Bronskill, 1978]. However, these calculations may not be valid if the bone under study differs from the calibration standard. Compton scattering densitometers are available for clinical use only in a few research centers.

2.1.6 Neutron Activation (NA)

Bone mineral mass measurement by NA involves the irradiation, with neutrons, of a body, in part or in whole. Neutrons are available from reactors, accelerators or radioisotope sources (^{252}Cf , ^{238}Pu -Be, ^{241}Am -Be). Neutron irradiation of bone converts ^{48}Ca into ^{49}Ca which emits photons at 3.1 MeV which can then be counted by scintillation detectors. Since the amount of ^{49}Ca produced is proportional to total amount of calcium in an irradiated body volume, and because 99% of the calcium is concentrated in bone, the amount of ^{49}Ca present is a good estimate of the amount of bone in the body part under consideration.

The precision of these measurement varies from $\pm 2\%$ to $\pm 7\%$ depending upon the body size; the radiation dose can be as high as 50 mSV delivered to the torso [Catto et al.,

1973]. Due to the problems of reproducibility and the influence of the size of skeleton, neutron activation remains a research tool.

2.1.7 Computed Tomography (CT)

CT offers major advantages for bone density measurement over other techniques:

(1) A CT image is a two dimensional distribution of average linear attenuation coefficients of material present in small volume elements within the cross-section of bone. A number of CT images taken axially along a bone can be arranged to construct a three dimensional map of the linear attenuation coefficient for a given volume of bone. Thus volumetric density of bone (gm/cm^3) can be measured.

(2) The cortical bone can be separated from the trabecular bone in the CT image and a volume containing only trabecular bone can be used in the analysis to obtain the average TBD value.

(3) The volume of bone for density analysis can be precisely reproduced with the help of digital radiograph and automatic cortical bone contour detection (see sections 3.2 and 3.3).

The technological improvements in terms of digital computers, data acquisition systems and scanner geometry have had a major impact in the field of CT. In the earliest, first generation CT scanners a single detector was utilized to measure the transmitted number of photons from a highly collimated X-ray beam as the source-detector assembly was translated across the object. In order to obtain the attenuation profiles at a number of angular positions around the object, the source-detector assembly had to be rotated and translated many times. This resulted in longer (5 to 10 minutes) scan times and large radiation doses. In second generation CT scanners, the pencil beam was replaced by a fan-beam with a number of detectors arranged in the fan. The source-detector assembly was translated across the object to obtain the attenuation profiles for a number of angular

positions depending upon the number and inter-detector angular spacing of the detectors. A considerable reduction in scan time (typical scan time of 2-3 minutes) resulted due to the smaller number of translations and rotations required to obtain a sufficient number of attenuation profiles. In third generation scanners, the translate-rotate scanning geometry is replaced by a rotate-rotate sequence. A large number of detectors (typically 300-700) are arranged in a wider fan-beam, and data collection involves a 360° rotation of the source-detector assembly around the object resulting in very small scan times (1-10 seconds). Fourth and fifth generation scanners further reduce the scan time by eliminating the need to rotate the bulky detector assembly of the third generation scanners. Fourth generation systems consist of a fixed 360° detector ring with only the source rotating. Fifth generation systems have both the source and the detectors stationary; such scanners are very complex and have high cost, however the scan times are extremely fast (fractions of a second).

2.1.7.1 Measurement of Bone Density using Commercial Scanners

Commercially available CT scanners can be used for bone mineral analysis if appropriate corrections for beam hardening and scattering are made for the projection data. These scanners have been extensively used for vertebral bone mineral content measurements [Goodsitt and Rosenthal, 1987; Laval-Jeantet et al., 1986; Cann and Genant, 1980; Genant and Boyd, 1977]. The patient is scanned along with calibration solutions obtaining a number of slices covering L1 to L4 lumbar vertebrae. A region of interest within the vertebral bodies is analyzed to give the bone density in terms of the standard solutions. However, commercially available scanners have a number of problems with respect to bone mineral measurement and analysis.

(1) The precision of bone mass measurement is poor because the bone occupies a small area of an image.

(2) Since skeletal treatment requires repeated bone measurements at the same skeletal site, the radiation dose for a study has to be a minimum. A larger patient dose

(>10mSv) is usually associated with commercially available CT scanners than for other bone measurement methods.

(3) The commercial CT scanners use a relatively high X-ray tube potential with an effective energy of more than 40 keV, thereby decreasing the sensitivity and precision to changes in bone density [Müller et al., 1985]. Moreover, the problems associated with marrow fat are enhanced at higher photon energies.

2.1.7.2 Special Purpose CT Scanners for Measurement of Bone Density

Spinal bone density is a very important parameter for differentiating the osteopenic from the normal skeleton, and it is well correlated to the bone density measured at the appendicular sites [Schulz et al., 1983]. Special purpose CT scanners are therefore designed combining a low keV photon source with good spatial resolution (<0.5mm) which results in very good reproducibility of bone density measurement with very low radiation dose. One such scanner was designed and fabricated at the University of Alberta in 1979 [Hangartner and Overton, 1982]. This scanner uses an ^{125}I point source and NaI(Tl)/PMT detector units. Changes in bone density can be determined with a precision of $\pm 0.9\%$ for an average local skin dose of 0.015 mSv per scan. The errors in bone density measurement due to marrow fat are small because the low photon energy provides a high contrast between bone and soft tissue. Sensitivity and precision are also improved at the lower photon energies.

2.1.8 Radiological Analysis of Bone and Bone Biology.

The radiological assessments of bone mineral content are based on the assumption that the amount of bone lost/gained does not change the composition of the bone cross-section in terms of the relative amounts of fat and soft tissue. A change in the composition of bone tissue results in an inaccurate measurement of mineral content. Similarly, the variable amounts of remodeling and mineralizing spaces can cause inaccuracy

in the results. In order to precisely and accurately measure the bone mineral content, and to understand the measured bone mineral content data, a knowledge of the composition, structure and the remodeling status of bone therefore becomes necessary.

2.2 Bone Biology

The human skeleton is an architectural structure which provides not only mechanical strength to the body but also acts as a mineral reserve. The skeletal functions are maintained through well defined metabolic activities in bone. The growth of human bones starts in the embryonic stage, and their size and shape are adjusted according to the eventual mechanical usage through bone formation and bone resorption processes. Bones continuously exchange minerals with the systemic circulation and maintain their compressive and tensile strength through a renewal process called 'remodeling'.

In this chapter the composition, structure and remodeling of bone are discussed, and their importance to an understanding of the radiologically measured bone mineral content data is outlined.

2.2.1 Composition and Structure of Bone

Human bone is made from a mineralized matrix of collagen fibers in an organic ground substance. Mechanical strength is provided by the collagen fibers and crystalline minerals. The minerals present in bone are calcium, phosphorous and carbonate in the form of calcium hydroxyapatite crystals. In the process of bone growth and maintenance, bone tissue is resorbed as well as formed. The bone cells which carry out the process of bone formation and bone resorption are known as osteoblasts and osteoclasts respectively. Osteoclasts are multinucleated cells which dissolve both the organic and inorganic bone substances through contact with their central ruffled border. Osteoblasts form bone in a two stage process of laying down collagen fibers in the ground substance and then by

facilitating the subsequent mineralization. In more detail, the osteoblasts deposit a layer of unmineralized (osteoid) matrix, known as the osteoid seam, which then begins to mineralize after a maturation period - a stage of primary mineralization. The completion of mineralization may take several months to a year. In addition to the osteoblasts and osteoclasts, there is another population of bone cells known as osteocytes which take part in mineral exchange and perform local bone turn over [Parfitt and Kleerekoper, 1979].

The structure of bone is characterized by a collection of "brick-like" pieces known as bone structural units (BSU) which are joined together by cement lines. The cement line is the boundary of a BSU which is fully mineralized. This basic structure characterizes the entire human skeleton but the bone can be classified by its two principal anatomical forms: cortical and trabecular bone.

Cortical (or compact) bone contains Haversian systems (osteons). Each Haversian system consists of a central canal which carries nutrient vessels, around which are concentrically arranged layers (lamellae) of mineralized bone extending up to the cement line. Each Haversian system is in close contact with all other Haversian systems through transverse Volkmann's canal and canaliculi. Cortical bone accounts for 80% of human bone volume but it provides only 30% of the bone surface area for mineral exchange.

Trabecular (or spongy) bone is an elegant architectural structure of plates and struts in close contact with spaces containing red and yellow marrow. A trabecular plate is also 'layered' or lamellar bone, e.g. as if an osteon was unrolled and spread flat. This bone accounts for approximately 20% of bone volume but provides 70% of the total bone surface area for mineral exchange.

The arrangement of cortical and trabecular bone gives rise to four different bone surfaces or envelopes: periosteum, Haversian, cortical endosteal and trabecular endosteal. On these surfaces all three states (formation, resorption and quiescence) can be found. The amount of formation and resorption varies from envelope to envelope with cortical endosteal and trabecular endosteal being more active than the Haversian and periosteal

envelopes.

2.2.2 Growth of Bone (Modeling)

Modeling is a process by which bone grows and changes its shape and size. The growth of bone and its final shape are achieved through resorption and formation drifts [Frost, 1982]. The resorption drift is due to a coordinated population of osteoclasts, the formation drifts a similar population of osteoblasts. These processes of resorption and formation are not coupled in modeling.

Longitudinal growth of long bones takes place through a process known as endochondral ossification [Frost, 1972] in which the primary spongiosa is formed. In this process the calcified cartilage is first resorbed within columns that are perpendicular to the growth plate and then woven bone is laid down. The cortical bone is formed from the cartilage by a process known as intramembraneous ossification [Frost, 1972]. In the transverse direction the thickness of cortical bone and the diameter of the marrow cavity increase by periosteal apposition and endosteal resorption.

In addition to nutritional, hormonal and genetic factors, the final shape and size of a bone is also governed by its mechanical usage. If normal mechanical usage produces flexural strain above a certain threshold level (minimum effective strain, MES), modeling activity will adjust the shape and size of bone such that the resulting strain is less than the new threshold level [Frost, 1982].

The quantity of bone accumulated during the growth period is very important since normally there is no bone growth after skeletal maturity.

2.2.3 Bone Remodeling

After skeletal maturity the mechanical competence and material properties of bone are maintained through a process known as remodeling. The fundamental entity of the remodeling process is the basic multicellular unit (BMU). Upon activation of a BMU

small quantity of bone is resorbed by osteoclasts and this resorption is followed by new bone formation by osteoblasts within the resorption cavity. Therefore, resorption and formation are strongly coupled in remodeling. The activation of the BMU and the resulting resorption and formation are spatially and temporally discrete events.

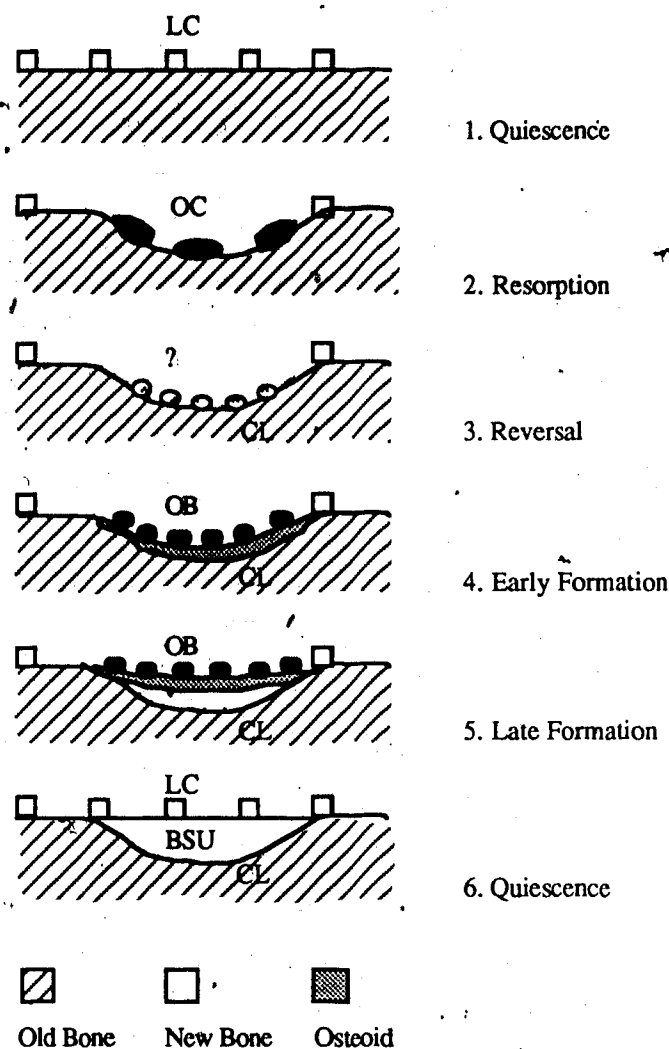


Figure 2.1: Bone remodeling

Figure 2.1 shows the history of a BMU undergoing remodeling to construct a new BSU in bone. The quiescent bone surface, covered by flat lining cells (LC), is resorbed by a group of osteoclasts (OC) to produce a cavity in the bone. The dimensions of a completed

BSU depend upon the quantity of bone removed by osteoclasts which in turn is determined by the number and the vigour of the BMU (osteoclast) population produced by the activation.

A cement line(CL) is deposited over the newly resorbed surface by a group of (as yet) unnamed mononuclear cells [Parfitt, 1981]. A group of osteoblasts(OB) then deposits a layer of unmineralized osteoid matrix over the cement line(CL). Primary mineralization of this matrix takes a few days, but then proceeds more slowly so that some 90-100 days are required for this part of bone to revert to histologic quiescence.

The time required for the resorption, reversal and formation processes is known as the remodeling period. The time required for complete mineralization of the BSU is known as the mineralization period. BMU-based remodeling has the following important properties [Frost, 1986]:

(1) BMU-based remodeling occurs throughout life in humans but it causes little change in the size and shape of bone.

(2) The difference between the amounts of bone resorbed and formed is known as bone balance per BMU and is denoted by $\Delta B.BMU$. This very important parameter determines the amount and sign of bone changes. The $\Delta B.BMU$ factor is generally zero on the Haversian envelope, slightly positive on the periosteum envelope and largely negative on the cortical endosteal envelope. The $\Delta B.BMU$ can control the bone balance independently of the bone resorption(formation) rates alone. This means that no matter how much bone is resorbed and formed in a typical BMU, the basic parameter which determines the bone balance is $\Delta B.BMU$.

(3) In a given bone the volume of a completed BSU varies very little. Therefore, bone turnover is determined mainly by the number of BMU's activated over a given time period in the unit volume of bone, i.e. activation frequency.

(4) In the steady state the global bone balance is determined by the activation frequency multiplied by $\Delta B.BMU$: therefore, bone balance can be controlled by these two

independent factors.

An example of such control is the treatment of osteoporosis by manipulation of coherent cell populations. The sequence of events in this process is activation- depression- free- repeat (ADFR). The BMU activation frequency is increased by giving an activation agent, e.g. Vitamin D [Hangartner and Overton, 1982]. Since resorption must occur before formation in the remodeling process, simultaneous activation of a large number of BMU will result in a large 'vacant' remodeling space in the bone. Therefore, bone mass will start decreasing soon after the activation event.

The normal activity of the osteoclast population is then reduced by giving a depressor agent (e.g. a bisphosphonate or calcitonin) such that a smaller than normal quantity of bone is removed by each BMU; this is known as a depression step in the ADFR process.

When the resorption period (about 10-20 days) is completed, the remodeling BMU is 'freed' to function independently. The osteoblasts will then (theoretically) deposit a normal amount of bone in each remodeling BMU cavity. However, since the volume of bone deposited by osteoblasts will be larger than the volume of bone resorbed by depressed osteoclasts, a net gain in the quantity of bone will result during this free period of the ADFR sequence. The whole activate-depress-free sequence can be repeated an appropriate number of times in order to obtain a desired gain in bone volume.

2.2.3.1 Classification of Bone Disorders

The various metabolic bone diseases can be differentiated on the basis of BMU-based remodeling. The skeletal state of reduced volume of otherwise healthy bone along with one or two vertebral fractures defines osteoporosis. In osteoporosis bone is lost either by a large negative ΔB BMU on the cortical endosteal surface, or by an increased bone turnover. In the first case (as in late stage involutional osteoporosis) the efficiency of the osteoblasts is decreased such that a smaller than normal amount of bone is formed per

BMU. In the second case (as in post menopausal osteoporosis) the small negative bone balance per BMU at the cortical endosteal and trabecular envelopes is amplified by an increased activation frequency [Parfitt, 1981]. If the resulting bone cannot withstand normal mechanical loading bone fractures occur and the person is then defined as 'osteoporotic'.

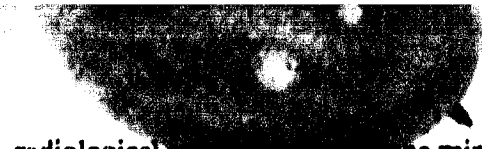
In case of osteomalacia, the BMU-based remodeling is arrested prior to the stage of mineralization. Therefore, the absolute bone volume may not change from normal levels but the mineral content is decreased and the osteoid seam thickness increased because of an increase in the mineralization lag time.

2.2.3.2 Effects of Bone Composition and BMU-based Remodeling on Radiological Bone Assessment

The techniques of radiological assessment of bone measure the amount of mineralized bone matrix within a specified bone volume. These measurements of bone mineral content are loosely given the name of bone "density".

The radiological techniques for measurement of bone mineral cannot differentiate spatially between trabecular plates and marrow spaces so that the resulting data includes contributions from both the mineral and non-mineral parts of trabecular bone. Therefore, the interpretation of bone mineral content data should take into consideration the changes in trabecular bone composition.

In the steady state a constant number of new BMUs is activated per unit time per unit surface area of bone. In each BMU a small amount of bone is first resorbed and then an osteoid seam is laid down which subsequently mineralizes. On the surface of the bone envelope undergoing remodeling there are vacant spaces, collectively known as the remodeling space (i.e. BMU at the reversal stage), which do not contribute to the photon attenuation. Similarly, the undermineralized bone known as the 'mineralizing space' will contribute less to the photon attenuation than the completely mineralized bone. The



radiological measurement of bone mineral content in a specified volume of trabecular bone is therefore underestimated due to the presence of remodeling and mineralizing spaces. Under steady state conditions for activation frequency, remodeling and mineralization periods, the errors from such sources are systematic and not important for serial studies. However, therapeutic intervention usually causes temporary changes in one or more of the above parameters which results in an error in the measured bone mineral content. For example, increasing the activation frequency will cause a temporary increase in the bone loss and the new steady state will only be reached after one complete remodeling cycle. In the new steady state for activation frequency, the remodeling and mineralization spaces will be larger than in the earlier state because a larger number of BMUs was activated per unit time. Therefore, the amount by which the bone mineral content will be underestimated will be increased proportionately. Remodeling and mineralizing spaces should therefore be taken into consideration if one or more of the bone remodeling parameters are changing over the period of a bone mass study.

Consideration of BMU-based remodeling is also important in the design of serial studies to assess the effects of therapeutic agents on bone since the resorption, reversal, formation and mineralization steps are separately defined.

We conclude that the mineral content of the trabecular bone can be measured using specially designed CT scanners, and that the interpretation of such data can be made on the basis of BMU-based bone remodeling. In the next chapter, we describe a particular special purpose CT scanner and its calibration, data collection and image reconstruction procedures.

3.0 Fan-beam X-ray CT Scanner for Quantitative Bone Density Measurement.

The γ -CT system designed and developed in the Department of Applied Sciences in Medicine is a second generation, translate-rotate scanner with a two minute minimum scan time. This relatively long scan time can result in subject movement, and hence artifacts in the image which increase both the analysis time and the inaccuracy in the bone mass measurement. The γ -CT scanner can only be used for bone density measurements at the distal radius site in humans since a low energy ^{125}I photon source (29 keV) is used and only objects of diameter less than 78mm can be scanned with good geometrical resolution. The isotope source is also very photon limited, increasing scan time in the reconstructed image.

These problems are partially resolved by using a rotate-rotate scanning geometry with a variable SCR distance to obtain a constant spatial resolution for a range of object sizes. In general rotational CT scanners require large numbers of closely packed photon detectors and hence are very expensive machines. The number of detectors required, however, can be decreased, with a corresponding increase in scan time, by using a multiple-rotation fan-offset scanning geometry [Peters and Lewitt, 1977; Jelinek and Overton, 1985].

The special purpose fan-beam X-ray CT scanner featuring a multiple-rotation fan-offset geometry and variable SCR distance was designed and developed by Hangartner [Hangartner and Overton, 1985]. In this chapter, the detector system and geometrical calibrations, data collection and image reconstruction procedures for this scanner are described. In order to better understand these procedures, a brief description of the hardware configuration, and of software implementation for this scanner precedes a discussion of the underlying theory and the experimental implementation of these procedures.

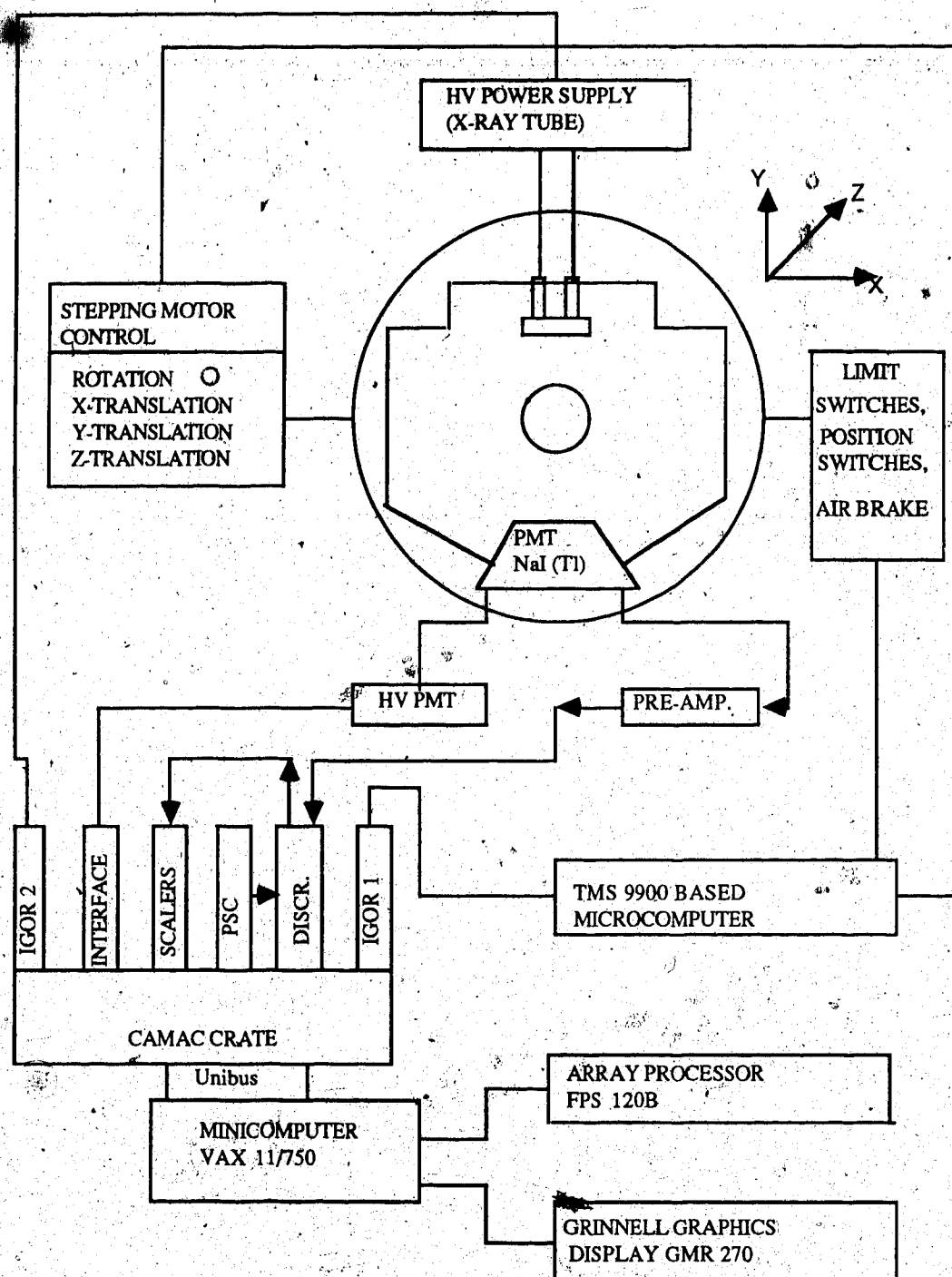


Figure 3.1.1: System schematic for X-CT scanner

3.1 System Description

The system schematic of this scanner is shown in Figure 3.1.1. The scanner can be divided into the following sub-systems:

- 1) X-ray tube and High Voltage Generation
- 2) Photon Detection System
- 3) VAX and CAMAC (Computer Automated Measurement and Control, IEEE Standard 583-1975) Interface System
- 4) Microcomputer and Scanner Control

Details of the design and development of the various sub-systems of this scanner are given in an earlier report [Wells, 1986]. In the following sections only a brief overview of these sub-systems is given.

3.1.1 X-ray Tube and High Voltage Generation

The photon source for the X-CT scanner is an X-ray tube with a 1mm^2 focal spot area and a 25° anode face angle. The photons emitted from the tube are collimated into a 50° fan angle using a 2mm wide lead collimator. The maximum operating voltage for the X-ray tube is 100kV; the maximum operating tube current is 10mA. The tube can be operated continuously at 140watts with a low pressure, circulating oil cooling system.

A compact DC high voltage generator which is based on the principle of switching DC power supplies is used [Fug Instruction Manual]. The maximum output ratings for the power supply are 120kV and 10mA. The high voltage is generated differentially such that a negative voltage is applied to the cathode and an equal positive voltage is applied to the anode. The filament current regulation is carried out by a programmable low voltage switching power supply. This high voltage power supply has a peak to peak ripple voltage of less than one part in 10^5 . The high voltage and the current for the X-ray tube can be regulated manually by potentiometers located on the front panel of the power supply, or these settings can be programmed remotely under VAX software control through the input

gate/output register (IGOR) module in the CAMAC crate. The maximum programmable voltage is limited to 96kV in order to protect the X-ray tube from overvoltage.

3.1.2 Photon Detection System

The photon detection system of the scanner comprises 26 NaI(Tl) detectors spaced at 2° intervals in the 50° fan-beam. The detector collimator has an aperture width of 3mm in the axial direction and 1mm in the radial direction and is 6mm long which reduces the effects of scattered radiation.

The electronics of the detectors are designed to work in count mode; each photon interacting with the detector crystal produces an individual current pulse at the output of the photomultiplier tube (PMT) which is amplified by a current-to-voltage converter/pre-amplifier, based on the LeCroy TRA1000 pre-amplifier circuit and designed to give a closed loop gain of 20mV/μA [LeCroy Systems, 1978]. The differential voltage pulses from the output of the pre-amplifier are fed to the differential input of a pulse height discriminator. The assembly containing the PMT/NaI(Tl) detectors and pre-amplifier circuitry is electrically isolated from the rest of the scanner in order to avoid noise in the data resulting from ground loops.

The discriminator outputs a logic pulse to a scaler provided the amplitude of the voltage pulse at the input of the discriminator exceeds a certain threshold level (see section 3.2.1). The threshold level of the discriminator can be varied manually or remotely by changing the voltage applied to the external threshold connector. In the remote mode the voltage applied to the connector is programmed by a programmable supply controller (PSC) module.

The scalers count the number of pulses until the 'load' line of the all the scalers is pulsed to indicate the end of a data collection interval. At this time the CAMAC controller interrupts the VAX, and the collected counts for the programmed number of detectors are stored in a temporary buffer. At the end of the data collection process, the counts for all

data collection intervals are accumulated in a VAX data file.

The counting mode for photon detection is better than the current integrating type of data acquisition systems used in commercial CT scanner systems. The current integrating type systems use analog integration of the signal from PMT followed by sample/hold and analog to digital conversion. The input offset voltage of these components and quantization error in analog to digital conversion increase the minimum level of signal detected, which is not very useful for detecting a low photon flux. The detection efficiency of the counting system is improved because each individual photon interacting with a detector is recorded separately. However, the fluorescence decay time constant of the NaI(Tl) scintillator (250nsec), and to a lesser extent the propagation delays in the electronic circuitry, introduce a 'deadtime' in the counting system during which the system is unable to record photons incident upon the detector. The theory of the deadtime calibration procedure for the X-CT system is described in section 3.2.2. The deadtime of the system depends upon the incident photon fluence, and for a relatively low count rate the error in the number of photons observed is very small.

3.1.3 VAX and CAMAC Interface System

The master controller for the X-CT scanner is a VAX 11/750 minicomputer, a multiuser system with 6 megabytes of main memory and 450 bytes of disc storage in addition to 1600 bpi magnetic tape. The minicomputer is connected to an array processor (FPS-120B) for the mathematical operations of convolution and backprojection, required for image reconstruction.

The basic purpose of CAMAC is to provide a standardized method for transmitting data between VAX and the various instrumentation modules of the scanner. The CAMAC modules are interfaced to the Unibus of the VAX system by the controller. The various modules of the CAMAC system used in the X-CT scanner are described below.

- (1) A CAMAC crate controller module (Kinetic Systems 3912) which

communicates directly with both the VAX and the other CAMAC modules.

(2) Two IGOR modules (**Kinetic Systems 3063**) each featuring an output register, an input register and handshaking signals for data communication. One of the IGOR modules is used for data communication between the VAX and the microcomputer used for control of the scanner movements; the other module is used for programming the X-ray tube voltage and current under VAX software control.

(3) An interface module (**LeCroy 2132**) allows bi-directional communication between the CAMAC dataway and up to 15 high voltage supplies used for the PMTs. The high voltage system (**LeCroy HV4032A**) provides up to 32 independently programmable channels. The PMT high voltages can be set manually or remotely via this interface module.

(4) A dual PSC module (**Kinetic Systems 3162**) featuring two 12-bit digital-to-analog converters is used for programming the discriminator threshold voltage for the discriminators used in this system.

(5) Two discriminator modules (**LeCroy 4415**), each consisting of 16 channels of differential input discriminators. The common discriminator threshold level for all 16 channels can be varied from -30mV to -600mV and can be set manually or remotely through an external voltage applied to the threshold control connector.

(6) A scaler module (**LeCroy 4434**) with 32 channels of 24 bit scalers. Each scaler counts pulses of duration greater than 10nsec and a maximum frequency of 20MHz.

Other peripheral devices associated with this system are a GRINNELL (GMR 270) image display system and a Versatec (V80) hardcopy plotter.

3.1.4 Microcomputer and Scanner Control

The X-CT scanner uses a multiple-rotation fan-offset scanning geometry in order to increase the radial sampling density, and hence the spatial resolution in the reconstructed images. Objects with diameters ranging from 75mm to 220mm can be scanned by varying

the SCR distance, and hence maximizing the number of detector rays passing through the object [Zatz, 1981]. The scanner is designed to translate in the x-, y- and z-directions and to rotate in the x-y plane over 360° (Figure 3.1.1). The horizontal movements (x-direction) are used for centering the fan-beam about the center-of-rotation of the scanner (section 3.2.5), and to provide the linear shifts of the fan-beam from the SCR line in the data collection procedure of the scanner (see section 3.3.1). The vertical movement (y-direction) of the scanner is used for optimizing the SCR distance with respect to object size in order to obtain the same geometrical resolution for different object sizes. The axial movement (z-direction) is used for positioning the fan-beam of the scanner at the measurement site determined by a digital radiograph (see section 5.1). The rotational movement of the scanner is used for data collection. A combination of x-, y- translation and rotation is used to simulate a small rotation of the detectors about the source (see section 3.3.1).

All four movements of the scanner are carried out using stepping motors. The speed and direction of each stepping motor is controlled by the frequency and the sequence of the pulses given to its four windings. The movement of the stepping motors is controlled by the microcomputer and the scanner control system. In addition, the microcomputer processes the status of limit switches and the air brakes used for mechanical safety, and the position switches used for determining the reset (home) position of the scanner. The microcomputer also controls the timing of the interrupt pulses given to scaler units at the end of each data collection interval.

The microcomputer consists of a TMS 9900 microprocessor based CPU (central processing unit) board, an I/O (input/output) board for communication with CAMAC, and a third board for generating timing pulses to stepping motors. A customized data communication protocol is used for sending commands for motor movements from the VAX to the microcomputer through an IGOR module of CAMAC [Wells, 1986]. Information concerning the speed, direction and length of the motor movements is downloaded from the VAX and status information from the scanner is uploaded to the

VAX through the same IGOR module.

The control system contains the translation control boards for each of the motors and a relay control board for processing the limit switch and air brake signals. The motors can also be operated manually in which the speed and direction of each of the motors can be set by switches located in front of the corresponding translator control board.

3.1.4.1 Scanner Reset Position

The scanner has to be in the reset position before any data collection for calibration or image reconstruction purposes is initiated. The reset position of all four scanner motors is determined with reference to the position switches corresponding to each of the scanner movements. The position switch is an oscillator which changes its internal impedance when a metal 'flag' comes closer to its surface.

The reset position of the axial motor is specified by the position of a horizontal cross-hatch of laser beam mounted in the ceiling above the scanner. The distance between this cross-hatch and the axial position switch is determined by placing a metal wire aligned with the cross-hatch. The wire is placed aligning with the horizontal cross of the laser beam such that it intersects with all 26 detector rays. Data for all 26 detectors are collected as the axial motor moves the fan-beam in the forward direction starting from the axial position switch until the fan-beam passes over this wire. A drop in photon intensity due to the wire gives the position of the horizontal cross-hatch and thus the reset position of the axial motor.

For the rotational reset position the motor is moved counter clockwise until the rotational position switch is detected, and then moved 180° clockwise from the position switch to the reset position.

The reset position of the horizontal motor is established during the fan-beam centering procedure discussed in section 3.2.5. The reset position of the vertical motor depends upon the object size. The scanner is setup for object diameters of 75mm, 100mm

and 150mm, but the vertical motor reset position from the vertical position switch is programmable from software.

3.1.4.2 Motor Movements in Data Collection

Data collection for this scanner can be initiated by moving any of the four motors. Each motor has an assigned location in the microcomputer memory where the motor movement description table is stored after downloading from the VAX. Each line in this table contains the number of steps of motor movement, the speed of the motor and the number of steps in a data collection interval, so that the data collection interval can be controlled in the VAX software. A few lines at the beginning of the motor description table are used for accelerating the motor to desired speed, and a few lines at the end for decelerating the motor speed to zero. A motor can be moved without collecting data by setting the number of steps in a data collection interval within the motor description table to zero.

In addition to downloading the motor description table for data collection the CAMAC driver control is also informed of the size (16 or 32bit) and length (number of data collection intervals) of the data. The data can be collected for all or for only selected channels by informing the CAMAC driver software accordingly. The number of data collection intervals programmed in the motor movement description table should match the number given to the CAMAC driver software, except for the first interval for which the duration is unknown.

3.2 System Calibration

In an ideal photon detector system all the detectors would have the same energy resolution, matched observed spectra, zero background noise count and zero dead-time. Similarly, a perfect X-ray source would be mono-energetic with a vanishingly small point focal spot, and isotropic angular flux distribution. Obviously these features are not realized

in any practical CT system, so procedures to correct for these imperfections are required before the CT system can provide artifact-free images.

A detailed analysis of the theory and implementation of the calibration procedures for the X-CT scanner has been reported by Wells [Wells, 1986]. For our work, the scanner has to be calibrated at two energies for dual energy scanning, and the calibration procedure at X-ray tube potentials of 50kV and 80kV is discussed in the following sections.

3.2.1 X-ray Spectrum Matching

The noise generated by a PMT depends on its gain and its peak anode current in that a larger number of light photons falling on the photo-cathode increases the noise generated [Hamamatsu]. Thus the charge collected at the last dynode of the tube also includes contributions due to noise; the counting system has to discriminate between noise and the signal due to photons which requires the setting of a discriminator 'threshold' to exclude noise.

The need to match the measured spectrum for each detector arises because a common discriminator threshold level is used for all the detectors. Although the photon energy spectrum incident on all the detectors is the same, the observed spectra will be different for each detector because:

- a) the energy response of the NaI(Tl) crystal varies slightly from detector to detector.

- b) there is a finite dead-time associated with the detector system, so the shape of the observed spectrum will depend upon photon fluence incident on the detector.

As the quantity of charge collected by the last dynode of a PMT is a function of inter-dynode potential and the amplitude of the output pulse increases as this potential is increased, so the measured spectrum of a detector can be shifted along the energy scale by changing the high voltage applied to its PMT.

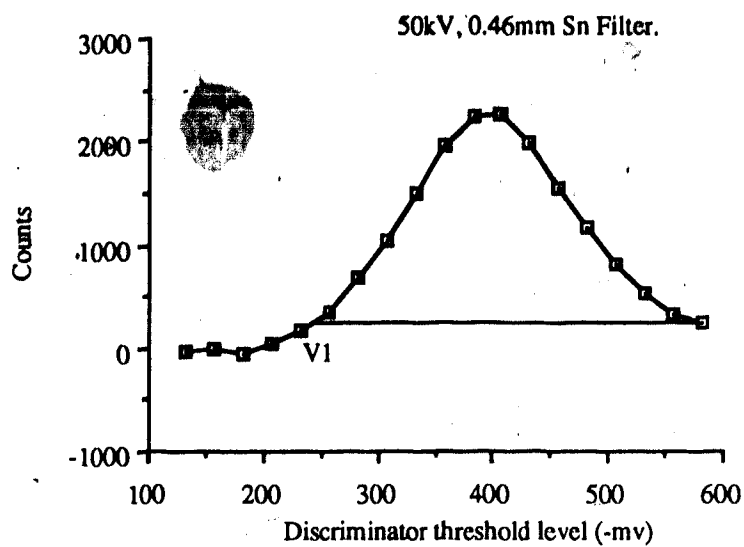
The instrumentation of the X-CT scanner does not readily permit direct pulse height analysis, so an indirect method of calculating the pulse height spectrum is used. A 0.46mm thick (Sn, $K_{\text{esc}}=29.2\text{keV}$) filter is used to limit the spectrum to energies between 20keV to 30keV at the lower tube potential (50kV), and between energies of approximately 40keV to 65keV at the higher tube potential (80kV).

The procedure works as follows. The detectors are given an initial PMT high voltage and the total number of photons collected by each detector in one second is measured as the discriminator threshold level is varied in steps of 25mV from -120mV to -600mV. A differential spectrum is calculated by subtracting successive readings for each detector. The lower and higher energy measured spectra of a detector are shown in figure 3.2.1.

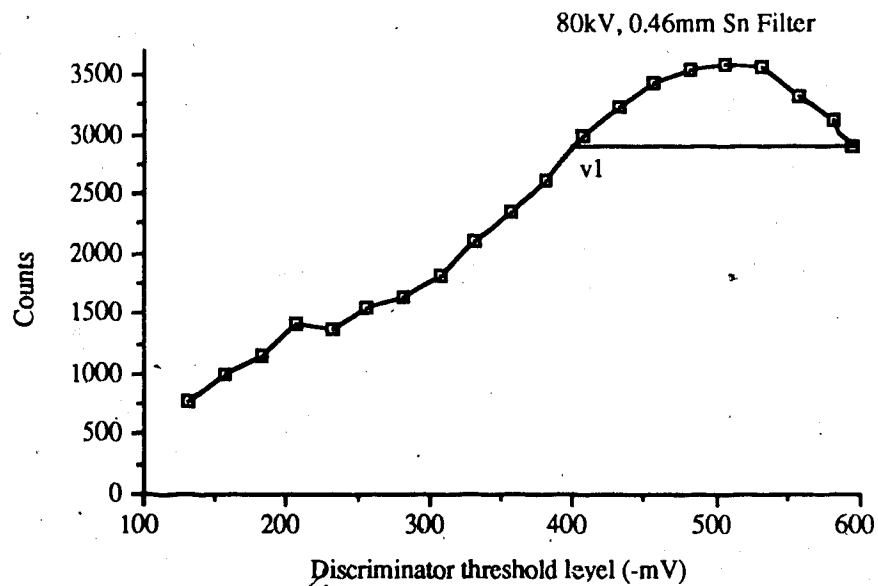
Let $I(v_t)$ be the number of photons in the observed differential spectrum and v_t the discriminator threshold level. $I(v_t)$ and v_t are the y-axis and x-axis parameters in figure 3.2.1. A baseline $y = I(-600\text{mV})$ is drawn which intersects the spectrum at -600mV and v_1 as shown in the figure. The peak position of the spectrum is then given by

$$V_{\text{peak}} = \frac{\int_{v_1}^{600} I(v_t) v_t dv_t}{\int_{v_1}^{600} I(v_t) dv_t} \quad (3.2.1)$$

The peak positions of the spectra at 50kV are compared with a reference position of $-400 \pm 10\text{mV}$ and those at 80kV with $-475 \pm 10\text{mV}$. The PMT high voltage of those detectors which show a deviation of more than $\pm 10\text{mV}$ from the reference position is then changed. This procedure is repeated until the spectra for all detectors are matched. Due to the short time (5-10 minutes) needed to perform this calibration, it would be possible to carry it out every day.



(a)



(b)

Figure 3.2.1: Differential counts vs the discriminator threshold level for (a) 50kV and (b) 80kV using a 0.46mm Sn filter.

A common threshold is used for all 26 detectors and this is determined from the shape of the observed spectra. The common discriminator threshold is selected at a point in the spectrum where the slope is a minimum and only the noise is completely discriminated.

An appropriate, common discriminator threshold was found to be ~~200~~ mV for both 50kV and 80kV.

3.2.2 Dead-time Corrections

All practical radiation detectors have a finite resolving time, or interval that must separate two events if they are to be separately registered. This interval is referred to as the 'dead-time' of the system, during which no additional photons can be detected. For a NaI(Tl)/PMT detector the dead-time is due principally to fluorescence decay of the crystal, and to a lesser extent to the resolving capabilities of the pre-amplifier/amplifier and discriminator/scaler circuits. The effect of the dead-time is seen in the non-linear relationship between observed counts (N_o) and incident photon fluence.

Two models are commonly used to describe the dead-time behaviour of counting systems: *paralysable* and *non-paralysable* response. For a non-paralysable model [Knoll, 1979]:

$$N_t = \frac{N_o}{1 - N_o \tau_d} \quad (3.2.2)$$

where N_t is the true counts, N_o the observed counts and τ_d the dead-time of the counting system. Similarly for a paralysable model [Knoll, 1979]:

$$N_t = N_o e^{N_o \tau_d} \quad (3.2.3)$$

It has previously been shown that the counting system of this particular scanner does not closely follow either of these models [Wells, 1986] as is evident from the experimental data shown in figure 3.2.2.

By using a paralysable model, and assuming that N_t is proportional to the X-ray tube current, a calibration procedure was developed to determine the dead-time for each of

the 26 detectors. Since there is no analytical solution for calculating true counts for the paralyzable model the raw data in the reconstruction procedure was corrected assuming a non-paralyzable model and using the dead-times so calculated.

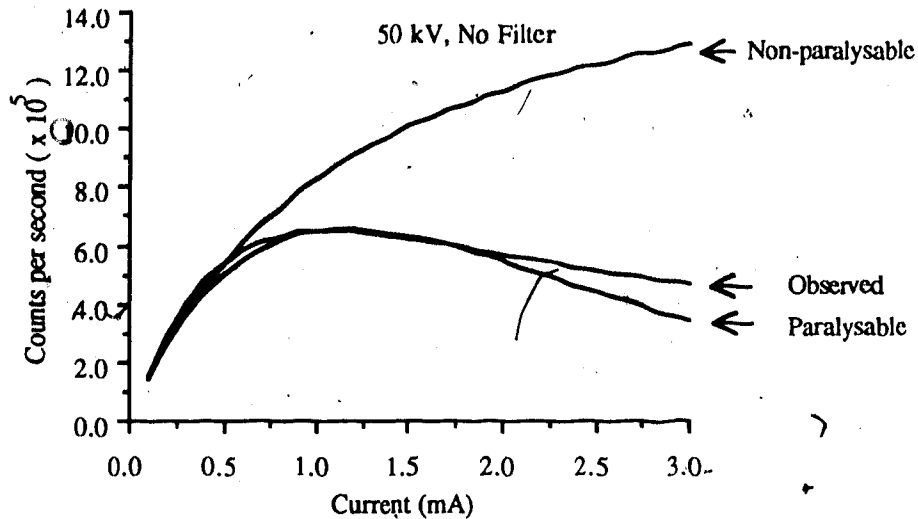


Figure 3.2.2: The observed number of photons as a function of X-ray tube current (or true counts) for a detector. The corresponding counts for *paralysable* and *non-paralysable* responses for $T_d = 500$ nSEC are also shown.

A reconstructed image of a phantom is shown in figure 3.2.3 where circular ring artifacts due to this imperfect dead-time correction are seen. The radii of these circular ring artifacts are equal to the perpendicular distances from the center-of-rotation to the source-to-detector lines of those detectors for which the dead-time estimation was wrong by a significant amount [Jelinek and Overton, 1986].

A simple but more precise method of correcting for dead-time was developed based on the fact that the increase in the N_o vs. N_t curve up to its maximum can be described by a second order polynomial [Kohman, 1945]:

$$N_o = a N_x + b N_x^2 \quad (3.2.4)$$

nd

$$N_t = m N_x \quad (3.2.5)$$

where N_x represents the X-ray tube current. This procedure measures the counts per second as the X-ray tube current is increased from 0.1 to 3.0mA for both 50kV and 80kV tube voltages, using 0.65mm and 2.75mm Cu filters respectively. The coefficients a and b for each detector at both X-ray tube settings are calculated by using a least squares fit of a second order polynomial to the data. The value of m was calculated by using the equation (3.2.5) assuming that the observed count rate is approximately equal to the true count rate at a tube current of 0.1mA. This calibration procedure was performed for both 50kV and 80kV X-ray tube potentials.

Since the coefficients a and b were calculated from the data which was collected using a 1second time-base the raw data used in the reconstruction needs to be adjusted to the same time-base before correction. The values of the coefficients a , b and m can then be used to correct the observed counts. An image of a phantom reconstructed by this method is shown in figure 3.2.4 where artifacts due to the imperfect dead-time corrections have vanished.

3.2.3 Background Noise

Background noise has two components, a 'dark count' due to electronic noise and a background radiation count. The electronic noise is caused by the following factors [Hamamtsu]: (1) thermionic emission of electrons from the photocathode or dynodes of the PMT and (2) ionization of residual gases inside PMT by electrons. Since a discriminator threshold level of -200mV is set at both the X-ray tube settings (0.65mm Cu filter at 50kV, 2.8mA and 2.75mm Cu filter at 80kV, 1.75mA), the majority of low energy noise pulses are removed. However, the higher energy noise passes through the discriminator and adds to the signal. Any noise greater than -200 mV is due mainly to the background radiation

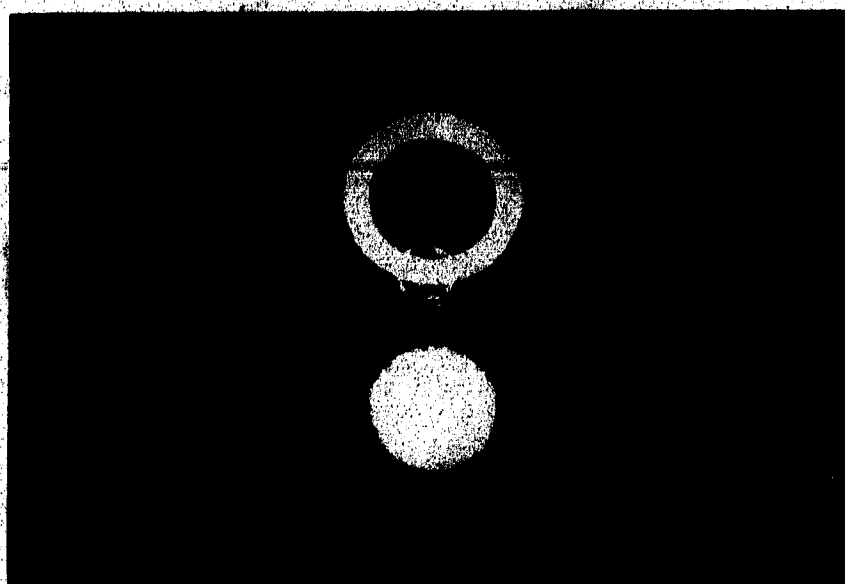


Figure 3.2.3

CT image of a plexiglass phantom: The upper dense annulus is aluminum and the lower, lesser dense solid circle is Teflon. Circular artifacts due to imperfect deadtime correction are evident.

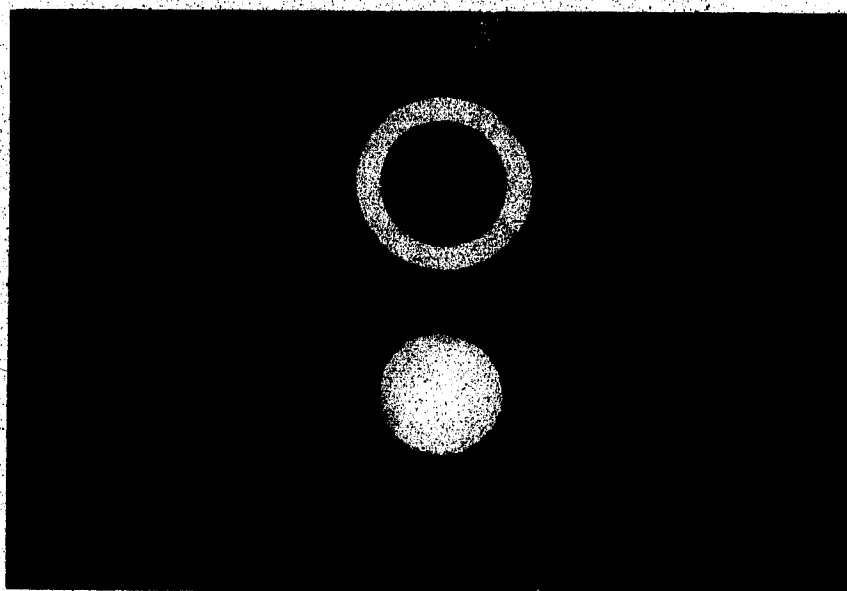


Figure 3.2.4

CT image of the same phantom: Proposed deadtime correction removes the circular ring artifacts.

(Wells, 1986), and is therefore independent of PMT current.

The amplitude of the current pulse at the anode of the PMT, due to background radiation, depends on the inter-dynode potential. The applied PMT high voltage for each detector is smaller at 80kV, 1.75mA than at 50kV, 2.8mA. This was necessary since at the same PMT high voltage the detectors start saturating at 80kV, 1.0mA even with the greater degree of filtration. Therefore, the background noise counts due to background radiation are different for the two X-ray tube settings.

The background noise counts of amplitude larger than the discriminator threshold are measured over a period of one hour with the X-ray tube off. The PMT high voltages are set appropriately for both X-ray tube potentials. In the reconstruction process, the background noise counts per interval are subtracted from the raw data before the dead-time and beam-hardening corrections are carried out in the reconstruction. At the discriminator threshold level used (-200mV), the average background count is of the order of 0.0005 % [Wells, 1986], therefore, the dark count correction has no significant effect on the reconstructed images.

3.2.4 Beam Hardening Calibrations

In CT, measurements of the linear attenuation coefficients at each point in a cross-section of an uniform object are different due to the polyenergetic nature of the X-ray beam. Since the attenuation at a fixed point is greater for lower energy photons, the energy distribution of the X-ray beam shifts towards higher energies (hardens) as it passes through the object. X-rays reaching any particular point inside an object from different directions are likely to have different energy fluence and thus will be attenuated differently at that point. This effect results in both quantitative and qualitative artifacts in the reconstructed images. It has been shown [Brooks and Di Chiro, 1976] that CT numbers at the center of the image of a phantom containing homogeneous material will be decreased due to beam

hardening, showing the well known 'cupping' effect in the attenuation profile of the reconstructed image. The beam hardening effect is, in general, non-linear [Joseph, 1981] and causes streaks in the image of a high contrast object.

The accuracy of bone mass measurements is also affected by beam hardening because of the variable amount of soft tissue surrounding the cortical bone [Hangartner et al., 1987; Vetter et al., 1986]. Several techniques are available to reduce the errors due to beam hardening, such as water-bag filters [MaDavid et al., 1977], polynomial fitting and linearization [Herman, 1979], and material selective corrections [Rüegsegger et al., 1978].

In single energy measurements of bone mass with the X-CT scanner, a simple, approximate method of correcting beam hardening errors has been developed [Wells, 1986]. A projection ray-sum or a logarithmic attenuation is defined as the natural log of the ratio of the incident number of photons (I_0) to the transmitted number of photons (I). The underlying assumption with this procedure is that any measured projection ray-sum is the result of attenuation of the beam by a sandwich of specified thicknesses of aluminum and plexi-glass. The correction procedure involves scanning successive layers of 5.85mm thick plexi-glass and 0.85mm thick aluminum sandwiches, and measuring the projection values corresponding to each layer. If the X-ray source was mono-energetic then the projection values corresponding to successive layers would increase linearly, but a polyenergetic beam hardens as the number of layers is increased resulting in a smaller attenuation by the added layers. This effect is shown in figure 3.2.5 where projection values are plotted as a function of thickness (numbers) of aluminum and plexi-glass plates. The deviation from linearity is determined by fitting a second-order polynomial to this curve; the coefficients of this polynomial are used to correct the projection values before convolution and back-projection for image reconstruction. This procedure is performed at both the X-ray tube settings.

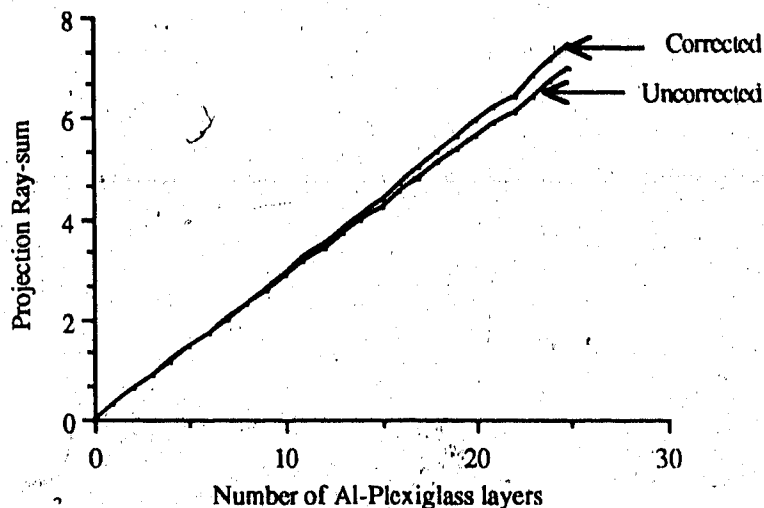


Figure 3.2.5: The logarithmic attenuation of a 50kV beam as a function of the number of layers of 5.85mm thick plexiglass and 0.85mm thick aluminum sandwich. The corrected data is obtained after linearizing the observed data by fitting a second order polynomial.

After linearization of the data, a linear correlation coefficient better than 0.98 was obtained for all detectors ($p < 0.001$), however, small errors due to variable amounts of soft tissue surrounding the cortical bone will occur, as discussed in section 6.1.2.

3.2.5 Centering The Fan-beam.

In a multiple rotation fan-beam scanner it is necessary that the initial fan offset, and the linear offsets between the rotations, are precisely determined (see section 3.3.1 for details). This requires that in the "home" position the SCR line bisects the detector arc so that the source to detector rays on both sides of the SCR line are symmetrical. The fan-beam centering procedure determines the reset (home) position of the horizontal motor.

The geometric considerations of this procedure are depicted in figure 3.2.6. For simplicity only two detector rays are shown in this figure. The centered fan-beam at 0° and 180° , shown by thin lines, is symmetrical about the SCR line (A-O-B). The thick lines depict the same fan-beam at 0° and 180° when it is not symmetrical about the SCR line, where AA' and BB' give the linear shift ΔX of the fan beam from the SCR line at 0° and 180° respectively.

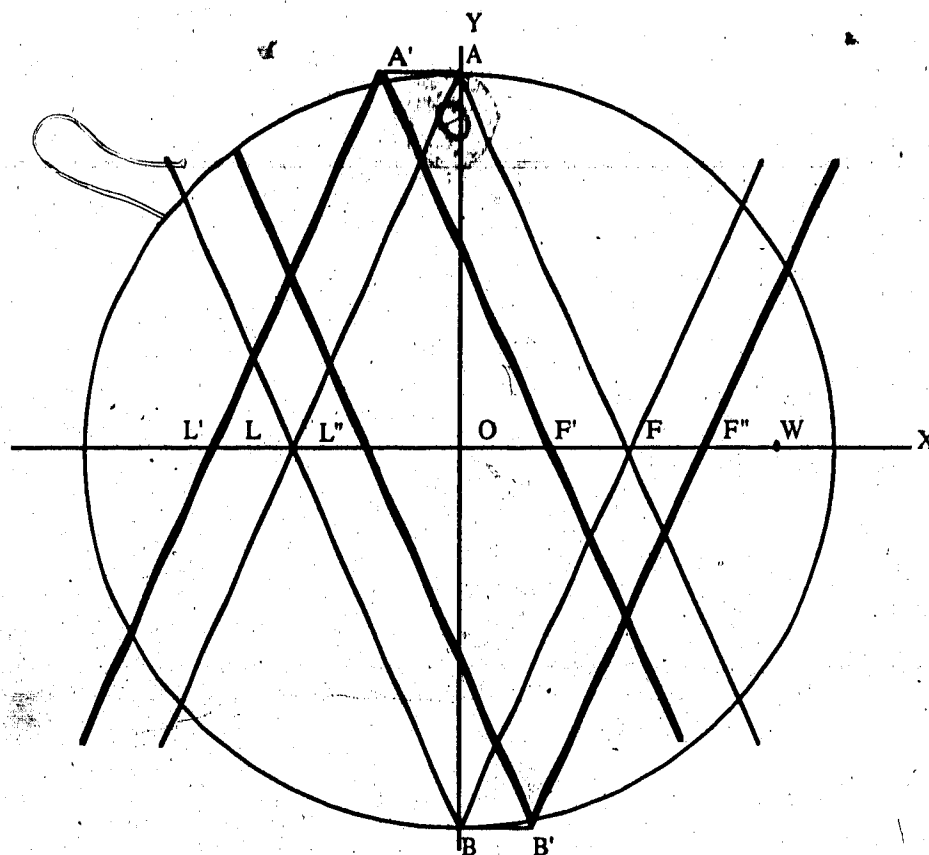


Figure 3.2.6: The centered and linearly shifted fan-beam at 0° and 180° .

A wire is placed in the fan beam, shown by point W in the figure, and the scanner is translated horizontally so that the beam for each detector passes through the wire. The point at which the wire passes through each beam is recorded as a drop in count rate for that particular detector. For each detector the distance through which the fan beam moves before the ray corresponding to a particular detector passes through the wire, is calculated. For the symmetrical fan beam, these distances are given by WL and WF for the two detectors in 0° and 180° positions. Similarly, WL' and WF' give the corresponding distances for two detectors, in case of asymmetrical fan-beam at 0° . The scanner is then rotated by 180° and the procedure is repeated and distances WL'' and WF'' for the asymmetrical fan-beam are measured. Due to the limited horizontal movement of the X-CT scanner (1.9cm), only six detectors pass by the wire which is horizontally aligned at the

center-of-rotation. Consider the following from Figure 3.2.6:

$$\begin{aligned}
 (WL' + WF') - (WL'' + WF'') &= (WL' - WL'') + (WF' - WF'') \\
 &= AA' + BB' + AA' + BB' \\
 &= 4 \Delta X
 \end{aligned} \tag{3.2.6}$$

So the linear shift ΔX can be found by determining the distances WL' , WL'' , WF' and WF'' . Although only two detectors are shown in the figure, the above procedure can be generalized. Let there be N detectors which show a drop in count rate due to the wire when the fan is translated horizontally. If $X_{n,1}$ and $X_{n,2}$ are the distances through which the fan moves before the n th detector ray encounters the wire at 0° and 180° respectively, then the linear shift of the fan beam is given by:

$$\Delta X = \frac{\sum_{n=1}^N X_{n,1} - \sum_{n=1}^N X_{n,2}}{2N} \tag{3.2.7}$$

The linear shift determined by this procedure is used to correct the reset position in the reset scan procedure such that the central ray of the fan beam will always pass through the center of rotation. The centered position of the fan beam is independent of the SCR distance so it is only determined for a particular SCR distance.

3.2.6 Geometrical Calibrations.

Both the data collection and image reconstruction require precise measurement of two more geometrical parameters, the SCR distance and the detector angles about the SCR line.

The geometrical considerations of this calibration are given in figure 3.2.7, where S and CR are the focal spot of the X-ray tube and the center-of-rotation of the scanner, respectively.

joining the wire and center-of-rotation (W-CR) coincides with the new X-axis, then the co-ordinates of points A_i and B_i in the X' - Y' co-ordinate system are given by:

$$X'A_i = p \cos A(i) \quad (3.2.8)$$

$$Y'A_i = p \sin A(i) \quad (3.2.9)$$

$$X'B_i = p \cos B(i) \quad (3.2.10)$$

$$Y'B_i = p \sin B(i) \quad (3.2.11)$$

where p is the radius of the circle centered at CR which passes through the wire W .

Let $(m'(i), i=1, 26)$ be the slopes of the detector rays with respect to the X' - Y' co-ordinate system, then $m'(i)$ is given by:

$$\begin{aligned} m'(i) &= \frac{p \sin B(i) - p \sin A(i)}{p \cos B(i) - p \cos A(i)} \\ &= \frac{\sin B(i) - \sin A(i)}{\cos B(i) - \cos A(i)} \end{aligned} \quad (3.2.12)$$

The next step in this procedure is to determine the co-ordinates of the focal spot S , and CR.

The co-ordinates of the focal spot are determined by the points of intersection of the i th and j th beams as given by following equations:

$$X_{s(i,j)} = \frac{Y'A_j - Y'A_i + m'(i)X'A_i - m'(j)X'A_j}{m'(i) - m'(j)} \quad (3.2.13)$$

$$Y_{s(i,j)} = \frac{m'(i)m'(j)(X'A_i - X'A_j) + m'(i)Y'A_j - m'(j)Y'A_i}{m'(i) - m'(j)} \quad (3.2.14)$$

The values of the X'_s and Y'_s are determined for the intersection of all possible combinations of the i th and j th beams.

A perpendicular drawn from CR to a detector ray i bisects this ray and the co-ordinates of the point of bisection can be determined from the co-ordinates of points A_i and B_i . Therefore, the center-of-rotation is the point of intersection of perpendiculars drawn at the points of bisection of all detector rays, enclosed by the circle of radius p . The slopes of these perpendiculars are determined from the slopes of detector rays in the $X'-Y'$ co-ordinate system, hence equations (3.2.13) and (3.2.14) give the co-ordinates of CR after replacing $(X'A_i, Y'A_i)$ and $(X'B_i, Y'B_i)$ with the co-ordinates of points of bisection, and $m'(i)$ and $m'(j)$ with the slopes of perpendiculars drawn at the points of bisection of rays i and j respectively. The values of $X'CR(i,j)$ and $Y'CR(i,j)$ for all combinations of i and j are therefore determined. The co-ordinates $X'CR(i,j)$, $Y'CR(i,j)$, $X's(i,j)$ and $Y's(i,j)$ are used to calculate the average slope $m(0)$ of the SCR line in $X'-Y'$ co-ordinate system along with the length of SCR line. The angle of rotation $\Theta(0)$ of the $X'-Y'$ co-ordinate system from the $X-Y$ co-ordinate system is calculated from the slope $m(0)$. The slopes $m(i)$ of the detector rays with respect to $X-Y$ co-ordinate system can then be determined by the following equation

$$m(i) = \text{TAN} \left(\text{TAN}^{-1}(m'(i)) - \Theta(0) \right) \quad (3.2.15)$$

and the angles of the detectors about the SCR line are given by:

$$\Theta(i) = \text{TAN}^{-1} \left(\frac{1.0}{m(i)} \right) \quad (3.2.16)$$

Similarly the SCR distance is given by the co-ordinates of the focal spot and the center-of-rotation:

$$\begin{aligned}
 SCR_1 &= \frac{1}{N} \sum_{i,j} \sqrt{(X'_{S(i,j)} - X'_{CR(i,j)})^2 + (Y'_{S(i,j)} - Y'_{CR(i,j)})^2} \\
 &\propto p \\
 &= K_1 p
 \end{aligned} \tag{3.2.17}$$

where K_1 is a constant dependent upon the SCR distance and N is the number of combinations of i and j .

Since the value of p is not known the whole experiment is repeated at a different SCR distance keeping the position of the wire (and hence value of p) the same outside the fan-beam. This measurement gives a SCR distance different from the previous value such that:

$$SCR_2 = K_2 p \tag{3.2.18}$$

We also know the difference d between the two source positions such that:

$$\begin{aligned}
 d &= SCR_1 - SCR_2 \\
 &= (K_1 - K_2)p
 \end{aligned} \tag{3.2.19}$$

The value of the SCR distance at the two source positions can then be calculated from the following equations:

$$SCR_1 = \frac{K_1 d}{(K_1 - K_2)} \tag{3.2.20}$$

$$SCR_2 = \frac{K_2 d}{(K_1 - K_2)} \tag{3.2.21}$$

In the preceding discussion it was assumed that by placing a wire outside the fan-beam and rotating the scanner by 360° , we can accurately find the angles $A(i)$ and $B(i)$ for

all the detectors. In order to know these angles accurately a large number of angular samples around the circle are required for all detectors. Since each data point is 4 bytes and the CAMAC I/O buffer is limited to 64 Kbytes, data for only three detectors is collected during one rotation containing 4570 angular samples for each detector (i.e. $4 \times \text{number of angular samples} \times \text{number of detectors} < 64 \text{ Kbytes}$). A total of nine rotations is therefore required to collect data for 26 detectors at each source position. This experiment was performed 15 times at each source position and average values for SCR distance and detector angles were calculated. The mean value of the SCR distance at 75mm object size setting was found to be 98.7mm with a standard deviation of 0.1mm. The standard deviation of measurement of all detector angles was less than 0.02° and mean inter-detector angle was approximately 2° .

3.3 Data Collection and Image Reconstruction

The methods for data collection and image reconstruction are unique to this CT scanner. In the following discussion the fan-beam geometry is analysed to ensure efficient data collection and image reconstruction. It will be shown that the spatial resolution of a fan-beam scanner can be improved by rotating the scanner more than once with different radial positions of the detectors in each rotation.

3.3.1 Data Collection

The effective detector aperture width (a_{eff}) is given by [Yester and Barnes, 1977]:

$$a_{\text{eff}} = \frac{1}{M} \sqrt{a^2 + (M-1)^2 s^2} \quad (3.3.1)$$

where a and s are the dimensions of the detector aperture and focal-spot respectively, and M is the magnification determined by the ratio of the focal-spot to detector and the

focal-spot to center-of-rotation distances. If both the intensity of the focal spot and the response of the detectors are constant over the appropriate dimensions and zero outside, then the effective beam profile is also constant over the width a_{eff} and zero outside it. Since a measured projection in a CT scanner is the convolution of a beam profile and an actual projection, the spatial resolution is limited by the finite value of a_{eff} . The value of a_{eff} also determines the sampling requirements in that there should be at least two samples per effective aperture width to satisfy the Nyquist criterion and avoid 'aliasing' artifacts in the reconstructed image [Stockham, 1979]. In a fan-beam, rotate-rotate CT scanner radiographic sampling is limited by fan geometry and detector size. A single 360° rotation would give one sample per effective aperture width and the sample positions would be determined by the position of the detectors in the fan. An arrangement of a large number of small and closely packed detectors in the fan improves the sampling density, however, for such an arrangement the cost is high. Even if the focal spot dimensions are small compared to the detector aperture, two samples per effective aperture width are still not available. This difficulty can be overcome by using a relatively small number of detectors and a detector offset procedure with multiple rotations of the fan-beam scanner.

The theoretical basis for a multiple rotation fan-beam scanner was first given by Peters and Lewitt [Peters and Lewitt, 1977]. In order to better understand the data collection procedure of such a device only three detectors are considered in the analysis. Figure 3.3.1 shows the fan-beam rotated from the reset position by an angle Ψ , the dotted lines show the fan-beam after the detector array is rotated by an additional small angle γ about the source. ϕ is the angle between detectors, θ and r are the angular and radial positions of ray S'-3 considered in the equivalent parallel-beam format. If the angular sampling interval is equal to the inter-detector angle such that $\Psi = n\phi$ ($n=1$ to $360/\phi$) then for the centered fan-beam:

$$\sigma = m\phi \quad m = -1, 0, 1 \quad (3.3.2)$$

$$\theta = n\phi + m\phi \quad n = 0, 1, 2, 3, \dots, (360/\phi) \quad (3.3.3)$$

$$r = SCR \sin(m\phi) \quad (3.3.4)$$

where SCR is the source to center-of-rotation distance and σ is the radial co-ordinate of a detector measured as an angle between the SCR line and the detector ray.

The ray-sum P for a detector with radial sample position σ , collected between 0° and 180° , is the same as that for a detector with radial sample position $-\sigma$, collected between 180° and 360° such that:

$$P(\sigma, \theta) = P(-\sigma, \theta + 180^\circ) = P(\sigma, \theta + 360^\circ) \quad (3.3.5)$$

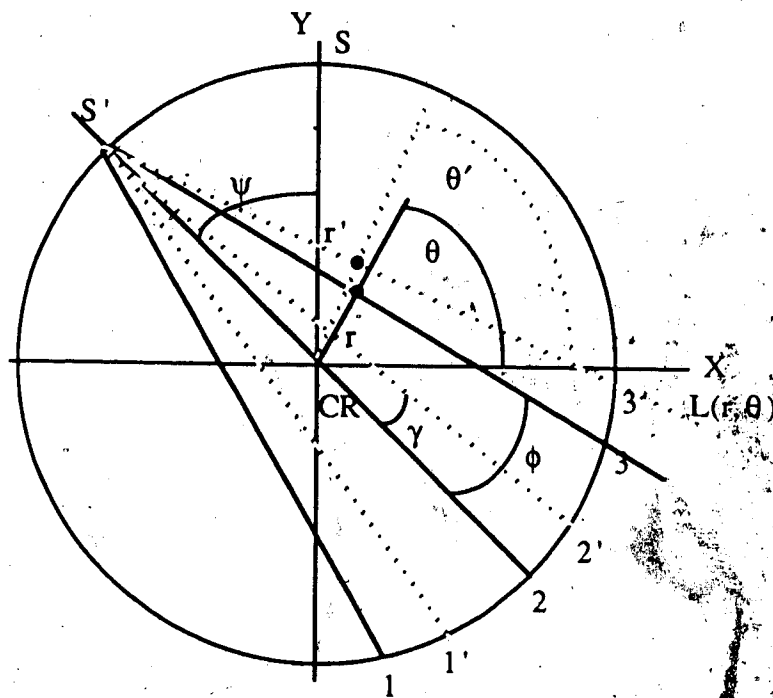


Figure 3.3.1: Fan-beam after a rotation from the reset position. Dotted lines show fan-beam after a rotation of the detectors about source.

Figure 3.3.2(a) shows how the sample space (σ, θ) is filled when the scanner is rotated by 360° . It can be seen that rotating the scanner by 360° collects data twice at the same (σ, θ) values. It can also be shown [Peters and Lewitt, 1977] that for complete data collection for a fan-beam scanner, a rotation of slightly more than 180° ($180^\circ + \text{fan angle}$) is required. A further rotation up to 360° is therefore pointless since it will repeat the already known data samples.

After rotating the detectors by a small angle γ about the source, the radial and angular co-ordinates of the fan-beam in an equivalent parallel beam format, are given by:

$$\sigma = m\phi + \gamma \quad (3.3.6)$$

$$\theta = n\phi + m\phi + \gamma \quad (3.3.7)$$

If the scanner is rotated by 360° the (σ, θ) sample space will be filled as shown in figure 3.3.2(b). Since the detector angles about the SCR line are no longer symmetrical, the radial position of detector 1 between 0° and 180° will not be the same as that of detector 3 between 180° and 360° (Figure 3.3.1). Data points collected at the same angular position ($\Psi = n\phi$) of source are shown connected (Figure 3.3.2(b)), showing that a rotation of 360° would give two samples per detector at each angular co-ordinate θ .

Figure 3.3.3(a) shows the asymmetrical fan-beam 1-S-3 (dotted lines) and the same fan-beam linearly shifted by a distance S-S' perpendicular to the SCR line (thick lines). If the fan-beam is given a linear shift in a direction perpendicular to the SCR axis, then the angular position of a ray does not change (Figure 3.3.3(a) rays S-3 and S'-3'). However, the radial position of the rays with respect to SCR axis is changed such that a detector will collect data at different radial co-ordinates but with the same angular co-ordinates. For example in Figure 3.3.3(a), the arc-length of detector 3 from the SCR axis before and after the linear shift of the fan-beam, is given by O-3 and O-3' respectively. A linear shift of the

fan-beam has changed the radial distance of detector ray S-3 from CR-r to CR-r' which is equivalent to an arclength of β .

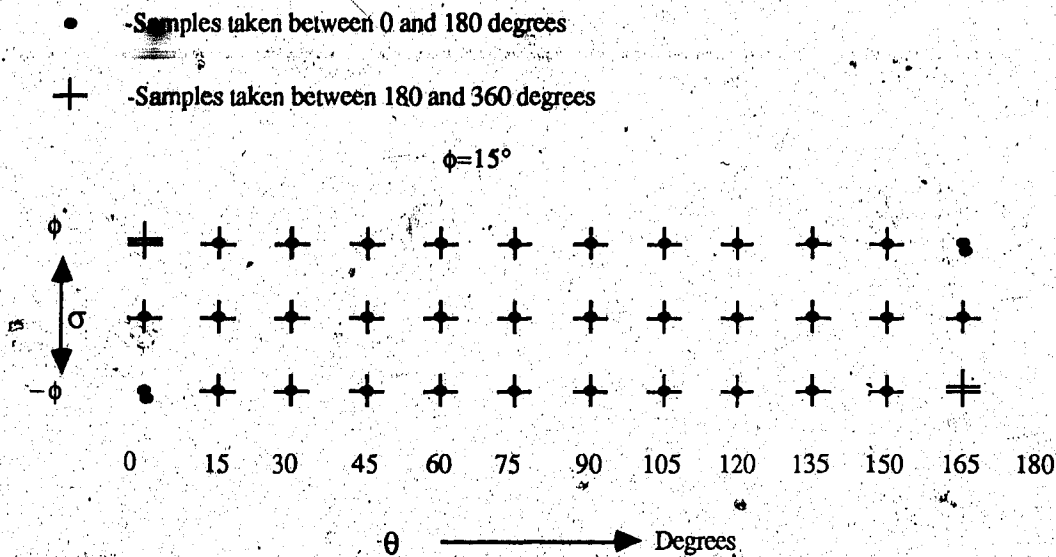


Figure 3.3.2(a): (σ, θ) Sample space for centered fan-beam

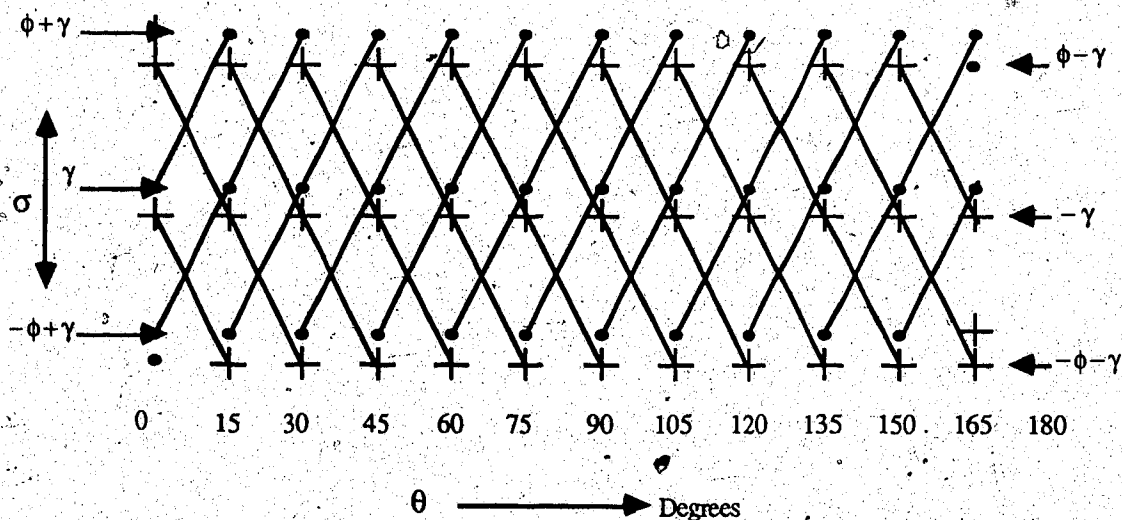
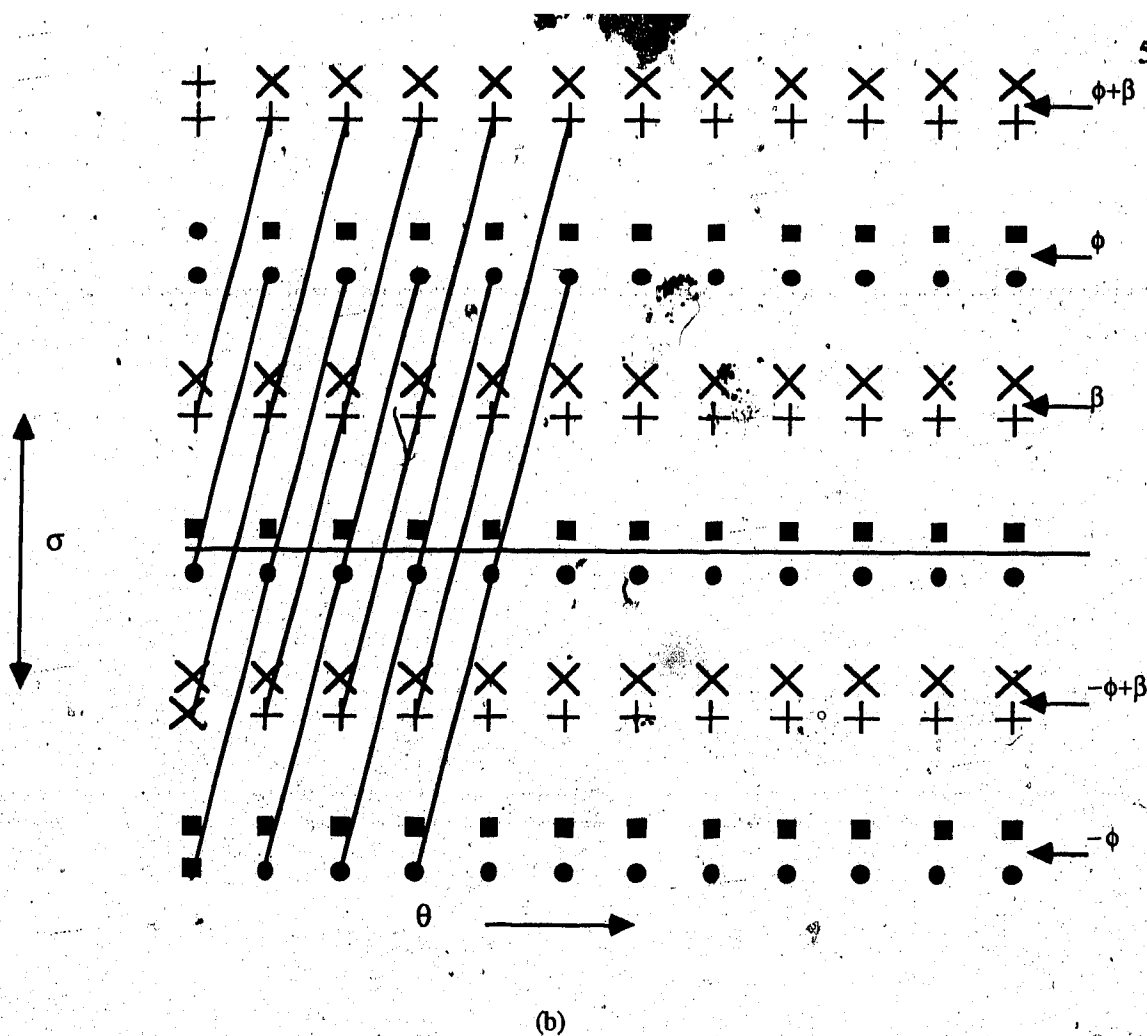


Figure 3.3.2(b): (σ, θ) Sample space for fan-beam after a small rotation of detectors about the source.
 The samples at the four corners are due to wrap around within a 180° rotation (either 0° - 180° or 180° - 360°)



- -Samples collected between 0° and 180° in first rotation
- -Samples collected between 180° and 360° in first rotation
- × -Samples collected between 0° and 180° in second rotation
- ⊕ -Samples collected between 180° and 360° in second rotation

Figure 3.3.3 (b): The (σ, θ) space for two rotations of an asymmetrical fan-beam; β is the shift in the radial co-ordinates of detector rays due to a linear shift of the fan-beam in the second rotation. The samples at the top-left and bottom-left corners are due to the wrap around within a 180° rotation (either 0 - 180° or 180 - 360°)

where n is the number of detectors. For example, the three detectors provide 12 $(2 \times 3 \times 2)$ radial sampling positions for each angular co-ordinate in figure 3.3.3(b). Hence the number of radial samples per detector can be increased by properly shifting the fan-

beam and rotating the scanner more than once. For our particular CT scanner, the initial offset of the detectors from the SCR axis involves movement of three motors as shown in figure 3.3.4.

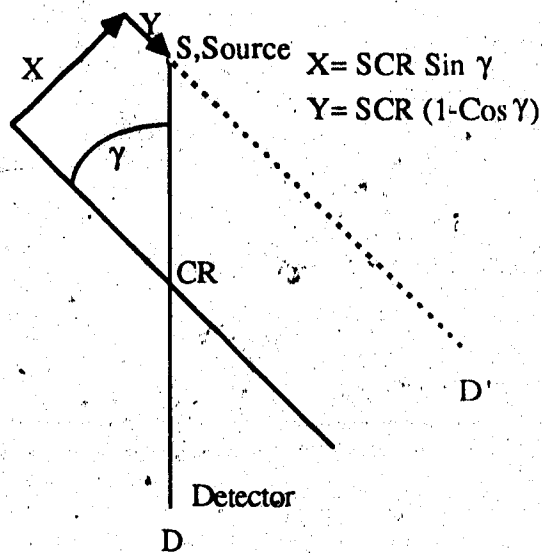


Figure 3.3.4: Equivalent linear shifts for a rotation of detector about the source.

The scanner is rotated five times with a different linear shift X in each rotation. In each rotation data is collected at $2/3^\circ(\phi)$ intervals for each of 26 detectors, giving 260 $(2 \times 26 \times 5)$ radial samples in each angular view. As the data collected between 180° to 360° is folded back between 0° and 180° , there are 270 equivalent parallel views available $(180/\phi)$. It should be noted that to keep the detectors in order within a 260-point profile, the linear shift given to the fan-beam must not exceed the ray-spacing of the detectors. The fan-beam in each successive rotation is therefore linearly shifted by one fifth of the ray-spacing.

The data collection procedure for this CT scanner takes about one minute (five rotations). The scan time can be reduced by increasing the speed of rotation but this involves an increase in photon fluence from the X-ray tube! However, the existing NaI(Tl) detectors start saturating at about 750,000 counts/second, so any improvement in the scan

time would require a different detector system with a smaller inherent dead-time than

$N(t)$.

3.3.2 Image Reconstruction.

The geometry of the X-CT scanner suggests the use of a direct fan-beam reconstruction algorithm, however, in such a scheme the first completed fan-beam projection is available only after the fifth rotation. We decided, therefore, to use a parallel beam reconstruction algorithm along with an efficient scheme for re-binning the fan-beam projections into parallel projections. Our reconstruction procedure is faster than direct fan-beam reconstruction which requires a back-projection operator dependent upon the distance between the source and the point at which a pixel value is reconstructed [Herman and Lakshminarayanan, 1976].

The data collection process determines the number of photons counted by each detector in all rotations. Considering the ray S-3' in figure 3.3.1, a projection ray-sum is calculated as follows:

$$P(r, \theta) = \ln \left(\frac{I_0(r, \theta)}{I(r, \theta)} \right) = \int_{L(r, \theta)} \mu(x, y) dl \quad (3.3.9)$$

where $\mu(x, y)$ is the linear attenuation coefficient of the material in the x-y plane, $L(r, \theta)$ is the ray path of the X-ray beam from source to detector, $I(r, \theta)$ and $I_0(r, \theta)$ are photon fluxes counted by the detector at r, θ radial and angular co-ordinates, with and without the object in the scanning field respectively.

The counts I_0 and I are corrected for dead-time and background counts before the projection ray-sums are calculated as discussed in sections (3.2.2 and 3.2.3). These ray-sums are then corrected for beam hardening and reordered into an equivalent parallel

projection. As previously discussed, the fan-beam geometry collects data along diagonal lines in (σ, θ) space. A reference co-ordinate system is set-up and the angles of the detectors with respect to the SCR line are determined in this system. The angular position θ of the parallel views is then determined from the angle of rotation, initial rotation of the detectors about the source and the angles of the detectors. The radial position of the detectors is given by the detector angles, the initial offset of the fan-beam about the source and the linear offset of the fan with respect to the SCR line. As shown in figure 3.3.3(b), data for a constant angular position along the σ axis is from a parallel projection. If the angular co-ordinate θ is more than 180° , it is folded back between 0° and 180° and the radial position is determined from equation (3.3.5).

The re-ordered parallel projection consists of irregularly spaced samples, and the position of a sample from the center of a projection is given by the following equation:

$$r = SCR \sin(m\phi + \gamma) + k\Delta l \cos(m\phi + \gamma) \quad (3.3.10)$$

where Δl is the linear offset of the fan-beam and k is the integral multiplier indicating the rotation number. A regularly spaced, 256-point profile is generated by a first order interpolation from the re-binned, unequally spaced profile. The final step in reconstructing the image is to convolve and back-project the 256-point profiles, spaced at $2/3^\circ$ intervals, according to the following equations:

$$f(x, y) = \frac{2N}{M} \sum_{\phi} \sum_{r'} P(r, \theta) * G(r-r') \quad (3.3.11)$$

$$G(r-r') = 1 \quad ; r=r'$$

$$= \frac{-1}{(4|r-r'|^2 - 1)} \quad ; r \neq r' \quad (3.3.12)$$

where $G(r-r')$ is a 256-point numerical version of the Shepp and Logan convolution kernel [Shepp and Logan, 1974]. N is the number of samples in a profile and M is the number of profiles rebinned from the fan-beam data. In the back-projection, a linear interpolation is used for samples not falling on the grid points.

The number of parallel views required is determined by the size of the reconstruction matrix, the size of the object and the required spatial resolution. If N (pixels) is the diameter of the circle of reconstruction, then the number of pixel elements, P_N , is given by:

$$P_N = \frac{\pi N^2}{4} \quad (3.3.13)$$

and if N is also the number of samples in a profile, then number of profiles to determine all the pixel elements is given by:

$$M = \pi \frac{N}{4} \quad (3.3.14)$$

For this CT scanner M is equal to 202, which is less than the 270 collected, so the requirement for the matrix size is more than satisfied. Since the profiles for all angles are added to give a pixel in the image, the precision of pixel values improves by collecting 270 instead of 202 profiles [Peter and Lewitt, 1977].

4.0 Analysis Procedures for High Precision Measurement of TBD using CT

The variation in spatial distribution of trabecular bone in man and in animals emphasizes the importance of using a highly reproducible volume of trabecular bone in a longitudinal study of bone mass. Thus a precise location of the CT measurement site, and a reproducible determination of bone contours is necessary to analyze an identical volume of bone in a serial study. In this chapter, the technique for repositioning bone in the CT scanner is outlined, and a brief analysis of bone contour detection and volumetric TBD determination procedures is given.

4.1 Reproducibility of the Measurement Site

For the distal radius it has been demonstrated that cross-sectional bone area can change by up to 6% per mm change in axial position along the bone [Hangartner and Overton, 1982]. The average TBD within a transaxial slice of the distal radius changes up to 5% per mm change in axial position. For the distal femur the TBD and the bone area also depend strongly upon the axial location of the measurement, Figure 4.1.1. The determination of a reproducible measurement site is thus extremely important for the study of bone mass at axial as well as at appendicular skeletal sites [Hangartner and Overton, 1982; Cann and Genant, 1980].

Localization of a measurement site is made possible by the use of a scan projected digital radiograph, known as a 'scout view'.

The patient is positioned using a laser cross-hairs system such that the start position is about 4cms above the center of the knee-cap. The data collection process for the digital radiograph uses the axial and horizontal movements of the scanner; data are collected for all 26 detectors as the collimated beam translates axially along the leg, then the fan-beam is linearly shifted to the right and the data is collected again. A set of transmission measurements is made for five such translations with a linear shift of the fan-beam made

before each translation, so a profile of 130 radial positions is available at each horizontal position.

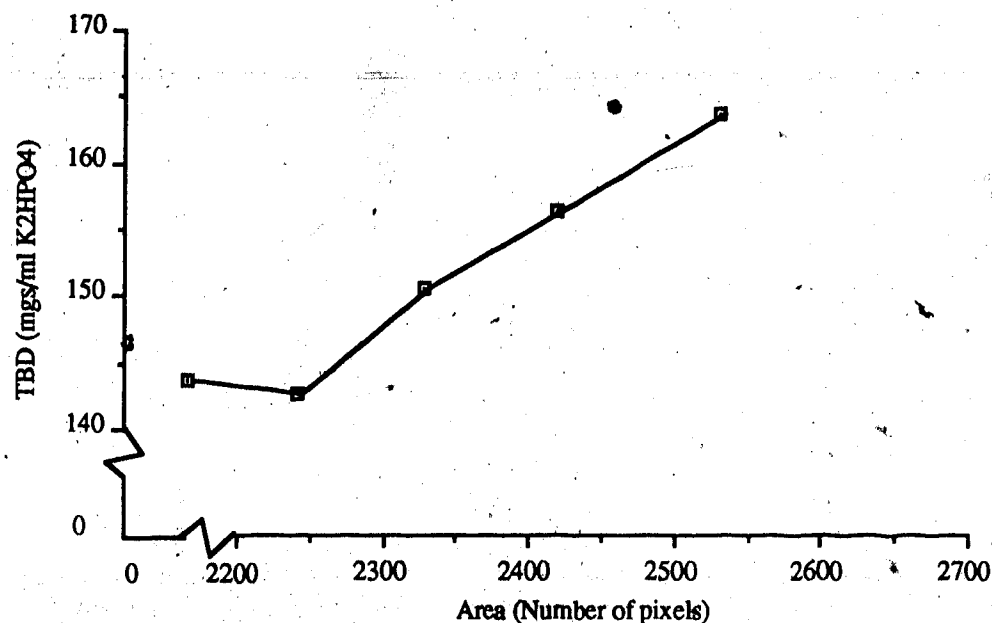


Figure 4.1.1

Trabecular bone density at distal femur site expressed as relative K_2HPO_4 solution concentration as a function of bone area. The slices are taken at 4 mm intervals proximal to the measurement site determined by 'SCOUT SCAN'.

Each profile provides a line in the two dimensional 'scout view'. The size of the linear shift of the fan-beam used in this scout scan is the same as that used in the data collection procedure for a tomographic image (section 3.3.1). The linear shift Δl of the fan-beam is equal to the one fifth of the detector spacing, given by:

$$\Delta l = \frac{2 \text{ SCR TAN}(\psi/2)}{125} \quad (4.1.1)$$

where ψ is the fan angle.

A 'scout view' illustrating the procedure for locating the measurement site is shown in Figure 4.1.2. It should be noted that this is not a true 'scout view' in that a fan-beam instead of a parallel projection is used as a single line in reconstructing the two dimensional

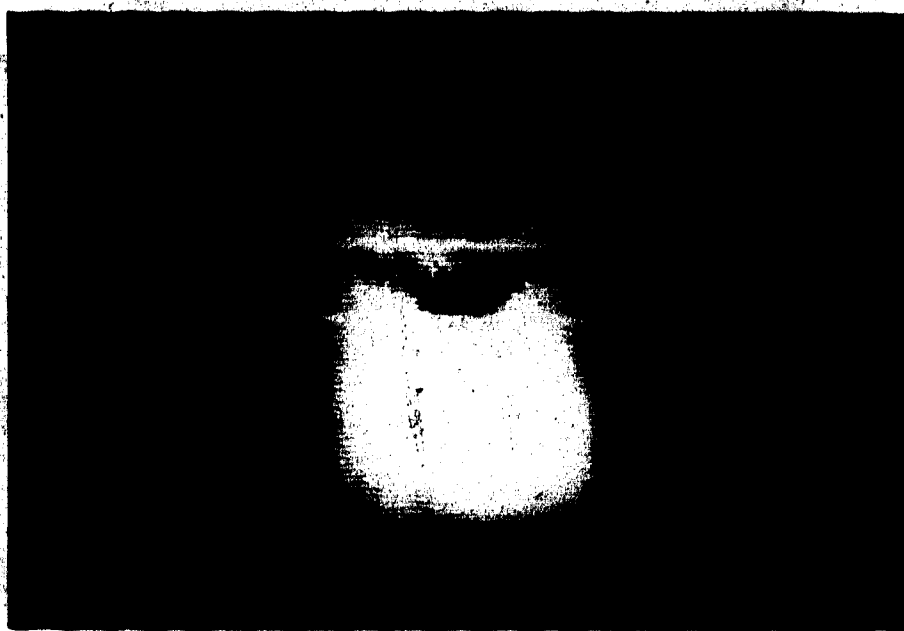


Figure 4.1.2

Scan projected digital radiograph of human knee: The two horizontal lines provide anatomical landmarks for repositioning the distal femur and the proximal tibia sites.

radiograph. This results in distortion of the 'scout view' in the transaxial direction.

However, since there is no distortion in the axial direction, the resulting image is analyzed to calculate the distance of the desired measurement site from the laser-beam cross-hairs position.

4.2 Reproducibility of Measurement Area

The distribution of trabecular bone varies spatially i.e. the volumetric fractions of collagen, mineral, soft tissue and fat are functions of the axial as well as transaxial position in the long bones. Hence, the measured TBD also depends on the volume of the trabecular bone taken for analysis. In a serial study of bone mass therefore, a precise reproduction of the measurement site is important, and an identical area of the bone cross-section must be used to calculate TBD. The reproducibility of bone area in a cross-section for TBD analysis is determined by the precision of the bone contour detection procedure.

4.2.1 Bone Contour Detection

After positioning the bone in the CT scanner and determining the axial measurement site from a digital radiograph, cross-sectional images are generated as a two-dimensional array of pixel elements representing the distribution of the linear attenuation coefficients within the section. Regions of similar pixels represent a specific tissue structure, for example, trabecular or cortical bone. In order to measure TBD the trabecular bone has to be identified as distinct from the cortical bone and the soft tissue surrounding the bone. In order to precisely quantify small density changes in trabecular bone over time an automated, objective procedure for bone contour detection is essential. In general the contour detection algorithm should have the following features:

- 1) The bone contour detection algorithm should automatically determine a unique and precise bone contour, without the intervention of an operator.

2) A serial study can only be carried out safely if the radiation dose is within prescribed limits. Therefore, noise in the CT image is generally high since statistical error is increased for a low incident X-ray flux. The contour detection algorithm should be more or less immune to this pixel noise.

3) It is known that bone remodeling activity (section 2.2.3) is greater on trabecular and cortical-endosteal envelopes than on the cortical Haversian and periosteal envelopes [Frost, 1986; Parfitt, 1979]. Due to the larger remodeling activity and a negative bone balance in each BSU (section 2.2.1) on the cortical-endosteal envelope, the marrow cavity increases in diameter with age. The periosteal envelope, on the other hand, undergoes very little remodeling so there is no significant bone change on the periosteal surface. Therefore, the outer diameter of the cortex of long bones remains constant, at least during relatively short study periods, e.g. 3 months. The bone contour detection algorithm should always determine this constant outer bone contour so that a constant area of the trabecular bone can be analyzed on each measurement occasion.

The images obtained with this CT scanner are 256x256 pixel arrays, and each pixel has 256 gray levels (0=black, 255=white). There are a number of different methods available to obtain precise and accurate contours within an image including: pixel classification; edge detection; region growing or partitioning; border following, and combinations of these [Rosenfeld and Kak, 1982; D'Amico, 1986]. To analyse femur images, Seitz and Rüeggsegger [1983] have used an automated and efficient algorithm based on the border following approach, along with local filtering operations to reduce the effect of noise.

The bone finding algorithm currently used with the γ -CT system [Hangartner and Overton, 1982] is based on a combination of pixel classification and spatial frequency filtering (median, Laplacian) operations. This algorithm detects all edges in the complete image resulting in several 'artifact' contours, along with the cortical bone contour, since the Laplacian operation is very sensitive to noise. On occasion the resulting cortical bone

63
contour is not perfectly closed and the operator has to remove unwanted objects present in the contour image and repair the desired bone contour using an interactive graphics system. The reproducibility of the bone area is greatly affected by these interactions and the analysis time is increased.

A substantial operational improvement with decreased analysis time and more efficient contour detection have resulted from the work of D' Amico [D'Amico, 1986] who developed an automated procedure known as 'Edge Detection by Cross-correlation of Radial Profiles' (EDCORP). This algorithm has been modified and implemented for this X-CT scanner.

The complete "bone find" (BOFI) analysis process can be divided into three major parts.

4.2.1 (a) Pre-BOFI

EDCORP is successful in establishing reliable contours 98% of the time, however, it can fail to give an accurate bone contour in cross sections which contain two bones, for example distal radius and ulna or proximal tibia and fibula. The function of the pre-BOFI process is to identify a 128x128 pixel image containing the desired bone section from the entire image. This is done using a track ball to move a 128x128 frame over the image and centering the frame over the desired bone area. If a 128x128 frame still contains a part of undesired bone, it can be removed manually with the help of the track ball. The EDCORP operation is then repeated with the framed image and the center of the frame gives the initial origin of the radial profiles.

4.2.1 (b) Auto-BOFI

This is a modified version of the EDCORP algorithm and normally is the first process to operate on the image to find the bone contours. This algorithm was developed to specifically find the contour in low dose CT images of the long bones at appendicular skeletal sites. A brief description of this algorithm is given in the following section; a

complete theoretical and operational description is given in the original manuscript [D'Amico, 1986].

The two types of CT images which are analyzed by the EDCORP algorithm are shown in Figures 4.2.1 and 4.2.2. The center of intensity of the image for pixels of values above a certain threshold is determined. For a cross-section of the proximal tibia and fibula (Figure 4.2.2) the center of intensity falls in between the two bones. Pixels situated below the determined center of intensity are zeroed, and a new center of intensity for the resulting image is determined. This is done in order to remove the fibula in proximal tibia cross-section, and to ensure that the new center of intensity falls inside the desired bone cross-section. For a distal femur image, the center of intensity is within the bone of the image because of the selected threshold. This center of intensity is taken as a first approximation for the origin of radial profiles of the desired bone cross-section. A radial profile consists of pixel elements along a line originating from the center of the bone cross-section, and extending towards and through the cortical bone into the surrounding soft tissue.

The profile at 0° is cross-correlated with a known correlation kernel - an idealized edge profile in this case. In order to compensate for blurring due to finite beam width, the reconstruction process and noise, the correlation kernel is measured from CT images of a phantom containing K_2HPO_4 solution in an inner aluminum cylinder [Figure 5.1.1]. The cross-correlation function from the correlation operation of the bone profile with this kernel has a maximum at the bone edge, and so the co-ordinates of the contour at this angle can be determined by calculating the position of this maximum value. A typical radial profile in a bone image is shown in Figure 4.2.3 along with the correlation kernel and the resulting correlation function. The position of the edge in the contour is determined by finding the cross-correlation function for the profiles at all angles. At this stage, a first approximation of the bone contour is available if the determined contour is a closed one. If this contour is not closed, the same process is repeated using a wider window for the cross-correlation



Figure 4.2.1
CT image at a distal femur site in a normal male subject.

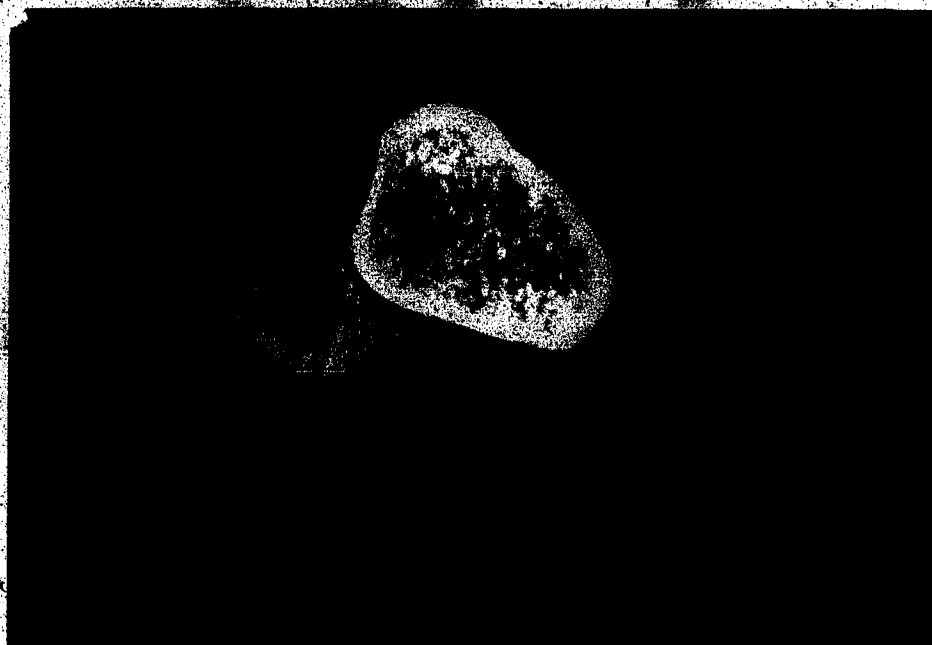


Figure 4.2.2
CT image at a proximal tibia site in a normal male subject.

kernel. If the contour determined using a wider kernel window is not closed, then the algorithm has failed and the operator has to use the Pre-Bofi method described earlier.

In 98% of the cases, however, a closed contour is available with the EDCORP process and the center of intensity of this contour determined. If this new center of intensity differs in position from the origin of the radial profiles, then the new center of intensity is taken as the new origin for radial profiles and the whole process is repeated a maximum of seven times, or until the center of intensity and the origin of the radial profile match. The last contour determined is taken as the outer contour of the cortical bone. If the center of intensity of the contour has not stabilized within seven cycles then an error message is displayed. Figures 4.2.4 and 4.2.5 show the contour determined for the femur and tibia images of Figure 4.2.1 and 4.2.2 respectively.

A bone mask is then prepared with the help of the calculated contour, and an image with negative pixels outside the contour is produced and stored in a file for further processing.

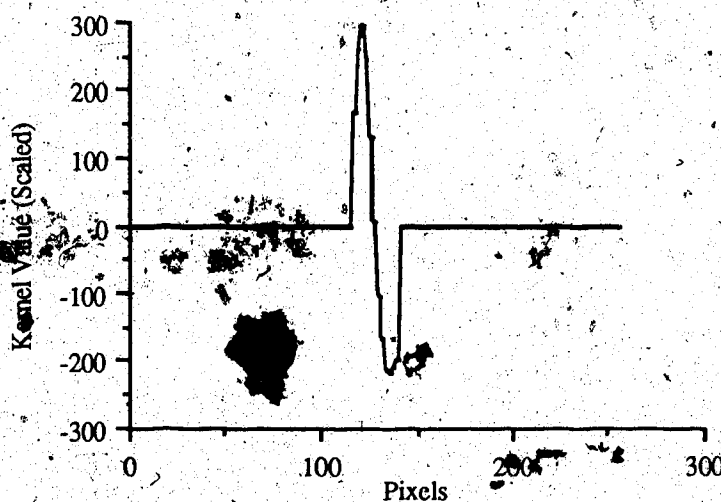


Figure 4.2.3(a): The cross-correlation kernel used in EDCORP algorithm.

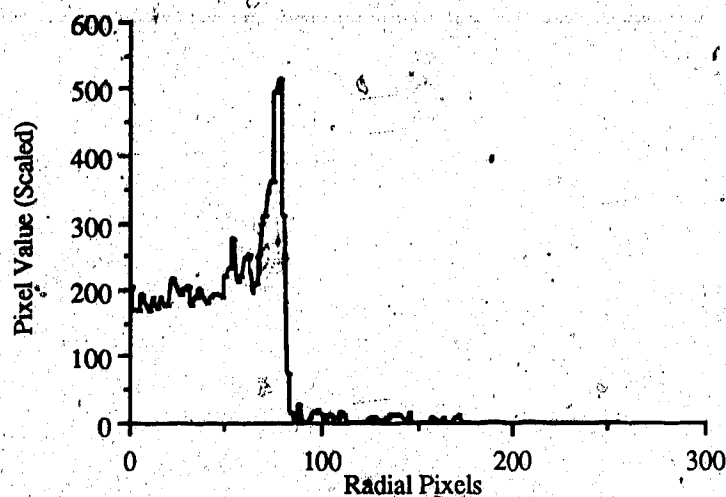


Figure 4.2.3(b): The radial profile from an image of the distal end of a cadaver femur.

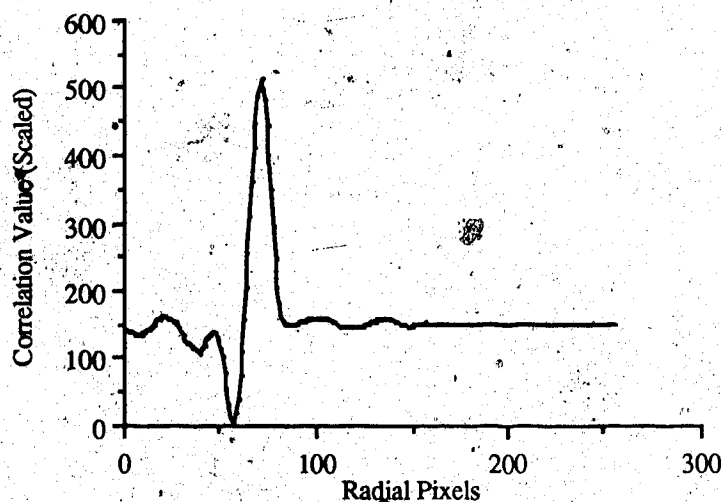


Figure 4.2.3(c): The correlation function resulting from cross-correlating (a) and (b).

4.2.1 (c) Post-BOFI

There are occasions when EDCORP fails to yield a bone contour; this occurs if the bone edges determined by cross-correlation of radial profiles do not belong to a closed contour, for example. There are circumstances when a bone contour determined by this

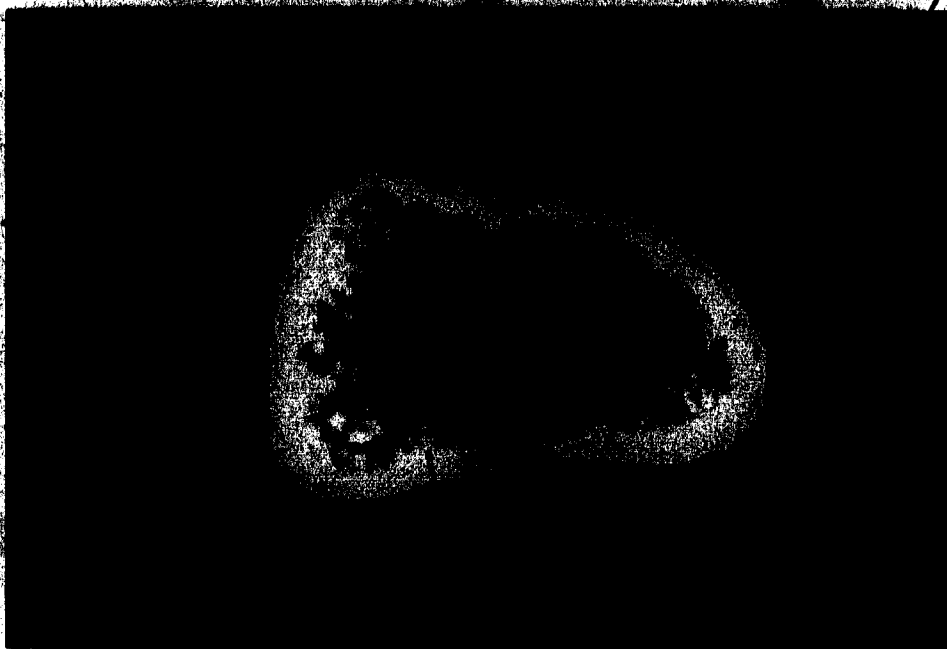


Figure 4.2.4
Distal femur image of figure 4.2.1 with the cortical bone contour outlined.



Figure 4.2.5
Proximal tibia image of figure 4.2.2 with cortical contour of tibia bone outlined.

method may not accurately represent the outer cortical bone surface, for example if the fibula is too close to the tibia and is not completely removed in the analysis process.

The function of the Post-BOFI system is to display the detected contour along with the image of the cross-section in order for the operator to decide upon the accuracy of the contour. If EDCORP failed due to incomplete removal of the second bone, the Post-BOFI process automatically regenerates the Pre-BOFI process and the operator manually corrects the bone separation using a track-ball. If EDCORP fails due to image noise then the operator can specify the use of a Laplacian operator method for edge detection. The Post-BOFI system also formats the data for use by the TBD analysis program.

4.3 TBD Analysis

When the desired location of the measurement site is found a contiguous set of non-overlapping 2mm slices is reconstructed both for the distal femur and proximal tibia. In order to calculate the volume average TBD at the distal femur and proximal tibia, a set of 10 slices are measured at each of the measurement sites. The calculation of TBD requires the measurement of the mean pixel values within a specified area of the trabecular bone. The area enclosed by the outer contour of the cortical bone is taken as the total bone area for a particular image section. The pixel values within this area are used to calculate the volume average TBD using all the measurements for a particular site, e.g. the distal radius, distal femur, proximal tibia. A simple and brief description of the steps involved in this analysis is given here.

The analysis is performed separately for each of the measurement dates. For all images taken on a particular date, the number of pixels within the inner 45% area of the bone contour are calculated along with the mean value of pixels within this area. This area is assumed to be occupied by trabecular bone [Hangartner et al., 1985]. The mean pixel values are used, along with the corresponding values for the standard solutions, to calculate the TBD. The various procedures for computing TBD from the mean pixel values are given

in section 5.0.

A second or third order polynomial is then fitted to the TBD vs. area data and a linear or second order polynomial is fitted to the position vs. area data of all the dates. If the functions $T(A)$ and $P(A)$ give the TBD and position as a function of area respectively, the volume average TBD, T_V , can then be calculated from the following expression:

$$T_V = \frac{\int T(A) P'(A) A \, dA}{\int P'(A) A \, dA} \quad (4.3.1)$$

where $P'(A)$ is the first derivative of the position vs. area function with respect to the area, A .

Operator defined lower and upper area limits are used in the calculation to determine the volume averaged TBD and these same limits are used in the analysis of all measurement dates for a particular patient. The volume averaged TBD for the first measurement date is taken to be the base TBD. For all the subsequent measurement dates changes in TBD are calculated with respect to this TBD base.

The discussion in the previous paragraph describes the procedure for reporting TBD. However, the actual implementation has additional features, e.g. measurements which have image artifacts can be excluded from the analysis, for more details refer to the operating manual for isotope CT scanner [Hangartner and Overton, 1982; Hangartner et al., 1985].

5.0 Methods for Bone Mass Measurement using CT

The pixel values in the CT images which represent the linear attenuation coefficients of bone are related to the bone mineral content. We describe here the techniques used to determine the trabecular bone mineral content from the single and dual photon energy measurements of linear attenuation coefficients of trabecular bone.

5.1 Single Energy Method for Bone Mass Measurement by CT(SECT)

Trabecular bone tissue consists of mineralized collagen fibers and intervening spaces containing hematopoietic tissue (red marrow) and fatty tissue (yellow marrow). The single energy method for TBD measurement, in general, assumes a two component tissue model for the trabecular bone: bone mineral, and marrow or non-mineral. The bone mineral component consists of the collagen and mineral; the marrow component consists of the fat and soft tissue. Since collagen and mineral have a fixed distributional relationship (about 1:2 by volume) for both normal and osteoporotic bones [Woodard, 1964], they can be combined into a single component, i.e. bone mineral. However, combining fat and soft tissue as a single component, i.e. marrow, is not generally correct, since the amount of fat is variable.

There are two approaches to the measurement of TBD by SECT.

- (a) Volume fractions approach.
- (b) Concentration approach.

5.1.1 Volume Fractions Method

Let μ_b , μ_s and μ_f be the linear attenuation coefficients of bone mineral, soft tissue (red marrow) and fat tissue (yellow marrow) respectively. Let X_b , X_s and X_f be the volume fractions of bone mineral, soft tissue and fat, respectively, present in unit volume of the trabecular bone tissue. CT measures the linear attenuation coefficient of the trabecular

bone tissue which is a weighted average of the three components. Therefore:

$$\mu = \mu_b X_b + \mu_s X_s + \mu_f X_f \quad (5.1.1)$$

$$1 = X_b + X_s + X_f \quad (5.1.2)$$

where μ is the linear attenuation coefficient of trabecular bone tissue.

The dimensionality of variables in equations (5.1.1) and (5.1.2) can be reduced by assuming a fixed volume relationship between soft tissue and fat present in the trabecular bone tissue [Hangartner and Overton, 1982].

Let μ_m be the linear attenuation coefficient, and X_m the volume fraction of the marrow component, which is a combination of the soft and fatty tissues.

Equations (5.1.1) and (5.1.2) can be written as:

$$\mu = \mu_b X_b + \mu_m X_m \quad (5.1.3)$$

$$1 = X_b + X_m \quad (5.1.4)$$

From equations (5.1.3) and (5.1.4) the volume fraction of the bone mineral is given by:

$$X_b = \frac{1 - \mu_m}{\mu_b - \mu_m} \quad (5.1.5)$$

Let ρ_b, ρ_m be the physical densities of pure bone and marrow respectively, then TBD is given by:

$$\begin{aligned} \text{TBD} &= \rho_b X_b + \rho_m (1 - X_b) \\ &= \rho_b \frac{\mu - \mu_m}{\mu_b - \mu_m} + (1 - \frac{\mu - \mu_m}{\mu_b - \mu_m}) \rho_m \end{aligned} \quad (5.1.6)$$

In a short term serial study only the changes in the TBD are considered important; the

density of the marrow portion of the trabecular bone tissue is therefore assumed to be zero to simplify the TBD calculations. In this case TBD is given by:

$$TBD = \rho_b \frac{\mu - \mu_m}{\mu_b - \mu_m} \quad (5.1.7)$$

TBD can therefore be measured if the values of the parameters μ_b , μ_m , ρ_b and ρ_m are known.

The physical density and the linear attenuation coefficient of trabecular bone mineral are the same as for compact bone mineral. The physical density and linear attenuation coefficient of marrow are calculated by assuming a fixed composition e.g. 70% soft tissue and 30% fatty tissue or 40% soft tissue and 60% fatty tissue by volume [Hangartner and Overton, 1982]. If the assumptions regarding the composition of the marrow and the bone are accurate, TBD can be measured in an absolute sense.

This method cannot be used with CT scanners which use an X-ray photon source since the linear attenuation coefficients of the pure components of trabecular bone tissue are not known due to the polychromatic nature of the beam of X-ray spectrum.

5.1.2 Concentration Method

The quantity of bone mineral present in unit volume of trabecular bone tissue is measured in terms of an equivalent K_2HPO_4 (or calcium hydroxyapatite) solution. Let μ_b , μ_s , μ_f be the mass attenuation coefficients, and C_b , C_s , C_f the concentrations in terms of gm/ml, of bone mineral, soft tissue and fat components of the trabecular bone tissue respectively. The linear attenuation coefficient of the trabecular bone tissue is therefore given by:

$$\mu = C_b \mu_b + C_s \mu_s + C_f \mu_f \quad (5.1.8)$$

Equation (5.1.8) can also be written as:

$$\mu = \mu_w (F_b C_b + F_s C_s + F_f C_f) \quad (5.1.9)$$

where μ is the linear attenuation coefficient of the trabecular bone tissue measured by CT and μ_w is the linear attenuation coefficient of pure water. The parameters F_b , F_s and F_f are the mass attenuation coefficients, relative to water, of bone mineral, soft tissue and fat respectively. Let C_{nm} be the concentration of the total non-mineral component (soft tissue + fat), and FFC the fractional fat content of the total non-mineral component. The concentrations of the soft tissue and fat can be expressed as:

$$C_s = (1 - \text{FFC}) C_{nm} \quad (5.1.10)$$

$$C_f = \text{FFC} C_{nm} \quad (5.1.11)$$

Substituting the values of C_s and C_f , equation (5.1.9) can be re-written as:

$$\mu = \mu_w (F_b C_b + F_{nm} C_{nm}) \quad (5.1.12)$$

where F_{nm} is the mass attenuation coefficient of the total non-mineral component relative to water and given by:

$$F_{nm} = (1 - \text{FFC}) F_s + \text{FFC} F_f \quad (5.1.13)$$

The concentration of bone mineral C_b can be determined from equation (5.1.12):

$$C_b = \frac{\frac{\mu}{\mu_w} - F_{nm} C_{nm}}{F_b} \quad (5.1.14)$$

For a pure bone-like mineral solution e.g. K_2HPO_4 , of known concentration C_k equation (5.1.14) can be written as:

$$C_k = \frac{\frac{\mu_k}{\mu_w} - C_w}{F_b} \quad (5.1.15)$$

where μ_k is the linear attenuation coefficient of the mineral solution measured by CT.

It has been assumed that the radiological attenuation for the mineral solution is the same as that of bone mineral. In a mineral solution the non-mineral component is water, therefore F_{nm} is equal to unity and C_{nm} can be replaced by the concentration of water C_w .

Equations (5.1.14) and (5.1.15) can now be used to find the unknown bone mineral content in terms of the mineral solution:

$$C_b = C_k \frac{\frac{\mu}{\mu_w} - F_{nm} C_{nm}}{\frac{\mu_k}{\mu_w} - C_w} \quad (5.1.16)$$

Since the values of F_{nm} and C_{nm} for trabecular bone tissue, and of C_w for the mineral solution are not known the following approximations are made to simplify equation (5.1.16):

- 1) The non-mineral component of the bone is radiologically equivalent to water and its concentration is equal to 1.0 gm/ml.
- 2) The concentration of water in the mineral solution is almost equal to its density such that:

$$F_{nm} C_{nm} \approx C_w \approx 1.0$$

The bone mineral concentration is then given by:

$$C_b = C_k \frac{\mu - \mu_w}{\mu_k - \mu_w} \quad (5.1.17)$$

The parameters μ_k and μ_w are determined by scanning samples of pure water and a mineral solution of known concentration (see section 5.1.3). Therefore, using equation (5.1.17), the linear attenuation coefficient of the trabecular bone tissue can be expressed in gm/ml of K_2HPO_4 equivalent to the trabecular bone tissue density. This method has been used extensively to find the mineral content of vertebral trabecular bone [Cann and Genant, 1986; Nickoloff and Feldman, 1985; Rao et al., 1987; Goodsitt and Rosenthal, 1987].

The volume fraction method quantifies TBD by measuring the volume fractions of

the bone and marrow. The concentration method measures the amount of bone mineral present in the trabecular bone in terms of an equivalent K_2HPO_4 solution concentration. In order to quantify the true TBD, changes in composition of marrow (or non-mineral) component should be taken into account. Since both approaches assume a constant composition for the marrow (or non-mineral), the values of TBD generated by both methods have the same physical significance.

The X-CT scanner uses polyenergetic photon source and therefore the linear attenuation coefficients of components of trabecular bone are not known. On the other hand, the linear attenuation coefficients of a standard mineral solution and water can be determined from the CT images. Therefore, the concentration method is used to quantify the TBD by the X-CT scanner.

5.1.3 Calibration for K_2HPO_4 Solutions

It should be noted that the concentration of the K_2HPO_4 solutions relate linearly to the pixel values measured by CT, except for a displacement error [Rao et al., 1987] which results in a decrease in the concentration of water when the concentration of mineral in the solution is increased. The pixel values are linearly proportional to the linear attenuation coefficients of the underlying material.

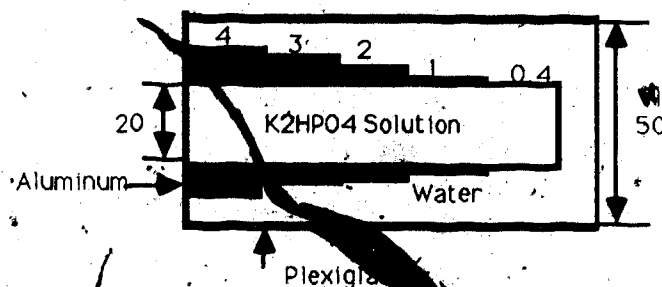


Figure 5.1.

Section through the cylindrical phantom, K_2HPO_4 solutions in varying percentage of ethyl alcohol are filled in the inner aluminum cylinder and section at 0.4 mm aluminum thickness is analysed in each case. dimensions in mm.

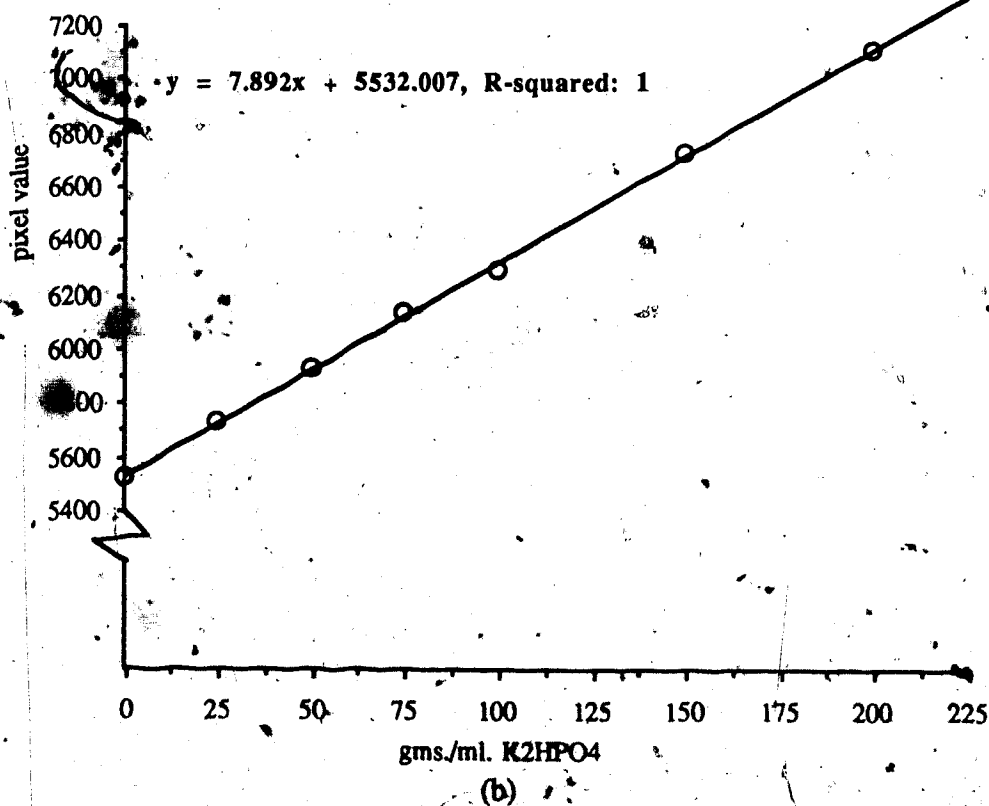
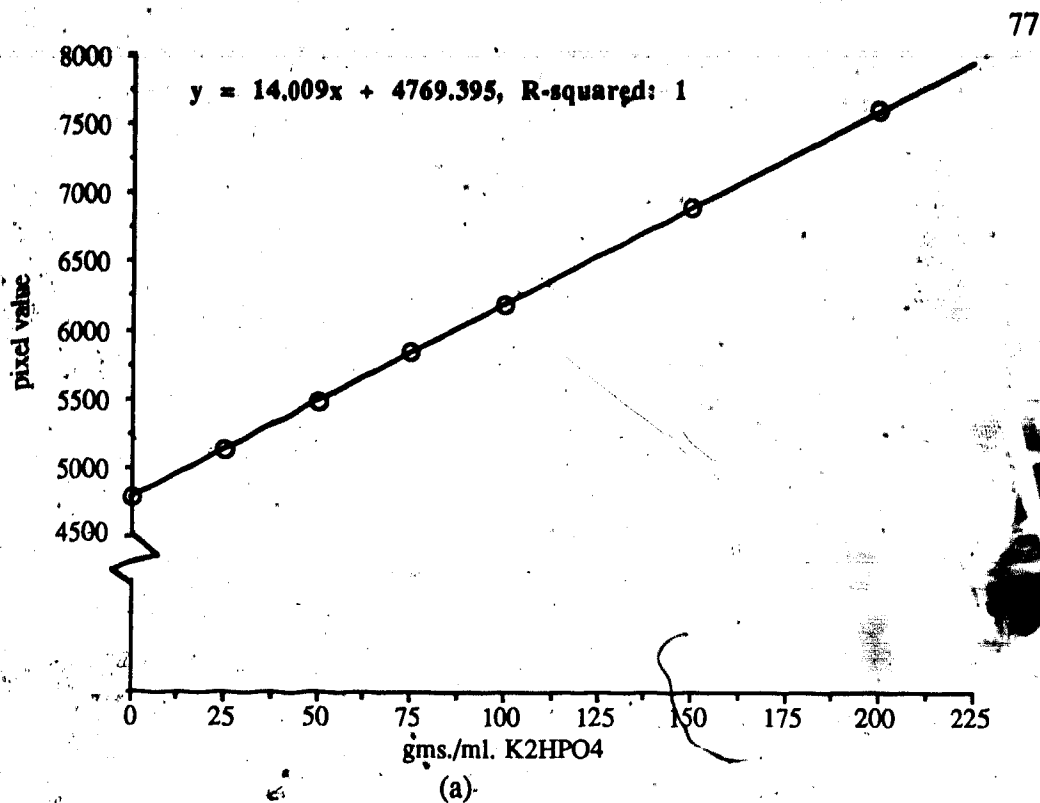


Figure 5.1.2: Mean pixel value vs. concentration of K₂HPO₄ solution scanned in a cylindrical phantom with X-ray tube potential (a) 50-kV and (b) 80-kV. The regression line equation and squared correlation coefficients are also shown.

Equation (5.1.17) can be used to calculate the bone mineral content if the pixel values of the water and mineral solutions are known. These pixel values are determined by scanning samples of mineral solution and water along with the bone. Since equation (5.1.17) assumes a linear relationship between the pixel values of mineral solutions and their concentrations, a large systematic error due to the displacement effect could be introduced. This effect would be exaggerated for TBD values significantly different from the concentration of the bone mineral solution. In order to correct for this error a number of different concentrations of mineral solution (0, 25, 50, 100, 150, 200 mg/ml of K_2HPO_4) were scanned. A phantom made of two concentric cylinders, Figure 5.1.1, was used for this calibration. The outer cylinder is plexiglass and is filled with water; the inner cylinder is aluminum and is filled with K_2HPO_4 solutions of various concentrations. This phantom was scanned and an image reconstructed. The mean value and standard deviation of all pixels, and the number of pixels within a circle of diameter less than the internal diameter of the aluminum cylinder with origin at the center of the reconstructed image, were determined using an automated analysis method. The standard error SE in the mean of the pixel values (95% confidence interval) is given by:

$$SE = \frac{1.96 SD}{\sqrt{N}} \quad (5.1.18)$$

where SD is the standard deviation and N the number of pixels.

Using a least squares procedure a line is fitted to the plot of mean pixel value vs. concentration of mineral solution. These fitted lines, at X-ray tube potentials of 50kV and 80kV, are shown in Figure 5.1.2. The equations of the lines and the squared correlation coefficients are also given. The standard errors for the intercept and the slope of the line are calculated as 0.06% and 0.18% respectively at 50kV and as 0.15% and 1.0% at 80kV.

Equation (5.1.17) can be written as:

$$C_b = \frac{\mu - \mu_w}{\frac{\mu_k - \mu_w}{C_k}} \quad (5.1.19)$$

The denominator is the slope of the calibration line, μ_w the intercept, and μ the mean pixel value of the trabecular part of the bone. The method of finding the average pixel value of the trabecular bone is described in section (4.2.2). Therefore, TBD is determined by equation (5.1.19) using the values for slope and intercept from the calibration line.

5.2 Dual Energy CT (DECT) for Bone Mass Measurement

The linear attenuation coefficient and the density of fat are less than the corresponding values for water, therefore, bone mineral content measured by the concentration method with SECT decreases as the fractional fat content in the trabecular bone increases [Sorenson and Mazess, 1970; Mazess, 1983; Laval-Jeantet et al., 1986]. Thus, the bone mineral measurement includes an error (5 to 50%) [Hangartner et al., 1985] because the fat content in the trabecular part of the bone is not known. Dual energy CT has been shown to reduce this error [Genant and Boyd, 1977; Nickoloff and Feldman, 1985; Laval-Jeantet et al., 1986; 1984; Goodsitt and Rosenthal, 1987]. DECT analysis of bone is particularly useful in cross-sectional studies when accuracy is more important than precision. However in serial studies when loss of bone is accompanied by a change in fatty marrow fraction [Mazess, 1983], DECT analysis provides particularly useful, additional information.

SECT analysis at lower energies (30-40 keV) is only slightly affected by changes in fat content [Genant and Boyd, 1977]. However, dual energy CT theoretically quantifies both the mineral and the non-mineral components, and can be used to measure the trabecular bone mass more accurately.

There are two types of dual energy methods for bone mineral analysis: the post-processing method, and the pre-processing method.

5.2.1 Post-processing Method

The post-processing analysis is carried out on the reconstructed images of a bone cross-section at two X-ray beam energies. The linear attenuation coefficient of trabecular bone is a weighted average of the linear attenuation coefficients of the mineral and non-mineral components in proportion to their respective concentrations. Hence, the mineral and non-mineral contents of the trabecular bone can be determined from the linear attenuation coefficients measured at two photon energies. The theory of dual energy post-processing method is given in the following section.

5.2.1.1 Theoretical Considerations for Dual Energy CT

The linear attenuation coefficient $\mu(E)$ of trabecular bone at energies E_1 and E_2 is given by equation (5.1.10) in section 5.1:

$$\mu(E_1) = \mu_w(E_1) [F_b(E_1)C_b + F_{nm}(E_1)C_{nm}] \quad (5.2.1)$$

$$\mu(E_2) = \mu_w(E_2) [F_b(E_2)C_b + F_{nm}(E_2)C_{nm}] \quad (5.2.2)$$

where C_b , C_{nm} are the concentrations, and F_b , F_{nm} are the mass attenuation coefficients relative to water, of the mineral and non-mineral components of trabecular bone respectively. $\mu(E)$ is the linear attenuation coefficient of trabecular bone at an energy E .

The linear attenuation coefficients $\mu_k(E_1)$ and $\mu_k(E_2)$ of a K_2HPO_4 solution of concentration C_k at the two energies can be written as:

$$\mu_k(E_1) = \mu_w(E_1) [F_b(E_1)C_k + C_w] \quad (5.2.3)$$

$$\mu_k(E_2) = \mu_w(E_2) [F_b(E_2)C_k + C_w] \quad (5.2.4)$$

where C_w is the concentration of water in the given K_2HPO_4 solution. The subscripts E_1

and E2 in equations (5.2.1) to (5.2.4) correspond to the lower and higher X-ray beam energies. From equations (5.2.1) to (5.2.4), the bone mineral concentration of trabecular bone C_b in terms of concentration of K_2HPO_4 solution C_k can be calculated as follows:

$$C_b = C_k \frac{\frac{\mu(E1)}{\mu_w(E1)} - \frac{\mu(E2)}{\mu_w(E2)}}{\frac{\mu_k(E1)}{\mu_w(E1)} - \frac{\mu_k(E2)}{\mu_w(E2)}} \quad (5.2.5)$$

with the following assumptions:

- (1) The concentration of water in mineral solution is equal to its density i.e. $C_w=1.0$
- (2) The ratio of the mass attenuation coefficient of the non-mineral component to that of water is the same at two energies i.e. $F_{nm}(E1)=F_{nm}(E2)$

The second assumption is not strictly valid since the ratio of the mass attenuation coefficient of fat to that of water increases with increasing photon energy, and there is a small decrease in this ratio for soft tissue with increasing photon energy [Rao et al., 1987]. Due to the variations in the composition of trabecular bone, therefore, an error will always result in its measured bone mineral content (section 6.1.1)

The concentration of the non-mineral content of trabecular bone can be similarly computed from the above equations. A dual energy post-processing method is available for determining the fat and soft tissue content of trabecular bone [Goodsitt and Rosenthal, 1987]. The bone mineral is expressed in terms of the standard K_2HPO_4 solutions, while a percentage of ethyl alcohol in water is used as a standard for the fat content present in the non-mineral part of trabecular bone. The calibration of the pixel value vs. the percentage of ethyl alcohol in water is carried out at specified photon beam energies, in addition to the usual calibration of the pixel value vs. concentration of K_2HPO_4 . These calibration data, and the pixel values of the trabecular bone at two energies, are used to compute the bone mineral and fat contents without making any assumptions regarding the composition of trabecular bone. The precision error in these measurements is large, however, since the

standard error for each calibration measurement propagates into the calculated mineral and fat contents. For this reason this post-processing method was not implemented for the X-CT scanner.

5.2.1.2 Procedure of Bone Mass Measurement

The established measurement position at a particular skeletal site is scanned at the two selected energies along with a K_2HPO_4 solution of a known concentration. The selection of the two beam energies for the X-CT scanner is dictated by the necessity to operate the detectors in their linear region; 50kV, 2.8mA and 80kV, 1.75mA were chosen as the two X-ray beam energies with 0.65mm and 2.75mm thick copper filters respectively.

The contour of the cortical bone is determined for the CT images of a bone cross-section at two energies by the method discussed in section 4.2.2. The mean pixel values within a given region of trabecular bone are found for both images; these values are proportional to the linear attenuation coefficients of trabecular bone at the two energies. The pixel values of pure water and mineral solution are also determined from images of calibration phantoms. The bone mineral content is then computed from equation (5.2.5). The resulting volumetric bone density is then computed for a specified volume by integrating the TBD vs. area function with respect to the position of the measurement.

5.2.2 Pre-processing Method

The linear attenuation coefficient of a material depends on its electron density and atomic number as well as on the photon energy used. Within the diagnostic range of photon energies (40 keV-100 keV) photons interact with a material principally through photoelectric absorption and Compton scattering processes. Hence the linear attenuation coefficient of a material can be defined in terms of the material, and the energy dependent parts of photoelectric absorption and Compton scattering. Therefore, the material

dependence for the photoelectric absorption and Compton scattering processes can be established if the linear attenuation coefficients of a material are known at two photon energies.

The pre-processing method generates two images, one containing an aluminum equivalent and the other a plexiglass equivalent of the material present in the desired cross-section. In case of trabecular bone, an aluminum equivalent image contains the mineral component plus a negligible amount of a non-mineral component, and vice versa, a plexiglass equivalent image contains non-mineral component and a negligible amount of mineral component. The mineral content of trabecular bone can therefore be quantified from the aluminum equivalent images with only a small error due to variable amounts of fat.

In the following sections, a detailed description of the theory and procedures for the pre-processing method is given.

5.2.2.1 Theoretical Considerations for the Pre-processing Approach to DECT

In the diagnostic energy range X-ray photons are attenuated principally by photoelectric absorption and Compton scattering. The mass attenuation coefficient of a material at an energy E can be expressed in terms of the material and the photon energy dependent components as follows:

$$\frac{\mu(E)}{\rho} = a_c f_c(E) + a_p f_p(E) \quad (5.2.6)$$

where $\mu(E)$ and ρ are the linear attenuation coefficient and density of material respectively, and $f_c(E)$ and $f_p(E)$ are the energy dependent components corresponding to Compton scattering and photoelectric absorption. The material dependent component a_c is the electron mass density N_g (electrons/gm):

$$a_c = N_g = \frac{Z}{A} \times \text{Avogadro's Number} \quad (5.2.7)$$

where Z and A are the atomic number and atomic weight of the material respectively. The

energy dependent component f_c is the Klein-Nishina function [John and Cunningham, 1983]. The second part of equation (5.2.6) can be written as [Lehmann et al., 1981]:

$$a_p f_p(E) = N_g C_p \frac{Z^{3.8}}{E^3} = N_g Z^{3.8} f_p(E)$$

where $C_p = 9.8 \times 10^{-24}$ and E is in keV.

Hence the material dependent component of the photoelectric absorption is proportional to approximately the fourth power of the atomic number of the material, while the energy dependent component is inversely proportional to the third power of the energy. Equation (5.2.6) is the result of a least squares fit to experimental data [Alvarez and Macovski, 1976]. However, it should be noted that equation (5.2.6) is true only in the energy range above the K-edge discontinuities, where photons are attenuated predominantly through the Compton scattering and photoelectric absorption.

It follows then that every material can be characterised by its a_c and a_p components. Therefore, by measuring the linear attenuation coefficient at two energies the material dependent components of photoelectric (a_p) and Compton (a_c) processes can be determined. In the case of X-CT the line integrals (projection ray-sums) measured at two energies can be separated into line integrals of a_c and a_p along a given beam path. The resulting images, the basis images, contain the values of a_c and a_p within a cross-section. This choice of basis images is useful in determining the chemical composition of the underlying material [Alvarez and Macovski, 1976].

The linear attenuation coefficient of any material can be expressed as a linear combination of the linear attenuation coefficients of aluminum and plexiglass. Rewriting equation (5.2.6) for aluminum and plexiglass:

$$\frac{\mu_{AL}(E)}{\rho_{AL}} = N_{gAL} f_c(E) + N_{gAL} Z_{AL}^{3.8} f_p(E) \quad (5.2.8)$$

$$\frac{\mu_{PL}(E)}{\rho_{PL}} = N_{gPL} f_c(E) + N_{gPL} Z_{PL}^{3.8} f_p(E) \quad (5.2.9)$$

Solving equations (5.2.8) and (5.2.9) for f_c and f_p and putting the result into equation (5.2.6), we get the following result [Lehmann et al., 1981]:

$$\frac{\mu(E)}{\rho} = a_1 \frac{\mu_{PL}(E)}{\rho_{PL}} + a_2 \frac{\mu_{AL}(E)}{\rho_{AL}} \quad (5.2.10)$$

where a_1 and a_2 are plexiglass and aluminum equivalent coefficients of a material given by:

$$a_1 = \frac{N_g(Z_{PL}^{3.8} - Z_{AL}^{3.8})}{N_{gPL}(Z_{PL}^{3.8} - Z_{AL}^{3.8})}; \quad a_2 = \frac{N_g(Z_{AL}^{3.8} - Z_{PL}^{3.8})}{N_{gAL}(Z_{AL}^{3.8} - Z_{PL}^{3.8})} \quad (5.2.11)$$

Table 5.2.1: Accuracy of basis decomposition

Material	a_1	a_2	% RMS Error
Aluminum	0.000	1.000	0.000
Plexiglass	1.000	0.000	0.000
Muscle	0.950	0.080	0.039
Bone	0.237	0.833	0.259
Water	0.968	0.071	0.053
Fat	1.067	-0.037	0.016

Table (5.2.1) gives the coefficients a_1 and a_2 of equation (5.2.11) for a number of materials within the energy range 40-110 keV. The coefficients listed are the result of a least squares fit of equation (5.2.10) to the measured attenuation coefficients [Lehmann et al., 1981].

Equation (5.2.10) can be used to determine the aluminum (bone) and plexiglass (soft tissue) equivalent parts of trabecular bone.

5.2.2.2 Procedure

Let $\mu(x,y,E)$ be the linear attenuation coefficient within the desired cross-section of

a material as a function of energy. In CT the logarithmic transmission of a well collimated X-ray beam through a volume of object is measured. If I and I_0 are the transmitted and the incident beam intensities respectively, the logarithmic transmission is given by:

$$T = -\ln \left(\frac{I}{I_0} \right) = -\ln \left[\int S(E) \exp \left\{ -\int \mu(x,y,E) dS \right\} dE \right] \quad (5.2.12)$$

where dS is the small length across the beam path and $S(E)$ is the X-ray energy spectrum distribution.

Using equation (5.2.11) equation (5.2.12) can be rewritten as:

$$T = -\ln \left[\int S(E) \exp \left\{ -[A_{PL}\mu_{PL}(E) + A_{AL}\mu_{AL}(E)] \right\} dE \right] \quad (5.2.13)$$

where;

$$A_{PL} = \frac{1}{\rho_{PL}} \int \rho(x,y) a_1(x,y) dS \quad ; \quad A_{AL} = \frac{1}{\rho_{AL}} \int \rho(x,y) a_2(x,y) dS$$

The parameters A_{AL} and A_{PL} are the equivalent aluminum and plexiglass thicknesses along the beam path for a given material. The units of the coefficients A_{AL} and A_{PL} are those of length. Equation (5.2.13) can be solved for A_{AL} and A_{PL} if the logarithmic transmission values are known for two beam energies. Let $S_L(E)$ and $S_H(E)$ be the energy spectra at X-ray tube potentials of 50kV and 80kV respectively. The lower and higher energy logarithmic transmission values, T_L and T_H can be written as:

$$T_L = -\ln \left[\int S_L(E) \exp \left\{ -[A_{AL}\mu_{AL}(E) + A_{PL}\mu_{PL}(E)] \right\} dE \right] \quad (5.2.14)$$

$$T_H = -\ln \left[\int S_H(E) \exp \left\{ -[A_{AL}\mu_{AL}(E) + A_{PL}\mu_{PL}(E)] \right\} dE \right] \quad (5.2.15)$$

If the source is monoenergetic then these equations can be simplified to first order simultaneous equations:

$$T_L = A_{AL}\mu_{AL}(E) + A_{PL}\mu_{PL}(E) \quad (5.2.16)$$

$$T_H = A_{AL}\mu_{AL}(E) + A_{PL}\mu_{PL}(E) \quad (5.2.17)$$

The aluminum equivalent thickness A_{AL} and the plexiglass equivalent thickness A_{PL} can be obtained from equations (5.2.16) and (5.2.17). However, the X-ray source for the X-CT scanner is polyenergetic, thus higher order terms must be included in these equations to account for spectral hardening. Conventionally [Alvarez and Macovski, 1976] a second order polynomial can be used as an approximation to equations (5.2.14) and (5.2.15) i.e.:

$$T_L = a_0 + a_1 A_{AL} + a_2 A_{PL} + a_3 A_{PL} A_{AL} + a_4 A_{PL}^2 + a_5 A_{AL}^2 \quad (5.2.18)$$

$$T_H = b_0 + b_1 A_{AL} + b_2 A_{PL} + b_3 A_{PL} A_{AL} + b_4 A_{PL}^2 + b_5 A_{AL}^2 \quad (5.2.19)$$

where the coefficients a_i and b_i ($i=1,5$) are determined by a calibration procedure discussed in the following sections.

There are a number of approaches to solve for equivalent aluminum and plexiglass thicknesses using either equations (5.2.18) and (5.2.19) or equations (5.2.14) and (5.2.15). The choice of procedure is based upon the following considerations:

- (1) Accuracy.
- (2) Sensitivity to noise in the data.
- (3) Sensitivity to the numerical procedure.
- (4) Computation time.

5.2.2.2(a) Conventional Approach

This approach was used by Alvarez and Macovski [Alvarez and Macovski, 1976] to generate the Compton and photoelectric basis images. This method can be briefly summarised by the following steps:

- (1) A number of combinations of aluminum and plexiglass thickness are scanned at

two beam energies giving the lower and higher energy logarithmic attenuation values for different combinations of A_{AL} and A_{PL} .

(2) Using the method of least squares equations (5.2.18) and (5.2.19) are fitted to the lower and higher energy logarithmic attenuation data to find the coefficients a_i and b_i .

(3) The object of interest is scanned at two energies and the logarithmic attenuations are determined for all possible beam orientations by CT.

(4) The equivalent aluminum and plexiglass thicknesses are determined from equations (5.2.18) and (5.2.19) using a generalized Newton-Raphson method [MacCracken and Dorn, 1964]. An aluminum image is reconstructed from the A_{AL} values and a plexiglass image is reconstructed from the A_{PL} values.

The Alvarez-Macovski method was not implemented for the X-CT scanner because:

- (a) the accuracy of the results depends upon the numerical procedure in the least squares fit,
- (b) the Newton-Raphson method sometimes does not converge due to noise, and (c) the computation time to reconstruct a 512x512 image is high (about 20 minutes) [Chuang and Huang, 1987].

5.2.2.2(b) Isotransmission Line Approach

Suppose t_{AL} and t_{PL} represent the thicknesses of aluminum and plexiglass respectively. For a given beam energy E there exist a number of combinations of aluminum and plexiglass thicknesses which would give the same logarithmic attenuation T_E . For a monoenergetic beam these ordered pairs of aluminum and plexiglass (t_{AL} , t_{PL}) are linearly related and the resulting straight line is known as an isotransmission line. The equation of an isotransmission line is given as:

$$T_E = \mu_{AL}(E) t_{AL} + \mu_{PL}(E) t_{PL} \quad (5.2.20)$$

An isotransmission line for a monoenergetic beam is shown in Figure 5.2.1. It should be noted that isotransmission lines for monoenergetic beams are parallel to each other.

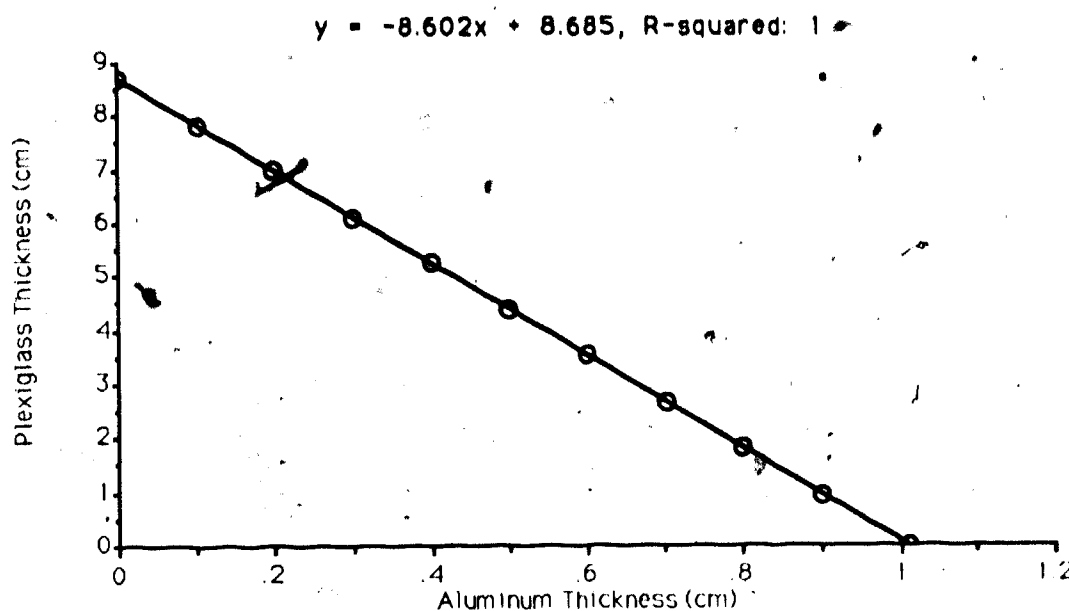


Figure 5.2.1: Isotransmission line at 30 keV for constant $T_{30 \text{ keV}} = 3.0$

If the X-ray beam is polyenergetic then the ordered pairs of aluminum and plexiglass are not linearly related since the linear attenuation coefficient is a nonlinear function of the photon energy. The ratio of the linear attenuation coefficients for aluminum and plexiglass varies nonlinearly with energy so the thickness of plexiglass and aluminum required to give the same attenuation are not linearly related. Wong et al. [Wong and Huang, 1983] were able to fit a fourth order polynomial to aluminum vs. plexiglass thicknesses required to give the same attenuation.

Suppose N aluminum plates of equal thickness are required for a given attenuation of a polyenergetic beam. If one aluminum plate is removed, a fixed thickness of plexiglass will then be required to obtain the same attenuation of the beam. The thickness of the

plexiglass would depend on the ratio of the effective attenuation coefficients of aluminum and plexiglass. If two aluminum plates are removed, the required thickness of plexiglass to obtain the same attenuation would not be doubled, since a nonlinear change in the spectrum of the beam results, and the ratio of the effective attenuation coefficients for the two materials is not the same. Therefore, isotransmission lines cannot be defined for polyenergetic beams due to changes in energy spectrum as the beam passes through different thicknesses of aluminum and plexiglass.

The isotransmission line approach can be used for a polyenergetic beam if spectral hardening errors are not significant. The logarithmic attenuation was shown as a function of thickness of an aluminum and plexiglass sandwich in Figure 3.2.5. The logarithmic attenuation is almost a linear function of thickness of material and deviation from linearity begins only at larger values of attenuation. Therefore, for the linear range of the curve shown in Figure 3.2.5, the isotransmission curves can be assumed as straight lines.

The isotransmission line method has been used successfully by Chuang et al. [Chuang and Huang, 1987] to carry out bone and soft tissue decomposition with a polyenergetic beam. The computational time required for separating the projection ray-sums at two energies into equivalent aluminum and plexiglass thickness is (< 2minutes) less than that required for the Alvarez-Macovski reconstruction method.

5.2.2.2(b.1) Isotransmission Line Calibrations

The data collection process for the isotransmission calibration is the same as that used for the conventional method. The basis materials for bone and soft tissue decomposition are chosen as aluminum and plexiglass.

The first step in the calibration process is to determine the thickness of

Table 5.2.2: Calibration Table for logarithmic attenuations at 50kV, 2.8mA. The number across the top and down are number of steps. The step sizes of aluminum and plexiglas are 0.085 and .585mm respectively.

AL PL	0	1	2	3	4	5	6	7	8	9	10	11	12	13
0	-.001	0.120	0.247	0.364	0.508	0.628	0.740	0.857	1.000	1.117	1.260	1.386	1.498	1.638
1	0.149	0.269	0.396	0.519	0.663	0.783	0.892	1.012	1.154	1.275	1.417	1.539	1.651	1.790
2	0.300	0.423	0.550	0.675	0.820	0.935	1.048	1.168	1.311	1.427	1.568	1.693	1.802	1.947
3	0.451	0.574	0.705	0.828	0.969	1.087	1.204	1.320	1.461	1.579	1.719	1.840	1.950	2.093
4	0.613	0.736	0.867	0.989	1.131	1.255	1.363	1.480	1.623	1.743	1.878	2.002	2.113	2.256
5	0.768	0.892	1.019	1.144	1.288	1.407	1.518	1.636	1.774	1.891	2.032	2.153	2.266	2.403
6	0.930	1.054	1.179	1.305	1.449	1.563	1.680	1.792	1.935	2.048	2.190	2.311	2.419	2.555
7	1.093	1.216	1.345	1.467	1.611	1.727	1.838	1.952	2.089	2.205	2.348	2.467	2.576	2.716
8	1.253	1.376	1.504	1.625	1.769	1.889	1.993	2.105	2.248	2.361	2.504	2.622	2.734	2.884
9	1.412	1.531	1.661	1.780	1.921	2.036	2.149	2.262	2.406	2.516	2.651	2.780	2.899	3.035
10	1.581	1.700	1.829	1.947	2.086	2.202	2.317	2.429	2.569	2.679	2.823	2.951	3.059	3.195
11	1.733	1.861	1.986	2.101	2.240	2.356	2.470	2.581	2.722	2.837	2.980	3.101	3.212	3.351
12	1.894	2.010	2.137	2.258	2.398	2.508	2.616	2.730	2.876	2.999	3.136	3.255	3.361	3.507
13	2.046	2.163	2.293	2.410	2.549	2.667	2.776	2.891	3.036	3.145	3.287	3.409	3.521	3.655
14	2.205	2.328	2.450	2.568	2.704	2.826	2.944	3.056	3.188	3.303	3.439	3.557	3.673	3.805
15	2.362	2.476	2.605	2.726	2.863	2.986	3.094	3.202	3.350	3.460	3.594	3.712	3.822	3.958
16	2.517	2.631	2.760	2.878	3.026	3.132	3.251	3.361	3.493	3.613	3.748	3.864	3.973	4.113
17	2.672	2.786	2.920	3.041	3.185	3.298	3.403	3.519	3.657	3.768	3.902	4.023	4.136	4.259
18	2.835	2.953	3.084	3.198	3.331	3.441	3.556	3.661	3.805	3.904	4.072	4.169	4.283	4.418
19	3.006	3.114	3.246	3.358	3.496	3.605	3.710	3.830	3.972	4.083	4.222	4.337	4.450	4.585
20	3.163	3.284	3.411	3.528	3.660	3.767	3.882	3.993	4.125	4.244	4.375	4.503	4.596	4.745

aluminum and plexiglass corresponding to the maximum thickness of bone and soft tissue, respectively. A 1.105cm thickness of aluminum, and a 11.78cm thickness of plexiglass were found to be adequate for the distal femur site. The thickness of each individual aluminum plate is 0.085cm, and of each plexiglass plate 0.589cm, resulting in a total of 13 aluminum and 20 plexiglass plates. Combinations of aluminum and plexiglass plates are scanned at 50kV, 2.8mA and 80kV, 1.75mA on the X-CT scanner. Copper beam filters of thickness 0.65mm and 2.75mm are used at 50kV and 80kV respectively. The resulting logarithmic attenuations are shown in Table 5.2.2 and Table 5.2.3 corresponding to a single detector at two X-ray beam qualities.

For a given detector the calibration data for different combinations of aluminum and plexiglass plates can be represented by a matrix. The rows of this matrix represent the

thickness of plexiglass and the columns represent the thickness of aluminum.

Table 5.2.3: Calibration Table for logarithmic attenuations at 80kV, 1.75mA. The number across the top and down are number of steps. The step sizes of aluminum and plexiglass are 0.085 and .585mm respectively.

PL \ AL	0	1	2	3	4	5	6	7	8	9	10	11	12	13
0	-0.002	0.057	0.111	0.170	0.236	0.291	0.342	0.399	0.465	0.523	0.588	0.647	0.697	0.769
1	0.124	0.186	0.241	0.298	0.361	0.418	0.469	0.530	0.592	0.654	0.715	0.778	0.822	0.899
2	0.252	0.312	0.366	0.427	0.490	0.545	0.597	0.655	0.720	0.778	0.846	0.902	0.950	1.021
3	0.375	0.435	0.491	0.550	0.613	0.670	0.722	0.778	0.845	0.901	0.967	1.029	1.073	1.148
4	0.511	0.569	0.623	0.682	0.747	0.805	0.853	0.911	0.980	1.039	1.100	1.159	1.210	1.280
5	0.638	0.698	0.752	0.807	0.871	0.932	0.980	1.038	1.104	1.161	1.230	1.289	1.330	1.404
6	0.768	0.830	0.883	0.938	1.003	1.064	1.111	1.167	1.234	1.294	1.358	1.416	1.465	1.538
7	0.902	0.960	1.014	1.074	1.139	1.192	1.240	1.305	1.367	1.426	1.491	1.546	1.596	1.665
8	1.030	1.086	1.145	1.201	1.267	1.320	1.370	1.432	1.495	1.555	1.610	1.679	1.728	1.792
9	1.163	1.216	1.273	1.329	1.395	1.452	1.500	1.560	1.624	1.683	1.742	1.807	1.855	1.922
10	1.294	1.355	1.411	1.466	1.527	1.588	1.636	1.697	1.753	1.818	1.883	1.936	1.996	2.059
11	1.422	1.481	1.537	1.589	1.658	1.712	1.763	1.821	1.892	1.942	2.006	2.066	2.118	2.181
12	1.550	1.610	1.663	1.715	1.782	1.837	1.885	1.947	2.016	2.065	2.133	2.186	2.241	2.314
13	1.676	1.730	1.786	1.841	1.907	1.964	2.015	2.069	2.141	2.197	2.261	2.317	2.368	2.440
14	1.812	1.862	1.920	1.969	2.037	2.094	2.144	2.190	2.266	2.327	2.394	2.448	2.496	2.565
15	1.935	1.992	2.047	2.100	2.164	2.218	2.271	2.334	2.396	2.451	2.514	2.575	2.623	2.691
16	2.059	2.119	2.170	2.227	2.294	2.352	2.396	2.456	2.518	2.575	2.645	2.699	2.743	2.823
17	2.188	2.244	2.295	2.356	2.430	2.474	2.530	2.585	2.641	2.706	2.769	2.825	2.875	2.949
18	2.310	2.376	2.426	2.491	2.549	2.606	2.654	2.708	2.781	2.831	2.901	2.959	2.999	3.074
19	2.449	2.505	2.569	2.616	2.684	2.739	2.791	2.845	2.908	2.960	3.037	3.091	3.135	3.202
20	2.588	2.641	2.708	2.758	2.822	2.871	2.926	2.990	3.047	3.109	3.175	3.222	3.266	3.347

The maximum and minimum logarithmic transmissions are determined from the matrix and the range between the maximum and minimum transmissions arbitrarily divided into 290 transmission values. The logarithmic transmission for the first isotransmission line is set to the minimum value. The combinations of aluminum and plexiglass thicknesses for this transmission value T_L are determined. An isotransmission line is fitted to aluminum vs plexiglass thickness if the number of such combinations is more than three. The general form of the isotransmission line is given by:

$$T_L = a_L t_{AL} + b_L t_{PL} \quad (5.2.21)$$

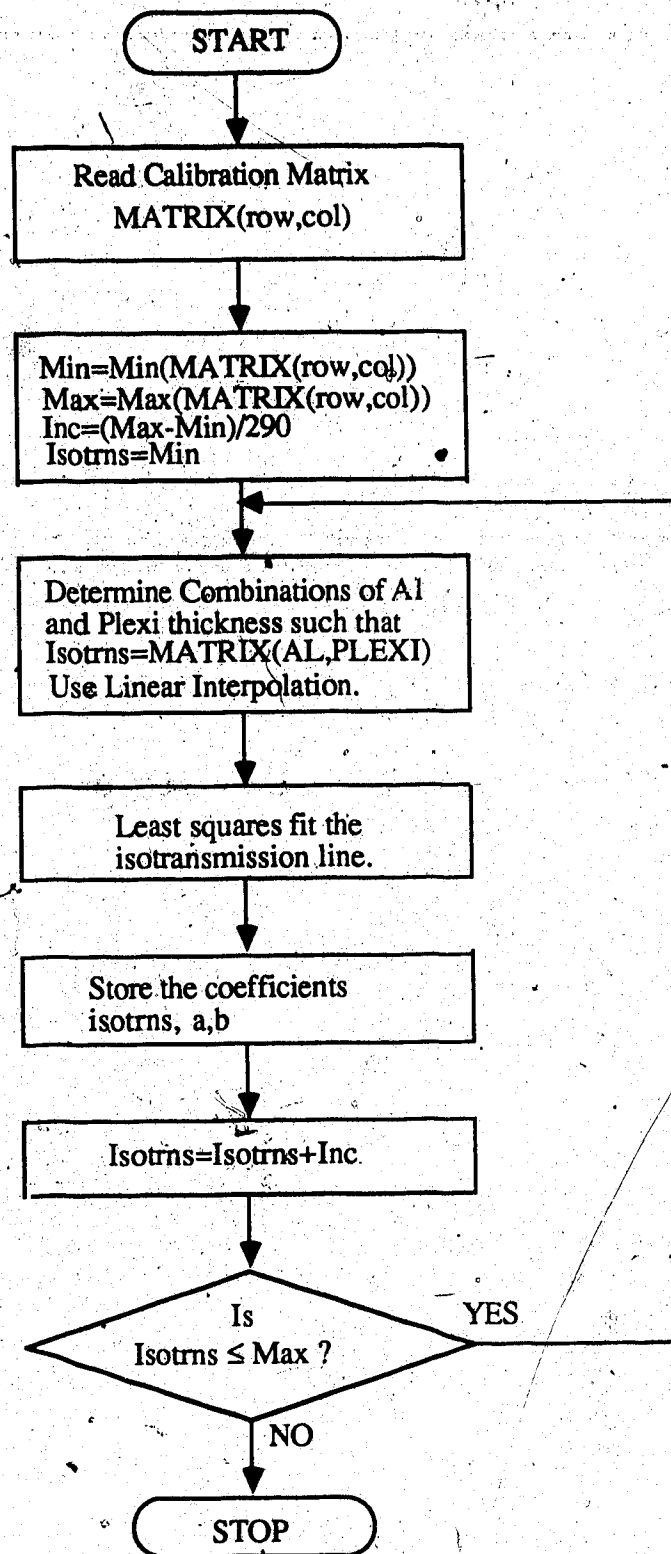


Figure 5.2.2: Flowgraph for isotransmission line calibrations.

where a_L and b_L are the regression coefficients, and the subscript L specifies the lower energy. The procedure is repeated for all 290 logarithmic transmission values and the coefficients stored in a lookup table. A flow diagram for this procedure is shown in Figure 5.2.2 for a given detector at a given beam energy. The procedure is repeated for all 26 detectors at both energies. At the higher energy the equation of the isotransmission line can be written as:

$$T_H = a_H t_{AL} + b_H t_{PL} \quad (5.2.22)$$

where T_H is the constant attenuation at higher energy and a_H and b_H are the regression coefficients resulting from the least squares fit. It should be noted that the coefficients a_L and b_L are proportional to the attenuation of the lower energy beam by aluminum and plexiglass respectively. Similarly, the coefficients a_H and b_H are proportional to the attenuation of the higher energy beam by aluminum and plexiglass respectively.

The validity of the isotransmission lines can be verified experimentally. At a given energy the logarithmic attenuation for a given combination of aluminum and plexiglass is found in the lookup tables of isotransmission line at that energy. The coefficients of the isotransmission line are used to calculate the attenuation for the combination of aluminum and plexiglass. The error between the predicted attenuation and the observed attenuation is calculated for all combinations of aluminum and plexiglass at both the energies. The maximum error between observed and predicted attenuations with respect to the observed attenuation was found to be less than 2% for both energies. This error is slightly more than the error found by Chuang et al. [Chuang and Huang, 1987] since 50kV and 80kV are used instead of 80kV and 120kV, and the contribution of coherent scattering to the attenuation coefficient is greater at lower photon energies. The root-mean-square error was

found to be 0.67% and 0.55% at 50kV and 80kV respectively.

Two isotransmission lines are shown in Figure 5.2.3 for a single detector at 50kV and 2.8mA. It should be noted that the slope of the isotransmission lines from one transmission value to another is different due to spectral hardening.

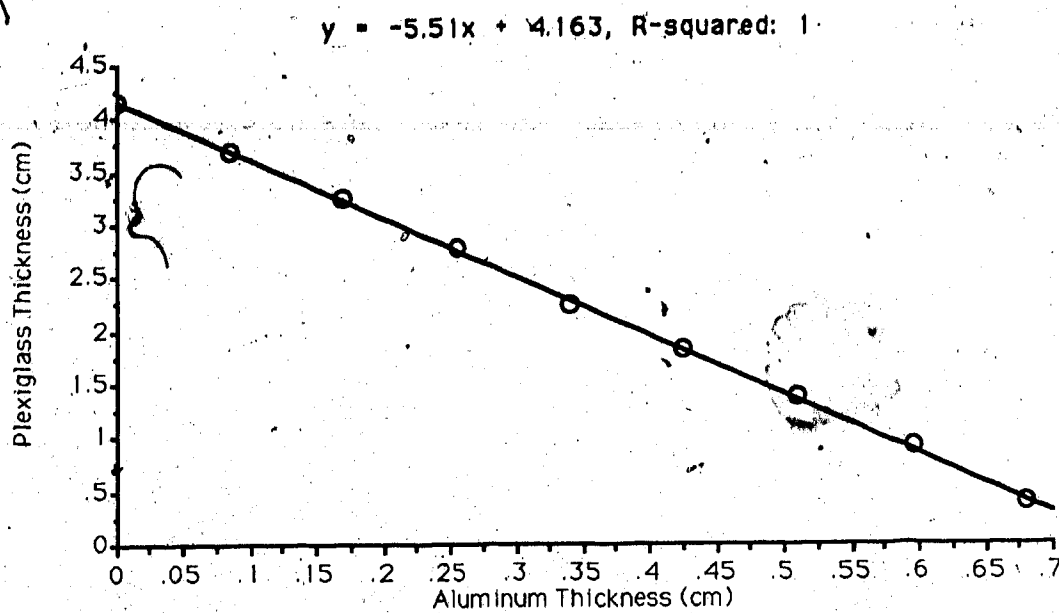
5.2.2.3 Bone and Soft Tissue Decomposition

The isotransmission line calibration step is a tedious and time consuming process in the pre-processing method. However, the reconstruction process for bone and soft tissue images is simple.

The object of interest is scanned at the two beam energies. In some commercial scanners, the provision for switching the X-ray tube potential between data pulses has made this procedure easy and efficient. The high voltage power supply of the X-ray tube in our CT scanner can be switched remotely but the tube itself can not be used in pulsed mode. Moreover, in order to avoid count rate saturation problems with detectors a larger thickness of copper filter is required at 80kV than at 50kV, therefore two separate scans of the object are taken at 50kV and 80kV respectively.

The projection ray-sums at the two energies are used to determine the coefficients a_L , a_H , b_L and b_H from the lookup tables. Equations (5.2.22) and (5.2.23) are then solved for the resulting combination (t_{AL} , t_{PL}) of aluminum and plexiglass equivalent thicknesses. These thicknesses are the same as parameters A_{AL} and A_{PL} in equations (5.2.14) and (5.2.15), hence the resulting data (t_{AL} , t_{PL}) are used to reconstruct the aluminum and plexiglass equivalents of the cross-section of the object.

The bone and soft tissue images of a distal femur section are shown in Figure 5.2.4 along with the single energy images at two beam energies. The aluminum equivalent (bone) image contains the entire amount of bone and a little soft tissue. Similarly, bone tissue is not seen in the plexiglass (soft tissue) equivalent image.



a) Isotransmission line at 50 kV for constant $T_{50kV} = 1.10$

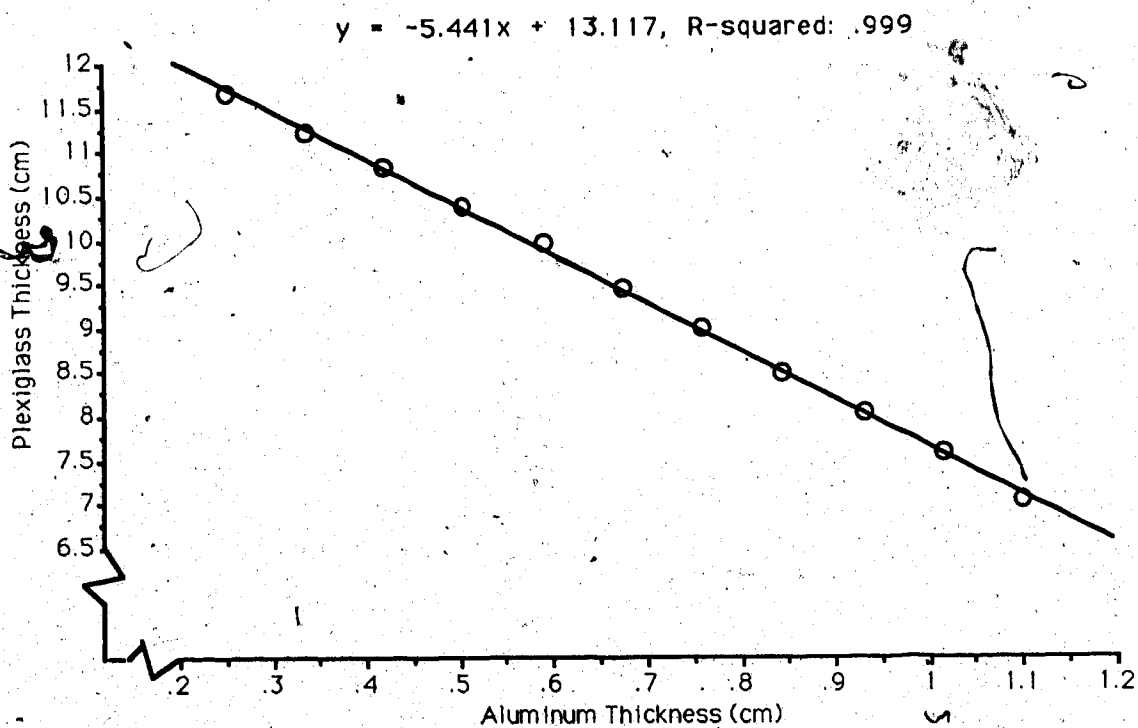


Figure 5.2.3

b) Isotransmission line at 50 kV for constant $T_{50kV} = 3.50$



Figure 5.2.4(a)
50 kV CT image of a cadaver femur at distal site.



Figure 5.2.4(b)
80 kV CT image of a cadaver femur at distal site.

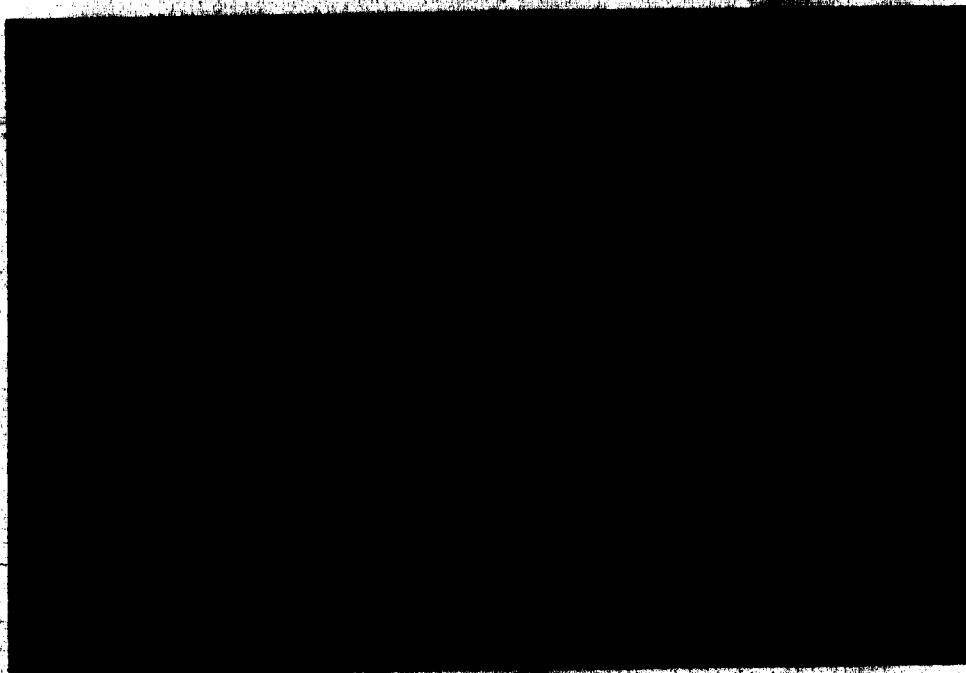


Figure 5.2.4 (c)
Bone equivalent CT image resulting from basis decomposition of (a) and (b).

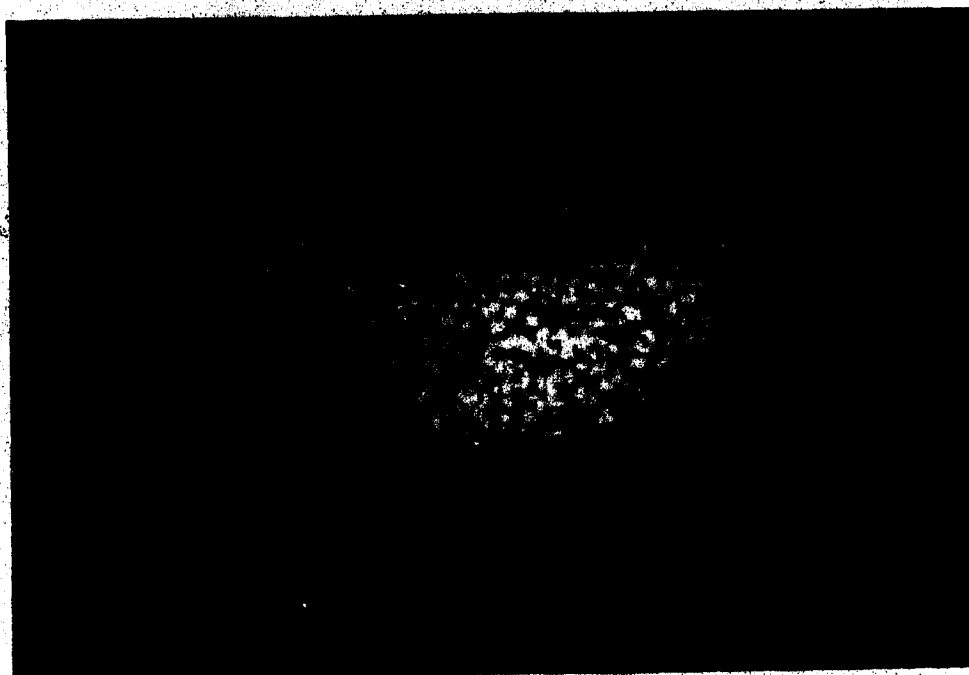


Figure 5.2.4(d)
Soft tissue equivalent CT image resulting from basis decomposition of (a) and (b).

5.2.2.4 TBD Measurement

The soft tissue and fat present in trabecular bone contribute little towards the pixel values of trabecular bone in an aluminum equivalent image. The aluminum image is therefore analysed to quantify the bone mineral contents in terms of gms/ml of K_2HPO_4 solution. Let a_{2m} , a_{2s} and a_{2f} be the aluminum equivalent coefficients, and C_m , C_s , and C_f be concentrations (gm/ml) of bone mineral, soft tissue and fat present in the trabecular bone, respectively. The pixel value of trabecular bone in the aluminum image $P_{AL}(\text{bone})$ is given by:

$$P_{AL}(\text{bone}) = \frac{1}{\rho_{AL}} (a_{2m} C_m + a_{2s} C_s + a_{2f} C_f) \quad (5.2.23)$$

Similarly the pixel value of a bone-like mineral solution $P_{AL}(K)$ is given by:

$$P_{AL}(K) = \frac{1}{\rho_{AL}} (a_{2m} C_k + a_{2w} C_w) \quad (5.2.24)$$

The bone mineral content can be expressed in terms of concentration of mineral solution from equations (5.2.23) and (5.2.24):

$$C_m = C_k \frac{P_{AL}(\text{bone}) - P_{AL}(W)}{P_{AL}(K) - P_{AL}(W)} \quad (5.2.25)$$

where $P_{AL}(W)$ is the pixel value of water in the aluminum image given by:

$$P_{AL}(W) = \frac{a_{2w} C_w}{\rho_{AL}}$$

The following assumptions are made in solving equations (5.2.23) and (5.2.24):

- (1) The aluminum equivalent coefficients of bone mineral and mineral solution are equal.
- (2) The non-mineral component of the trabecular bone gives a pixel value equal to that of water in the aluminum image.

Similar assumptions were made in the concentration method in case of SECT (section 5.1.2).

In practice equation (5.2.25) is not used directly to quantify the bone mineral content. An approach similar to the SECT method is taken and a calibration line for various K_2HPO_4 solutions is determined. The slope and the intercept of this line are calculated and then used to determine the bone mineral concentration. The calibration line corresponding to the aluminum images of the K_2HPO_4 solutions is shown in Figure 5.2.5. The standard errors of estimate of the slope and intercept are 1.15% and 2.98% respectively.

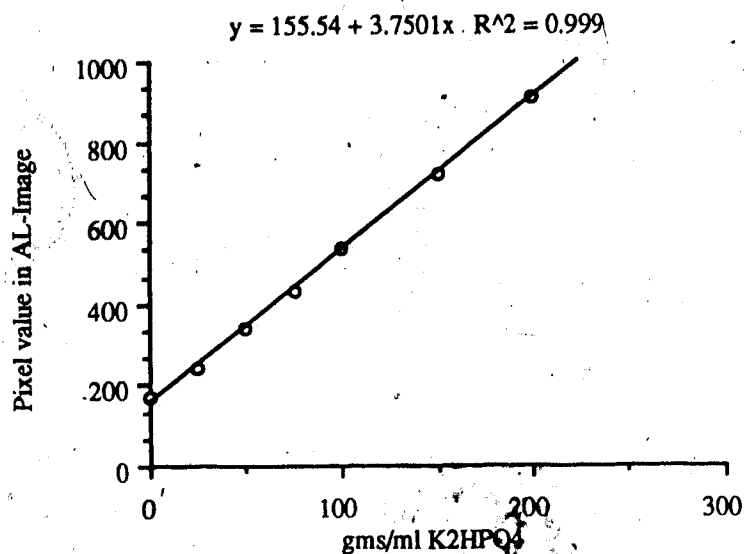


Figure 5.2.5

Pixel value in the aluminum equivalent image vs. concentration of the mineral solution. The regression line equation and the correlation coefficient are shown.

6.0 Performance of X-CT Scanner for TBD Measurement

The performance of the X-CT scanner for TBD measurements is evaluated in terms of measurement accuracy and precision. The accuracy of the TBD measurement is particularly important in cross-sectional population studies. The precision of the TBD measurement is important in longitudinal studies to quantify small changes in TBD over time.

In this chapter the factors affecting the accuracy and precision of TBD measurements using the X-CT scanner are analyzed. The results for human cadaver femur measurements, *in vitro*, and for human *in vivo* measurements at distal femur and proximal tibia sites are presented.

6.1 Accuracy

The accuracy of a bone mineral measurement is usually stated relative to the actual amount of bone mineral (gm/cm^3) contained in the volume measured by CT. The normal standard of reference is the gravimetric determination of mineral content in a sample following ashing [Cann, 1988].

In general, the factors affecting the accuracy of TBD measurement can be classified into two categories: physiological and experimental. The physiological factors include changes in the composition of the measured bone volume, for example relative changes in the fractional fat content. The experimental factors are associated with the accuracy of CT measurement of linear attenuation coefficients in a bone cross-section. For this X-CT scanner the evaluation of the effects of these factors on the measured TBD will be elaborated upon in the following section. The significance of several factors which affect the accuracy of TBD measurement will be analysed in terms of standard mineral solutions. These are:

- (1) Variable fractional fat content

(2) Beam hardening

(3) Scattering and Exponential Edge Gradient Effect

6.1.1 Variable Fractional Fat Content.

As noted in earlier sections, trabecular bone is composed of three principal components: bone mineral, soft tissue (red marrow), fat (yellow marrow). Assuming that each pixel in a CT image represents the average linear attenuation coefficient for a fixed measurement volume, the SECT measurement is able to measure the volume fraction of the two components if their material properties are known. The previously discussed assumptions regarding one or two components are generally made in the SECT measurements. The assumption regarding the radiological equivalence of water to the non-mineral component of trabecular bone is made in the 'concentration method' of SECT. However, the linear attenuation coefficient of soft tissue is slightly greater than that of water while the linear attenuation coefficient of fat is less than that of water. A similar behaviour for density is also found for these components. The fractional fat content of trabecular bone is variable from person to person; it also varies over time at any particular skeletal site for an individual. This unknown quantity of fat causes a systematic uncertainty in the TBD values measured by SECT [Mazess, 1983; Laval-Jeantet et al., 1986]. The fat fraction of the total linear attenuation coefficient for trabecular bone increases with increasing photon energy thus giving a larger error in measured TBD values at higher energies.

The major part of the photon attenuation is due to photoelectric absorption at lower photon energies (30keV-40keV) and is approximately proportional to the fourth power of the atomic number. Therefore, a very high contrast between bone and the non-mineral component is obtained at lower energies, and the errors due to variable amounts of fat in the TBD measurements are greatly reduced. The special-purpose CT scanners designed for peripheral bone evaluation [Rüeggsegger et al., 1976; Hangartner and Overton, 1982] generally work at the lower photon energies. However, the low photon energy may not be

adequate for imaging thicker bones, or bones surrounded by large amounts of soft tissue. Dual energy CT can be used to reduce the errors due to variable amounts of fat by measuring the relative concentrations of the mineral and non-mineral components.

An experimental verification of the effect of fat on measured TBD values was carried out using a K_2HPO_4 solution in water and ethyl alcohol. The mineral content of the K_2HPO_4 solution represents the bone mineral, and ethyl alcohol has radiological properties similar to fat. A 100 mg/ml K_2HPO_4 solution was made with varying fractions of 0, 5, 10, 20, 25 and 30% ethyl alcohol. The phantom used in this experiment is shown in Figure 5.1.1. The aluminum insert, of uniform internal diameter, was filled with the desired solution and the phantom was scanned at the 0.4mm aluminum cylinder thickness at 50 kV and 80 kV. The isotransmission line technique of the pre-processing method was applied to the raw data at 50 kV and 80 kV to give bone and soft tissue equivalent images. The mineral contents of the K_2HPO_4 solutions were calculated using SECT and DECT (pre- and post-processing). The measured mineral content decreases linearly as the percentage of alcohol is increased in the solution as seen in Figures 6.1.1 and 6.1.2. For a 10% increase in ethyl alcohol the measured mineral content of a 100 mg/ml K_2HPO_4 solution is reduced by approximately 11 and 7 mg/ml at 80 kV and 50 kV respectively. These values are reduced to approximately 3.2 and 3.5 mg/ml per 10% increase in alcohol with post and pre-processing dual energy methods. The correlation coefficients for these lines illustrate the corresponding increase in precision error in the case of the pre- and post-processing dual energy techniques.

Even dual energy techniques are not able to completely avoid errors due to variable amounts of fat in the measured TBD values. Although the post-processing technique gives two independent measurements of linear attenuation coefficient for trabecular bone, solutions for a three component trabecular bone still requires some assumptions regarding the radiological behaviour of the non-mineral component.

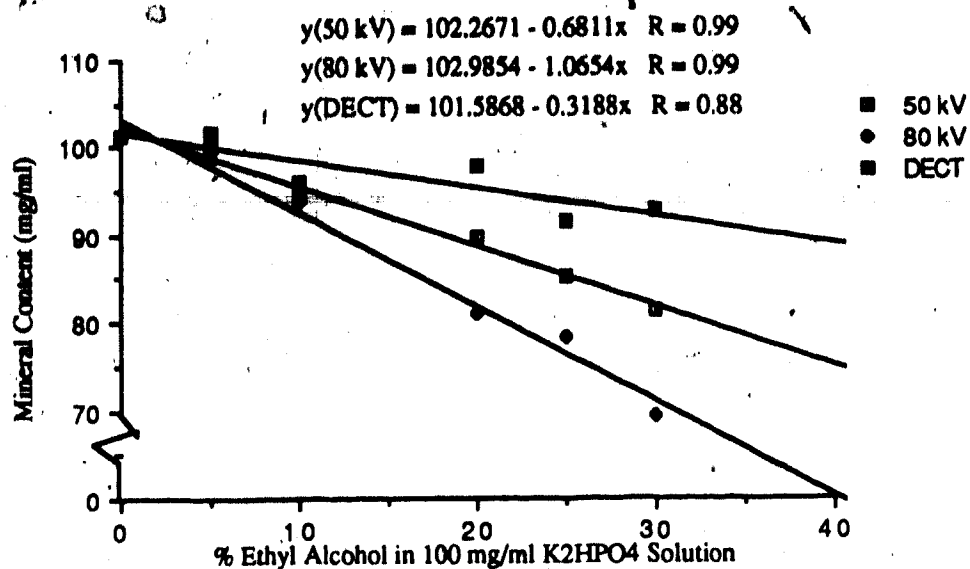


Figure 6.1.1

Measured mineral content as a function of % ethyl alcohol in a 100 mg/ml K_2HPO_4 solution by SECT (50 and 80 KV) and DECT (post-processing) methods.

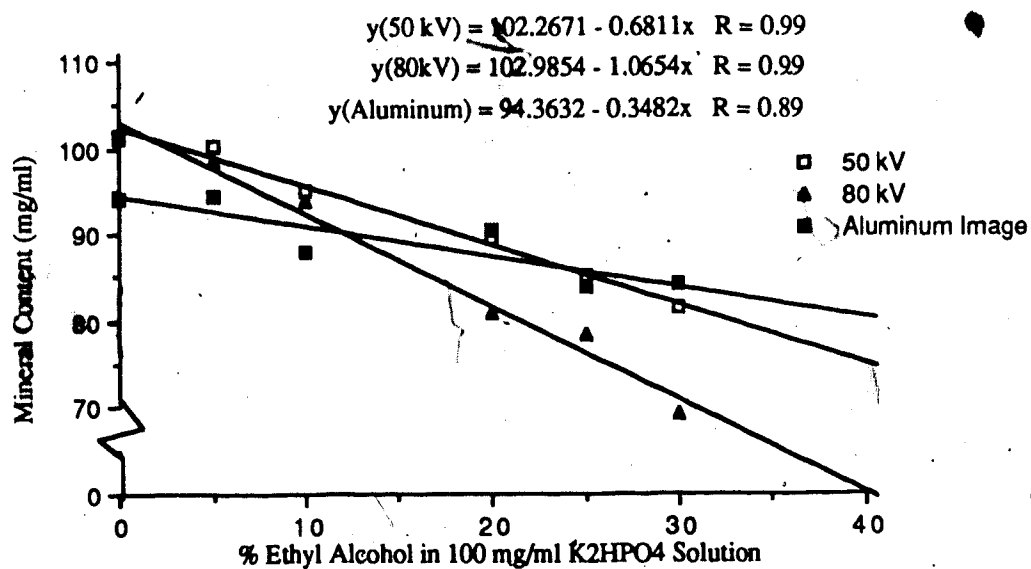


Figure 6.1.2

Measured mineral content as a function of % ethyl alcohol in a 100 mg/ml K_2HPO_4 solution by SECT (50 and 80 KV) and DECT (aluminum image of pre-processing) methods.

The mass attenuation coefficient of the non-mineral component relative to that of water is not the same for the two photon energies. The ratio of the mass attenuation coefficients of soft tissue and water decreases with increasing photon energy; the ratio of the mass attenuation coefficient of fat with respect to water increases with increasing photon energy. Therefore, the ratio of the mass attenuation coefficient of total non-mineral content of the trabecular bone with respect to that of water also varies with increasing photon energy, the nature of these variations being determined by the relative fractions of soft tissue and fat present in trabecular bone. However, the error in the measured mineral content of the trabecular bone due to an unknown amount of fat can be minimised by a proper selection of the two energies [Rao et al., 1987].

Similarly, the pixel values of water and the non-mineral component in the aluminum (bone) equivalent images are not the same thus causing a small error due to variable alcohol content in the 100 mg/ml K_2HPO_4 solution.

6.1.2 Beam Hardening

The X-CT scanner uses a polyenergetic X-ray beam as a photon source. The measured integral attenuation values are not correct since the energy spectrum changes as the beam passes through the material. The errors are propagated through the reconstruction process so the pixel values for trabecular bone will depend upon the density and quantity of the surrounding soft tissue. There are always quantitative discrepancies in the measured TBD values due to this spectral hardening unless a post-processing, material selective beam hardening correction is applied [Rüeggsegger et al., 1978]. All other types of beam hardening correction make assumptions about the distribution of material in a cross-section. For example, each integral attenuation is assumed to be caused by a certain combination of aluminum and plexiglass in the case of the X-CT scanner. On the other hand, the material selective beam hardening corrections are numerically very tedious to perform and involve iterative solutions for the final image.

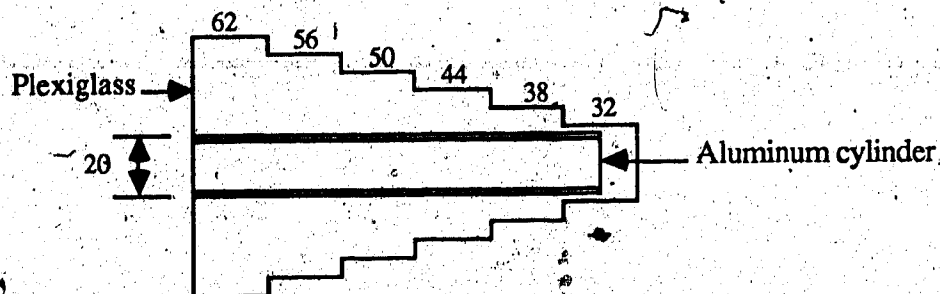


Figure 6.1.3

Section through the beam hardening phantom. The inner aluminum cylinder is filled with a 150 mg/ml K_2HPO_4 solution. The aluminum cylinder is surrounded by a solid plexiglass cylinder of variable diameter. All dimensions in mm.

The dual energy pre-processing procedure theoretically removes the beam hardening errors. A monoenergetic image of the object is reconstructed from the aluminum and plexiglass equivalent images. The pixel values in the reconstructed monoenergetic image represent the average linear attenuation coefficient of the materials present in a unit volume (voxel) at a specified photon energy. The coefficients a_1 and a_2 (section 5.2.2.1) are used to give the linear attenuation coefficient at an energy, E , by following equation:

$$\frac{\mu(E)}{\rho} = a_1 \frac{\mu_{PL}(E)}{\rho_{PL}} + a_2 \frac{\mu_{AL}(E)}{\rho_{AL}} \quad (6.1.1)$$

where $\mu_{PL}(E)$ and $\mu_{AL}(E)$ are the linear attenuation coefficients of plexiglass and aluminum at energy, E .

The errors due to beam hardening were studied for the X-CT scanner using a phantom shown in Figure 6.1.3.

An aluminum cylinder representing cortical bone was filled with a 150 mg/ml K_2HPO_4 solution while the outer plexiglass cylinder of variable diameter represented the soft tissue surrounding cortical bone. This phantom was scanned at 50kV and 80kV at each step of the plexiglass cylinder. Single energy images were reconstructed at 50kV and 80kV using the proposed beam hardening correction. The aluminum and plexiglass equivalent images were also reconstructed using the isotransmission line method, and these images

were used to determine the monoenergetic images at 50keV. For each image, the average pixel values were determined in an area of 1201 pixels within the aluminum insert. The mean pixel value of the K_2HPO_4 solution at 50 kV and 80 kV; and the aluminum equivalent images, were obtained and the percentage deviations from the mean were determined corresponding to the different plexiglass diameters (Table 6.1.1).

Diameter of plexi Cylinder (mm)	Percentage Deviation from Mean			
	50 kV	80 kV	Aluminum	50 keV
32	-1.62	-2.48	3.8	0.34
38	-0.94	-0.91	-0.74	0.19
44	-0.43	-0.40	-0.14	-0.14
50	0.89	0.92	-0.30	0.00
56	1.62	1.73	-1.70	-0.14
62	1.96	2.46	-2.70	-0.34

Table 6.1.1: The percentage deviation of pixel values of beam hardening phantom at 50kV, 80kV, aluminum and mono-energetic images

The error in the mean pixel value changes from -1.62% to 1.96% and from -2.48% to 2.46% at 50 kV and 80 kV respectively. These errors are reduced in the monoenergetic images at 50 keV from 0.34% to -0.34%. The errors in the aluminum equivalent images result from the assumption of an isotransmission line for the logarithmic attenuation as a function of aluminum and plexiglass thickness for the case of a polyenergetic beam. The errors in the thicknesses of aluminum and plexiglass plates used in the isotransmission line calibration procedure also contribute to the overall error for both the aluminum equivalent and monoenergetic images. However, a comparison of the errors in the aluminum images with the rest of the data is questionable since the aluminum equivalent images have more noise compared with the 50kV, 80kV and monoenergetic images.

6.1.3 Scattering and Exponential Edge Gradient Effect

In the diagnostic X-ray energy range the second major process of photon interaction is scattering (coherent and Compton). A photon interacting with the material through

scattering is deflected from its path with either the same (coherent) or a lower (Compton) energy. Therefore, scattered photons measured by the detectors do not reflect the attenuation properties of the material along a direct path from the source to detector. The observed transmitted intensity is thus increased due to scattering and hence the integral attenuation value is decreased.

The scattered radiation results in significant errors (1 to 5%) in TBD measurements [Hangartner, 1987]. The measured attenuation in a bone cross section is decreased due to the scattered photons at all points in a projection profile. A filter function containing negative elements at all spatial positions except at the center is used to filter these projection profiles. The resulting filtered projection will have larger than expected values within the trabecular bone since smaller than expected values of attenuation by cortical bone are used in the convolution process. Therefore the pixel values within the trabecular bone are increased due to scattering.

The phantom of Figure 5.1.1 was used to study the errors caused by scattering. The inner aluminum cylinder was filled with 150 mg/ml K_2HPO_4 solution and the outer plexiglass cylinder was filled with distilled water. The variable thickness of the aluminum ring represents the variable thickness of cortical bone in the appendicular human skeleton. This phantom was scanned at all steps of the aluminum ring for X-ray tube potentials of 50kV and 80kV respectively. The single energy images at 50kV and 80kV were reconstructed without scattering correction. The data at the two energies was used to generate the aluminum and plexiglass equivalent images using the isotransmission line approach. The percentage increase in the mean pixel value of the K_2HPO_4 solution as a function of aluminum ring thickness is given in Table 6.1.2 for 50kV, 80kV and the aluminum equivalent images. The corresponding results for distilled water pixel values are shown in Table 6.1.3.

The data in Tables 6.1.2 and 6.1.3 indicates that errors due to scattering are greater at 50kV than at 80kV, in spite of the fact that the scattering fraction of total attenuation

cross-section increases with the photon energy. The increase in water pixel values in the aluminum equivalent images is more than the corresponding values for the K_2HPO_4 solution. These results cannot be explained solely on the basis of scattered radiation since a similar increase in pixel values results from the Exponential Edge Gradient Effect (EEGE) as the thickness of the aluminum ring is increased. The EEGE is the result of finite beam width, heterogeneity of material within the beam and the exponential nature of photon attenuation [Joseph, 1981]. The photon detector system collects the average transmitted intensity over the beam width. The attenuation R is then calculated by following equation:

$$R = \ln \left(\frac{I_0}{I} \right) = \ln \left[\frac{W}{\int \exp \left(- \int \mu(x,y) dS \right) dR} \right] \quad (6.1.2)$$

where W is the beam-width, and I_0 and I are incident and transmitted beam intensities respectively. Parameters dS and dR are small lengths along and across the beam path respectively. If the linear attenuation coefficient $\mu(x,y)$ is constant in direction of dR , equation (6.1.2) can be simplified to:

$$P = \int \mu(x,y) dS \quad (6.1.3)$$

Aluminum ring thickness (mm)	Percentage change in mean pixel value		
	50 kV	80 kV	Aluminum Image
0.4	0	0	0
1.0	0.14	0.46	-1.12
2.0	1.37	0.47	19.36
3.0	2.51	0.48	25.2
4.0	3.03	1.30	23.4

Table 6.1.2: Percent change in the water pixel value as a function of aluminum ring thickness.

Aluminum ring thickness (mm)	Percentage change in mean pixel value		
	50 kV	80 kV	Aluminum Image
0.4	0	0	0
1.0	0.3	0.06	0.5
2.0	1.40	0.20	2.8
3.0	1.78	0.50	2.6
4.0	2.70	1.07	2.4

Table 6.1.3: Percent change in the pixel value of K_2HPO_4 solution as a function of aluminum ring thickness.

Aluminum ring thickness (mm)	Percentage change in mean pixel value							
	Single energy image					Aluminum image		
	30 keV	40 keV	50 keV	60 keV	70 keV	30-50 keV	40-60 keV	50-70 keV
0.4	0	0	0	0	0	0	0	0
1.0	2.7	0.86	0.3	0.1	0.1	20	12	3.5
2.0	4.1	1.6	0.7	0.3	0.2	28	22	15
3.0	3.8	1.7	0.9	0.3	0.2	25	21	20
4.0	3.9	1.8	0.6	0.5	0.3	12	19.6	9.2

Table 6.1.4: Percent change in the water pixel value as a function of aluminum ring thickness.

The attenuation sums P and R will not be the same for a beam path partially filled by cortical bone. It can be shown that the measured attenuation R will always be smaller than the true attenuation P if the beam path is occupied by two or more different materials [Joseph and Spital, 1981]. The nature of the error in the measured attenuation is, therefore, similar to that resulting from scattering. It should be noted that errors due to EEGE will disappear if either the photon beam is infinitely small or a homogeneous material is present in the beam.

In order to estimate the relative contribution of the EEGE to the errors in Tables

6.1.2 and 6.1.3, the phantom of Figure 5.1.1 was simulated mathematically. The inner and outer cylinders were assumed to be filled with water. The linear attenuation coefficients were taken from tables available for each material [John and Cunningham, 1983]. The raw data was calculated using a beamwidth of 1.28mm for an object size of 75mm over a range of photon energies (30keV- 70keV). In order to simulate the EEGE errors attenuations were calculated by averaging the intensities over the proposed beamwidth. The images corresponding to each step of the aluminum ring thickness were reconstructed at all photon energies. The mean pixel value for water in the inner aluminum cylinder was found for each aluminum ring thickness. The percentage change in the mean pixel value as function of aluminum ring thickness is shown for different photon energies in Table 6.1.4. Similar results for the aluminum equivalent images are also shown for a several pairs of photon energies in Table 6.1.4. The following observations can be made from this data.

- (1) The percentage change in pixel value for 50kV images as a function of increasing aluminum ring thickness falls between the corresponding values in the simulated images at 30keV and 40keV. Hence the errors at 50kV result mainly from the EEGE instead of scattering.
- (2) The percentage change in the pixel values due to EEGE at 50-70keV is very small since the radiological contrast decreases with increasing photon energy. Hence a significant portion of the errors at 80kV is caused by scattered radiation. The errors due to scattering at 80kV, however, happen to be less than the errors due to EEGE at 50kV.
- (3) The percentage change in the pixel value due to EEGE in the aluminum equivalent images for the 30-50keV and the 40-60keV pairs are very large, so the errors in the aluminum equivalent images for the 50-80kV pair have a major contribution due to the EEGE effect. The EEGE errors, however, will decrease as the radiological contrast decreases. Since a 150mg/ml K_2HPO_4 solution has attenuation properties closer to aluminum than water, the errors due to EEGE will be smaller for a 150 mg/ml K_2HPO_4 solution than for water (Tables 6.1.2 and 6.1.3) contained in the aluminum cylinder

considered in the aluminum equivalent images.

The observations made above are only approximately true since the actual energy spectrum of the X-ray beam at 50 and 80kV is not known. The 50kV beam is assumed to have a relatively large portion of 30 to 40keV photons while the 80kV beam may have significant intensities at 50-70keV photon energies.

The results so far suggest that in order to measure TBD independent of the variations in the cortical bone thickness (aluminum ring thickness in the experiment), a scattering correction must be made at 80kV. The error due to EEGE should be corrected both at 50kV, and in the case of the pre-processing dual energy approach. The EEGE errors can be corrected by Fourier deconvolution or by the 'Local Ray' correction method [Joseph and Spital, 1981]. No attempt was made to implement EEGE or scattering corrections here since:

- a) The quantitative uncertainty in TBD measurements resulting from scattering and EEGE is important only in the case of variations in the cortical thickness of bone, and hence is not important in a short-term longitudinal study.
- b) The change in pixel values for a wide range of aluminum ring thicknesses is not more than 3% for a 150mg/ml K_2HPO_4 solution.
- c) Corrections for both EEGE and scattered radiation are time consuming.

6.2 Precision

The TBD measurement procedure should always produce the same result for a given quantity of bone so that the deviation, or variability, in a set of measurements can be defined as the precision or reproducibility of the bone mineral measurement procedure.

Two major factors affect the reproducibility of TBD measurements by quantitative CT; the first is the precision of the measurement of linear attenuation coefficients in a CT image containing a number of volume elements ('voxels') within the trabecular bone

region; the second is the reproducibility of the trabecular bone volume used in the analysis procedure.

6.2.1 Precision of Linear Attenuation Coefficient

The pixel value in a CT image gives only an estimate of the average linear attenuation coefficient for the materials present in a 'voxel'. The noise in the attenuation profile resulting from the limited photon fluence contributes to the pixel noise. The stability of the calibration data (dead-time and beam hardening coefficients) is another important parameter in determining the precision of the pixel values. In quantitative CT the pixel values within trabecular bone are averaged to produce the mean pixel value used in the TBD calculations. A better precision for TBD measurement is obtained if a large number of low noise pixels, for a given physical area of the trabecular bone, is used to calculate the mean pixel value. The standard error σ_μ in the mean pixel value μ for N pixels is given by:

$$\sigma_\mu = \frac{\sigma}{\sqrt{N}} \quad (6.2.1)$$

where σ is the standard deviation.

The standard deviation σ depends on the radiation dose to the subject, and the number of pixels depends upon the spatial resolution of the scanner. A good spatial resolution is obtained with the X-CT scanner by using a multiple rotation fan-offset technique, as discussed in section (3.2). The effective beam width of the scanner varies from 1.28 to 1.36mm for objects of 75 to 220mm diameter. This means that high contrast objects (e.g. lead strips) of diameter 0.64 to 0.68mm can be resolved in the CT image [Wells, 1986].

Although noise can be introduced to corrupt the data at any point in the CT image process the principal source is the random, statistical noise arising from the detection of a finite number of x-ray quanta in the projection measurements. The effect of this noise

the precision of the linear attenuation coefficient was studied by scanning a 100mg/ml K_2HPO_4 solution at different speeds. The phantom of Figure 5.1.1 containing the mineral solution was scanned at three rotational speeds, at X-ray tube potentials of 50 and 80kV. The aluminum and plexiglass images were reconstructed from the projection data at two beam qualities by the isotransmission method. The percentage standard error in the mean pixel value of a region of 1201 pixels was determined for each image. The results are shown in Table 6.2.1 for 50kV, 80kV, aluminum and plexiglass images.

speed (Hz)	Percentage standard error			
	50 kV	80 kV	Al- Image	Plexi- Image
2000	0.23	0.28	2.0	0.92
1000	0.17	0.21	1.5	0.65
500	0.14	0.17	1.1	0.48

Table 6.2.1: Standard error in mean pixel value as a function of the rotational speed of the scanner.

The standard error in the aluminum and plexiglass images is much higher than in the 50 and 80kV images. The aluminum and plexiglass equivalent thicknesses are calculated by subtracting the scaled projection ray-sums for the 50 and 80kV X-ray beams, respectively to reconstruct the aluminum and plexiglass images. The noise in the resulting aluminum and plexiglass equivalent thicknesses is therefore increased giving a larger standard error in these images. Since a larger number of photons is collected in a specified angular sampling interval ($2/3^\circ$) as the rotation speed is decreased so the standard error in mean of pixel values decreases.

In order to estimate the short term variations in pixel values, a 200mg/ml K_2HPO_4 solution was scanned repeatedly over a period of one hour, both at 50kV and 80kV. The mean of 1201 pixels was determined for each measurement in 50kV, 80kV and aluminum images. Table 6.2.2 shows the coefficient of variation (CV) in the mean pixel value of the 50kV, 80kV and aluminum images.

	50kV	80kV	Aluminum
Mean	7597.0	6994.0	926.1
Standard Deviation	9.17	19.93	3.17
Number of scans	14	13	10
CV%	0.12	0.29	0.34

Table 6.2.2: The coefficient of variation in pixel values of a 200mg/ml K₂HPO₄ solution.

6.2.2 Comparison of Dual Energy Methods

The dual energy post-processing technique is applied to the mean pixel values so the standard error can be calculated for the resulting TBD value. Assuming that the standard error of the estimate of the slope and intercept of the calibration lines (section 4.1.3) is very small, the standard error σ_{TBD} in TBD values as determined by the post-processing dual energy method is then given by:

$$\sigma_{\text{TBD}} = \frac{\sqrt{\left(\frac{\sigma_{\mu_1}}{a_1}\right)^2 + \left(\frac{\sigma_{\mu_2}}{a_2}\right)^2}}{\frac{\mu_1}{a_1} - \frac{\mu_2}{a_2}} \quad (6.2.2)$$

where σ_{μ_1} and σ_{μ_2} are the standard errors in mean pixel values of the trabecular bone (μ_1 and μ_2) at two energies. The coefficients a_1 and a_2 are the intercepts of the calibration lines at the two energies.

The standard error of TBD measurement using the dual energy pre-processing method can be calculated as follows:

$$\sigma_{\text{TBD}} = \frac{\sigma_{\text{AL}}}{\mu_{\text{AL}} - a_{\text{AL}}} \quad (6.2.3)$$

where μ_{AL} and σ_{AL} are the pixel values of the trabecular bone and its standard error in the

aluminum image; a_{AL} is the intercept of the calibration line for the aluminum images.

The percentage standard error of the TBD measurement for the pre- and post-processing methods was determined from equations (6.2.2) and (6.2.3) using the data of Table 6.2.1. The results are given in Table 6.2.3.

speed (Hz)	Percentage standard error	
	Pre- processing	Post- processing
2000	3.06	2.96
1000	2.35	2.2
500	1.79	1.74

Table 6.2.3: The standard error of TBD for pre- and post-processing dual energy methods.

6.2.3 Repositioning Errors

The spatial resolution in the 'scout' image is determined by the spatial resolution of the scanner in the axial direction. The source and detector collimator have physical aperture widths of 1mm and 3mm, respectively in the axial direction. The effective beam aperture in the axial direction at the center-of-rotation is determined by the source and detector collimator apertures and the SCR distance. The effective beam aperture in the axial direction can be calculated by the same method as for the transaxial direction (section 3.3.1). The effective beam aperture for the X-CT scanner for the 75mm diameter setting was found to be 1.8mm. Therefore, the position of a high contrast edge in the axial direction can be reproduced to ± 0.9 mm. The measurement site determined by the scout image helps in repositioning the same region of bone for measurement in a serial study.

The errors in determining the measurement site are further reduced by using operator defined area limits, and interpolation in the integration in calculating volumetric TBD (section 4.3). In this way, a highly reproducible, particular bone volume is always used to calculate volume averaged TBD so a small error in the area of trabecular bone, in

each measured slice, resulting from the error in repositioning does not affect the volume of the bone for TBD analysis in a serial study.

The repositioning errors were studied by measuring TBD at the distal end of a cadaver femur, *in-vitro*. The measurements were carried out at 50kV, 2.8mA, and the SCR distance was set for an object of 150mm diameter. The scanner was reset and the laser beam cross-hair positioned at approximately 5cm cranial to the distal end of femur. A 'scout view' was reconstructed using the method discussed in section 4.1 (Figure 6.2.1). The horizontal lines in Figure 6.2.1 give the distance between laser beam cross-hair and the distal end of femur. A set of 10 slices was taken at 2mm intervals starting at a distance of 4cm from the distal end. The axial position of the femur bone was then altered and 'scout view' again carried out to repeat 10 slices spaced at 2mm intervals.

Measurement Number	TBD (gms/ml) K_2HPO_4
1	142.2
2	142.1
3	140.9
4	141.8
5	141.1
6	143.6

Table 6.2.4: The volumetric TBD (gms/ml K_2HPO_4) for six measurements of femur.

This experiment was repeated 6 times for the same bone, each time altering the axial position with respect to the laser beam cross-hatch.

There were no apparent artifacts in the reconstructed images for the six different measurements. Therefore, the image and TBD analysis procedures were applied to these images (sections 4.2 and 4.3). All six measurements were analyzed simultaneously and the same lower and higher area limits used in each case to calculate the volumetric TBD. The calculated volumetric TBD is shown in Table 6.2.3.

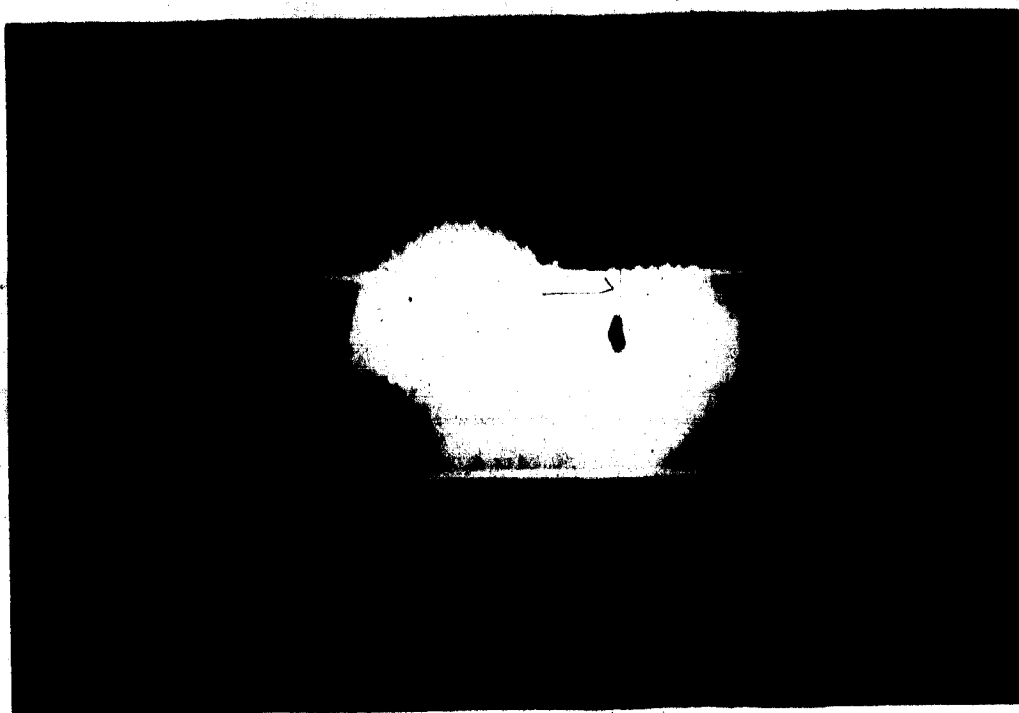


Figure 6.2.1
Digital radiograph at distal site in a cadaver femur.

The mean TBD and standard deviation from six measurements are 141.9 and 0.95 giving a TBD measurement precision of 0.67%

6.3 Results

The X-ray CT scanner is presently being used in several bone research studies. In one study TBD measurements are carried out for a number of human cadaver femurs both at the distal and proximal sites including the femoral neck. This data will be compared with histomorphometric studies on these same bones. In another study TBD in a group of post-menopausal women is being measured in order to assess the effects of exercise at different skeletal sites. For this study, the X-ray CT scanner is being used to measure TBD in the distal tibia. In this section preliminary TBD measurement data for cadaver femur and *in vivo* measurements is presented.

6.3.1 Cadaver Femur Measurements

Using the X-ray CT scanner TBD measurements were carried out at the distal and proximal femur and femoral neck sites for two frozen human cadaver femur bones. Both the SECT (50 and 80kV) and DECT (pre- and post-processing) techniques were used for TBD measurements.

For the distal femur the measurement site was located by the 'scout view' as shown in Figure 6.2.1, at a distance of 3.5cms from the distal end of femur. Starting at this measurement site, two sets of 20, non-overlapping slices, each spaced 2mm proximally, were obtained at X-ray tube potentials of 50kV and 80kV. The CT images were reconstructed at the two energies for each of the 20 slices, and by using the isotransmission lines approach, aluminum and plexiglass equivalent images were also generated. The outer contour of the cortical bone was determined by the EDCORP algorithm and TBD analysis was performed using SECT (50 and 80kV) and DECT (pre-and post-processing)

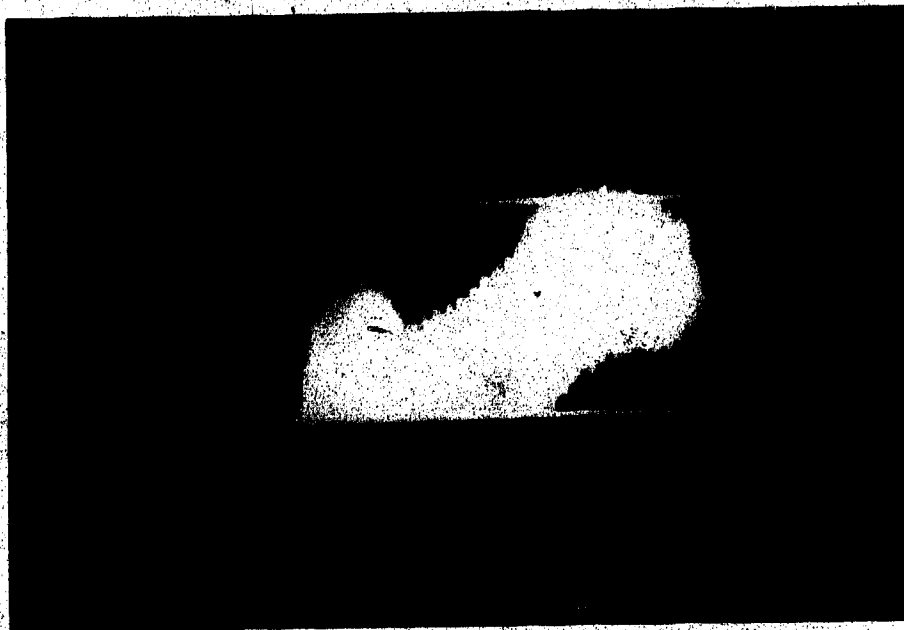


Figure 6.3.1
Digital radiograph at proximal site in a cadaver femur.

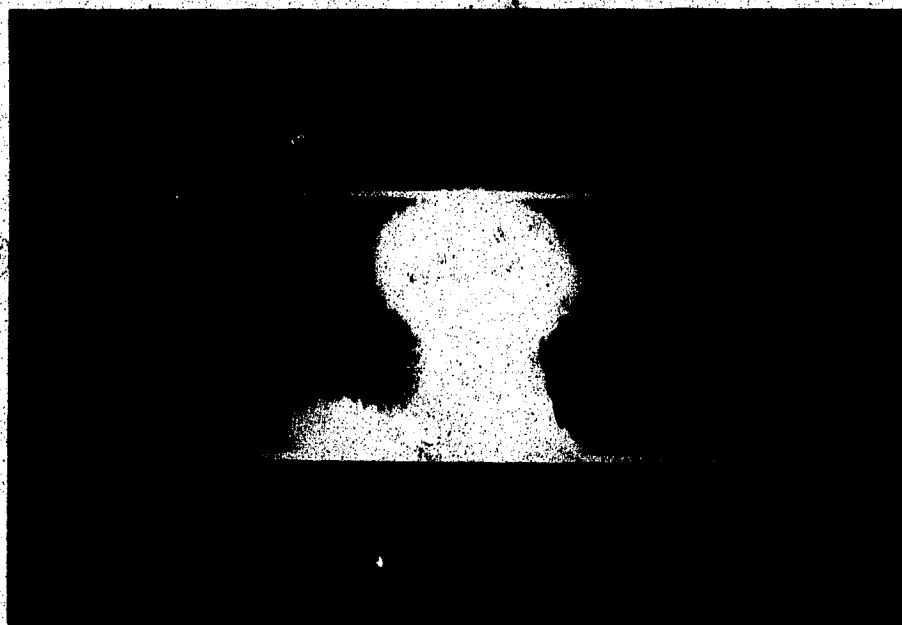


Figure 6.3.2
Digital radiograph at femoral neck site in a cadaver femur.

techniques (section 5.0). The inner 45% area enclosed by the outer cortical bone contour was assumed to be trabecular bone and mean pixel values within this area, for 50kV, 80kV and aluminum images, were used to calculate TBD (gm/ml K_2HPO_4) at each slice position. The aluminum images were used in the pre-processing DECT technique. For a particular bone the same low and high area limits were used in equation (4.3.1) to calculate the volumetric TBD in each of the measurement techniques. The results for two femurs are shown in Table 6.3.1.

Femur	TBD (gms/ml. K_2HPO_4)											
	Distal				Proximal				Femoral Neck			
	SECT		DECT		SECT		DECT		SECT		DECT	
	50 kV	80 kV	Pre	Post	50 kV	80 kV	Pre	Post	50 kV	80 kV	Pre	Post
1	137	112	150	160	123	106	134	140	237	204	258	270
2	91	75	104	105	144	133	152	155	242	234	254	271

Table 6.3.1: TBD (gms/ml. K_2HPO_4) of cadaver femurs at different sites measured by SECT (50kV, 80kV) and DECT (pre- and post-processing) techniques.

The 'scout view' of the proximal site is shown in Figure 6.3.1. The distance between the scanner reset position (laser beam cross-hair) and the end of the femoral neck was determined from the two horizontal bars shown in the 'scout view'. The first measurement site was located at a distance of 5.5cm from the end of femoral neck. As in the case of distal femur the same two sets of 20 slices were again obtained at 50kV and 80kV. The procedure for calculating the TBD was similar to the distal measurements except that 30% of the total bone area enclosed by the outer cortical bone contour was assumed to be trabecular bone and different lower and higher area limits were used for calculating the volumetric TBD. A 30% instead of 45% of the total bone area was necessary in order to

exclude from the TBD analysis, a small, wedge-like cortical structure extending into the trabecular envelope. The volumetric TBD for two femur bones are given in Table 6.3.1.

A 12cm length of the proximal femur including the femoral neck, was physically separated from the rest of the femur in order to measure the TBD at the femoral neck site. The sectioned bone was placed in the scanner such that the femoral neck was aligned parallel to the longitudinal axis of scanner. For these measurements the first measurement site was located at a distance of 1cm from the end of neck as shown in Figure 6.3.2. The TBD measurement procedure was similar to that for the distal femur for each of the SECT and DECT techniques. The volumetric TBD of the femoral neck sites of two femur bones are given in Table 6.3.1.

6.3.2 *In vivo* Measurements

The procedure for TBD measurement in the human distal femur and proximal tibia was demonstrated in two normal subjects. Simultaneous data collection for X-ray tube potentials of 50kV and 80kV is not possible with the present set-up for data acquisition in the X-ray CT scanner. These measurements were, therefore, only carried out at 50kV.

Subject	Age (Years)	TBD(gms/ml. K_2HPO_4)	
		Distal Femur	Proximal Tibia
1	30	230	191
2	28	152	117

Table 6.3.2: TBD (gms/ml. K_2HPO_4) at the distal femur and proximal sites for two normal male subjects.

The axial measurement sites for the distal femur and proximal tibia were determined using the horizontal lines in the 'scout view' shown in Figure 4.1.2. These lines gave the

distances of the two sites from the scanner reset position. The scanner was first moved to the distal femur site at 3.5cm proximal to the lower line (Figure 4.1.2). A set of 10 slices was taken craniad to the first measurement site, each slice separated by 2mm. A similar set of slices was taken distally from the first measurement site for the proximal tibia. The outer cortical bone contour was determined and TBD at each slice position obtained assuming trabecular bone occupies 45% of total bone area. The volumetric TBD for two subjects at each site is given in Table 6.3.2

7.0 Discussion

The X-CT scanner is a unique example of the application of a multiple rotation, fan-offset geometry with a count mode data acquisition system, which combine to provide a high geometrical and physical resolution at a very low radiation dose (less than 20mR). Evaluation of the X-CT scanner with respect to its geometrical parameters (effective beam apertures, focal spot dimensions etc.) and precision of various scanner movements have been carried out previously [Wells, 1986]. This section contains brief discussion of the performance of scanner including the accuracy and precision obtained using different techniques of TBD measurement.

7.1 Scanner Performance

Detector system calibrations, such as spectral matching, dead-time and beam hardening (section 3.2.1 to 3.2.4), and geometrical calibrations such as fan-beam centering, detector angles and SCR distance evaluations (sections 3.2.5 and 3.2.6), have now been optimized to give artifact free images. It was found that detector system calibrations are required at about 2-week intervals, and that they can be easily performed in 2-3 hours for both 50kV and 80kV. The effectiveness of these calibrations can be seen in the artifact-free images shown in this thesis (sections 3.2 and 4.2.2). Moreover, in the rotate-rotate scanning geometry artifacts due to imperfect calibration of particular detectors result in circular ring artifacts with specific radii. This characteristic facilitates the fast identification of faulty detectors.

The geometrical calibrations for the X-CT system are, however, very cumbersome and time consuming. Multiple measurements are required to calculate the SCR distance and detector angles, which increases the calibration time significantly. However, the geometrical calibrations were found to be very stable and needed repeating only once per year at a 50kV tube potential for an object size setting of 75mm diameter. SCR distance at

the other object size settings (100mm and 150mm diameters) were simply obtained from 75mm setting by adding the linear movement of vertical motor required for these settings. There are no geometrical artifacts in the images as long as the initial position of the scanner motors (reset scan position) is accurately determined before each data collection.

The data collection and image reconstruction were carried out separately for the X-CT scanner as fan-beam projections were available only after the five rotations. Data collection time is less than half the scan time of ^{125}I scanner [Hangartner and Overton, 1982]; this time can be further reduced by using faster data acquisition systems (section 9.2). This relatively small data collection time (50 seconds) and automatic axial movements of the scanner result in faster subject measurement times and thus decrease movement artifacts.

With the exception of the distal femur measurement, in which the operator has to interactively remove the patella from the image, the cortical bone contour is determined automatically. A single, interactive TBD program calculates TBD by SECT (50kV, 80kV) and DECT (pre- and post-processing) techniques.

7.2 Accuracy

The accuracy of TBD measurement is dependent upon the linearity of the detectors, beam hardening, scattering, EEGE and the variable amount of fat content present in trabecular bone. A correlation of $r=0.98$ is found with the X-ray tube current as a function of photon counts corrected for deadtime. Pixel value of calibration solutions in 50kV, 80kV and aluminum images correlate highly with the concentration of solutions (Figure 5.1.1 and 5.2.5). These results compare well with the ^{125}I scanner [Hangartner and Overton, 1982] and are better than those obtained by Genant and Boyd [1977] with the EMI head scanner.

For the X-CT scanner a 10% increase in ethyl alcohol content in a 100mg/ml K_2HPO_4 solution decreases the measured mineral content by 7mg/ml at 50kV and by 11mg/ml at 80kV. These results fall within the range of values in the literature [Laval-

Jeantet et al., 1986; Goodsitt and Rosenthal, 1987; Genant and Boyd, 1977]. Laval-Jeantet et al. found a decrease of 11mg/ml at 85kV_p and 13mg/ml at 140kV_p, in the measured spinal mineral content for a 10% increase of actual fat content. Goodsitt and Rosenthal showed a decrease of 8mg/ml at 80kV and 10mg/ml at 140kV in spinal mineral content. In an *in vitro* study similar to that described in section 6.1.1, Genant and Boyd presented mineral content as a function of % alcohol by volume in a 5mg% K₂HPO₄ solution at 80kV and 140kV. They showed a 9% and 12% decrease in mineral content for a 10% increase in alcohol by volume respectively. The DECT pre- and post-processing techniques of X-CT reduce the error to 3.2mg/ml and 3.5mg/ml for 10% alcohol respectively. Laval-Jeantet et al. [Laval-Jeantet et al., 1986] obtained an error of 7mg/ml by DECT (post-processing) at 80kV_p and 130kV_p, and Genant and Boyd [Genant and Boyd, 1977] showed that the dual energy results for mineral content were within one standard deviation (10%).

Numerous difficulties arise when comparing these results. The fat-dependent error decreases as the photon energy decreases (Figures 6.1.2 and 6.1.3) which makes it a function of the X-ray tube potential and added beam filtration. Another factor is the use of different equivalent fat material to represent these errors. Since the physical density of ethyl alcohol is 0.8mg/ml compared with 0.92mg/ml for fat, an overestimation of the error due to fat is obtained using ethyl alcohol. A true comparison can only be made in equivalent situations.

The pre-processing CT techniques have not been generally used because of calibration and operational difficulties. Moreover, other than separate visualization of bone and soft tissue, this technique does not reduce the errors shown by the post-processing technique as far as the effect of fat content on the TBD measurement is concerned (Figures 6.1.2 and 6.1.3). In the case of the X-CT scanner the data collection for the pre-processing technique requires the object to be at the same position with respect to the center-of-rotation when it is scanned at the two energies with different photon beam filters. Any deviation of the object from its previous position results in artifacts in the aluminum and plexiglass

equivalent images. In the post-processing technique the results are calculated from the mean pixel values of lower energy and higher energy images so small variations in the position of the object when scanned at two energies are not important. The pre-processing results can be improved by simultaneous data collection at two energies which removes the errors due to small movements.

The two beams (50kV and 80kV) are heavily filtered, with 0.65mm and 2.75mm copper respectively, to reduce the spectral hardening. However, if beam hardening corrections are not applied artifacts in the CT images result due to hardening of the beam and to the variable response of the detectors to photon energy. Not only the actual hardening of the beam but also the nature of the correction procedure contributes towards the errors given in Table 6.1.1. The polynomial coefficients are determined by measuring the projection ray-sums for a number of sandwiches containing 5.85mm plexiglass and 0.85mm aluminum. The effective attenuation coefficient of such a sandwich is smaller than that of aluminum, and greater than that of plexiglass. Therefore, an increase only in the plexiglass thickness of the beam hardening phantom (Figure 6.1.4) does not cause as much hardening of the beam as would be assumed by this correction procedure resulting in an over-correction of the projection ray-sums before image reconstruction. This factor also explains the opposite nature of these errors in Table 6.1.1 from those of 50keV mono-energetic images for which these errors are a minimum.

The beam hardening errors have been studied in this form by Hangartner et al. [Hangartner et al., 1987] and Vetter et al. [Vetter et al., 1986]. Hangartner et al. found errors ranging from 1.52% to -2.53% for body sizes of 260mm to 410mm for the GE8800 CT used for spinal bone measurement. These authors also found errors ranging from -0.91% to 0.79% for object sizes of 38mm to 63mm for the ^{125}I scanner. Vetter et al. determined an error of 12% at 125kV and 3% for pre-processing for object sizes of 19 to 33cms. However, these results cannot be directly compared with our results since a different beam quality was used.

An experiment similar to that performed by Hangartner et al. [Hangartner, 1987] was performed to study the scattering and EEGE errors for this scanner. These errors are, however, only important when the thickness of the cortical bone changes along with TBD. A major contribution to the total error at 50kV is the result of EEGE (section 6.1.3) since the detector collimator of the scanner has been designed to minimize the detection of scattered radiation. These errors at 50kV are much smaller than the corrected or uncorrected errors of the ^{125}I scanner [Hangartner, 1987] since the EEGE effect is larger at the 29keV photon energy due to a larger radiological contrast between bone and soft tissue. Scattering and EEGE errors at 80kV are smaller than those at 50kV since EEGE error decreases due to decreased radiological contrast and the increased scattered radiation is excluded by collimation. In the aluminum images errors similar those at 50kV occur because the errors arising for the two single energies propagate into the aluminum equivalent thickness calculated from the projection ray-sums at the two energies.

7.3 Precision

The precision of pixel values is determined mainly by statistical photon noise. At a scan time of 50 seconds (2000 Hz rotational speed), the coefficient of variation (CV) of pixel value of 200mg/ml K_2HPO_4 solution (one standard deviation of mean) is 0.12%, 0.29% and 0.34% at 50kV, 80kV and in aluminum equivalent images respectively.

The sensitivity for measuring changes in TBD at a given precision depends upon photon energy, and on the technique of TBD calculation; it is determined from the slope of the corresponding calibration line. The standard error of TBD measurement is determined by the standard error of pixel values and sensitivity of the measurement technique, and is determined by propagation of errors in the corresponding equations of the various TBD calculation techniques. This value is determined to be 1.04%, 2.2%, 3.06% and 2.96% for 50kV, 80kV, pre-processing and post-processing techniques respectively, for a 100mg/ml K_2HPO_4 solution. Therefore, the sensitivity is better at 50kV than at 80kV because a larger

error at 80kV is obtained for a similar error of pixel values (0.23% and 0.28%). This results from dependence of the photoelectric effect on the third power of the atomic number of the material in the lower photon energy range. This finding is in agreement with those obtained by simulation [Müller et al., 1985].

Although the standard error of the pixel values in the aluminum images is large compared to those in the 80kV images, the standard errors of the TBD measurement differ by less than 50% in the two cases. This is another example of increased sensitivity of the TBD measurement which is better for aluminum images since the changes in TBD contribute significantly to the pixel values of the aluminum images with negligible contribution from soft tissue. Similarly, the sensitivity of the TBD measurement by DECT (post-processing) is very good because the contributions of soft tissue to the pixel values in 50kV and 80kV are almost cancelled when TBD is calculated by subtracting one from the other.

Longitudinal studies require that subjects serve as their own controls which stresses the need for good reproducibility in TBD measurement. A reproducibility error of $\pm 0.67\%$ in multiple TBD measurements of a cadaver femur demonstrates the accuracy of determining the measurement site and volumetric TBD by using the same area limits for evaluating the same volume of bone each time.

7.4 Cadaver femur

The data collection, image reconstruction, image analysis and TBD analysis programs of the X-CT scanner were tested on two cadaver femur bones with various TBD measurement techniques. This preliminary data (Table 6.3.1) indicates the presence of relatively large amounts of fat in trabecular bone space at the distal, proximal and femoral neck sites. SECT (80kV) gives the lowest value of TBD at each measurement site of two bones because the linear attenuation coefficient of fat contributes a significant fraction of total linear attenuation coefficient of trabecular bone. At a lower photon energy, where the

photoelectric effect is the dominant photon interaction process, the contribution of fat to total linear attenuation coefficient increases because photoelectric effect depends upon the third power of atomic number of the material and the effective atomic number of fat (6.46) is less than that of bone (12.31) [John and Cunningham, 1983]. TBD measured by SECT (50kV) is therefore larger than that measured by SECT(80kV). Both of the dual energy techniques considerably reduce the effect of fat and give TBD values significantly larger than those given by SECT (50kV and 80kV) techniques.

8.0 Conclusions and Future Developments

8.1 Conclusions

System calibrations for the X-ray fan-beam CT scanner have been developed. Methods to reproduce the volume of TBD analyzed within a particular bone and various image analysis procedures for determining mineral content have been implemented. Trabecular bone can be analyzed as a two component (SECT) or a three component (DECT) model in order to determine its mineral content.

SECT analysis can be performed for a range of photon energies on the X-CT scanner, specifically 50kV and 80kV analysis has been demonstrated to measure the TBD. A number of factors affecting accuracy and precision of TBD measurement have been analyzed at 50kV and 80kV. The TBD measurements at 50kV are superior to those at 80kV in terms of measurement precision and variable fat related errors. Therefore, SECT analysis at 50kV should be preferred to that at 80kV in order to determine the response of skeletal challenge to various stimuli including drugs and physical activity. A short term precision of 0.12% and short terms variations, including repositioning errors, of 0.67% are found at 50kV.

Dual energy techniques implemented on this scanner include the pre- and post-processing analysis which treat the trabecular bone as a three component model. The post-processing technique seems more attractive due its relative simplicity compared the pre-processing technique; it also gives minimum variations in TBD due to the variations of fat content compared to any other method. Both dual energy techniques have a comparable standard error in TBD measurements which is more than that for single energy techniques at 50kV and 80kV. Dual energy techniques provide a more accurate estimate of trabecular bone mineral and hence could be used in a cross-sectional discrimination of normal and osteoporotic subjects. The TBD data measured by both single and dual energy techniques

can be much more useful in clinical applications.

The mono-energetic images of the pre-processing technique are useful, particularly at the lower mono-energy, for quantitative bone measurements since these are free from beam hardening errors. Use of a lower photon energy is useful in reducing the fat related errors. An atomic number and electron density choice of basis images instead of bone and soft tissue basis can be useful in diagnostic radiology in order to identify the atomic number or electron density related pathologies.

8.2 Future Developments

The X-CT scanner as implemented does have advantages over the second generation γ -CT scanner, with its lower scan time and the possibility for multiple site TBD measurement. However, several problems remain with this scanner with respect to TBD measurements by single and dual energy methods, these include:

(1) The scan time per slice is 50 seconds, which is still unacceptably long as patient movement can introduce artifacts in the image; repeating these measurements considerably increases the total time of a bone mass study.

As a result of the fluorescence decay time of NaI(Tl) (250nSec), and signal propagation delays in the electronic circuits, the present photon detector system is limited to count rates less than 750,000 events per second. Reducing the scan time for a given precision in pixel value to say 20 seconds, would require the detector system to operate reliably at rates greater than 10^6 /second.

(2) Data collection at the two energies cannot be performed simultaneously. Also, at the higher energy the amplitude of the current pulse at the anode of the PMT is increased which increases pulse width resulting in additional pulse pile-up which further reduces the count rate. This problem can be solved partially by reducing the difference between the discriminator threshold and the average pulse height of the observed spectrum resulting in smaller pulse width. But the poor energy resolution of some of the existing detectors in this scanner does not allow a difference of less than 200mV. Therefore, in order to achieve

comparable count rates at 50kV and 80kV, a lower PMT high voltage is used at 80kV and the beam is filtered by a thicker copper filter. This necessary arrangement makes simultaneous data collection at the two energies very difficult to achieve. Simultaneous data collection at the two photon energies is particularly useful for pre-processing dual energy measurements since even a small displacement of object between two data collections produces noticeable discrepancies in the measured projection ray-sums at two energies. In post-processing dual energy measurements such data collection would significantly reduce the study time.

A dual energy beam is not easily available with this scanner. There are a number of techniques available for generating a dual energy photon beam. These are: (1) by rapidly switching the high voltage on X-ray tube, (2) by using a split filter approach [Rutt and Fenster, 1980], which divides the fan-beam into two different energies and (3) by using a filter which gives two energy peaks. Rapidly switching the high voltage requires small stabilization times for the high voltage and current from the high voltage generator, and use of a pulsed rather than a continuous output X-ray tube. The high voltage generator for this scanner can switch the voltage and current in about 1.5mSec [Fug], but the X-rays are generated by a filament controlled, continuous output tube which cannot be used for rapid switching. On the other hand, a split filter approach requires a 360° rotation of asymmetric (about the SCR) fan-beam to collect the projection data at the two energies over 180°. For the X-CT scanner, this would require 10 rotations of the scanner to collect data for a 260-point profile at each angular position, for the two energies; which is the same as presently used.

In the following sections, suggestions concerning a dual energy beam method using a special filter, and detector systems for fast single and dual energy data collection are discussed.

8.2.1 Dual Energy Photon Beam

Heavy filtration of the radiation from a stationary anode X-ray tube by a gadolinium filter produces a dual peak X-ray spectrum with the peaks centered at 43keV and 100keV. The X-ray tube needs to be operated at an anode potential of greater than, or equal to, 120kV. In the X-CT scanner the high voltage generator for the X-ray tube can operate up to 120kV and 10mA, but the tube itself can be operated only at maximum anode potential of 100kV. Therefore, a tube capable of operating at an anode potential of more than 120kV, and with similar specification regarding focal spot dimensions and anode angle, is required. Such an arrangement would produce a photon beam for single and dual energy quantitative CT applications without requiring the rapid switching of high voltage or geometrical bisection of photon beam into two energies. The 43keV beam can be used for SECT and both beams can be used for DECT measurements of TBD. A data acquisition system for such a photon beam is suggested in the following section.

8.2.2 Alternative Detectors and Data Acquisition System

The key to a detector system capable of high count rates at good detection efficiency is a scintillation material which has low fluorescence decay time and a high linear attenuation coefficient at the desired photon energies. In the X-CT scanner the counts rates are limited both by the relatively large decay time of NaI(Tl) crystal (250nSec), and by the pre-amplifier response. If the electronic circuits do not introduce signal delay, then the detector system can count up to the theoretical limit of 4 million counts per second set by the crystal. Therefore, fast pre-amplifiers are being tested to increase the count rate. The impulse response of a pre-amplifier currently being tested has rise time of 2nSec and a decay time constant of 40nSec [Rel-labs]. This circuit should be able to increase the count rates up to more than a million counts per second. However, very high count rates can be achieved with such a circuit only if NaI(Tl) crystal are replaced by either germanium or plastic scintillators. A 4mm length of high-purity germanium crystal can offer good photon

absorption efficiencies at 43keV and 100keV [Stebler et al., 1985]. However, a significant operational difficulty arises with the use of germanium since it is required to keep the detectors at liquid nitrogen temperatures.

Another alternative for high speed X-ray photon counting is offered by plastic scintillators which are lead doped polyvinyltoluene compounds. These scintillators are being tested in our lab with a faster pre-amplifier circuit. One major problem with the plastic scintillator is its lower attenuation coefficient than an NaI(Tl) crystal. However after proper doping with lead, these detectors can work at a counting efficiency more than 50% of NaI(Tl) and a small decay time constant of 2.5nSec [NE data manual]. If the absorption efficiency of plastic scintillators is increased, they can be used with a dual beam arrangement using a gadolinium filter for single and dual energy CT applications.

A gadolinium filtered dual beam along with high speed germanium or plastic scintillators requires a new data acquisition system. The pre-amplifier circuit for these detectors must not introduce additional delays which are in terms of rise and fall times of voltage pulses, larger than the decay time of the scintillator. A window type discriminator with programmable lower and higher discriminator levels can be designed using comparators and digital logic circuits. A set of two scaler (counters) channels are required for each of photon energies of dual energy beam. Alternatively, a set of two existing discriminators and scalers arrangement can be used, one to collect the higher energy photons and another for collecting photons in entire beam. However, the window type discriminator would provide ease of spectrum matching both at 43keV and 100keV.

These developments of photon detection systems would help to reduce the scan times to the order of 10-20 seconds with better or at least the same precision and accuracy of the present TBD measurements. Such a system would produce a tremendous improvement DECT by decreasing the scan time and hence errors in dual energy results.

References

- Alvarez RE, Macovski A. Energy selective reconstructions in X-ray computed tomography. *Phys Med Biol* 1976; 21(5):733-744.
- Battista JJ, Bronskill MJ. Compton-scatter tissue densitometry: Calculation of single and multiple scattered photon fluences. *Phys Med Biol* 1978; 23:1-23.
- Bentzen SM, Hvid I, Jorgensen J. Mechanical strength of tibial trabecular bone evaluated by X-ray computed tomography. *J Biomechanics*, 1987; 20(8): 743-752
- Berninger WH, Redington RW. Dynamic computed tomography. *Radiology of skull and brain: Technical aspects of computed tomography*. ed by Newton TH, Potts DG. The C.V. Mosby Company, 1981; pp 4261-4285
- Bracewell RW. Strip integration in radio astronomy. *Aus J Phys*, 1956; 9: 198-217
- Brooks RA, Chiro GD. Beam hardening in X-ray reconstructive tomography. *Phys Med Biol* 1976; 21(3):390-398.
- Cameron JR, Mazess RB, Sorenson JA. Precision and accuracy of bone mineral determination by direct photon absorptiometry. *Inves Radiol* 1968; 3:141-150.
- Cameron JR, Sorenson J. Measurement of bone mineral in vivo: an improved method. *Science* 1963; 142:230-232.
- Cann CE. Quantitative CT for determination of mineral density: A Review. *Radiology* 1988; 166:509-522.
- Cann CE, Ganant HK. Precise measurement of vertebral mineral content using computed tomography. *J Comput Assist Tomogr* 1980; 4(4):493-500.
- Catto GRD, McIntosh JAR, Macleod M. Partial body neutron activation analysis in vivo: a new approach to the investigation of metabolic bone disease. *Phys Med Biol* 1973; 18:508-517

- Chuang K, Huang HK. A fast dual-energy computational method using isotransmission lines and table look-up. *Med Phys* 1987; 14(2):186-192.
- Ciarelli MJ, Golstein SA, Dickie D, Ku JL, Kapper M, Stanley J, Flynn MJ, Mathew LS. Experimental determination of the orthogonal mechanical properties, density and distribution of human trabecular bone from major metaphyseal regions utilizing material testing and computed tomography. *Trans. of Orthopaedic Research Society*, 1986; 11: 42
- Cormack AM. Representation of functions by its line integrals with some radiological applications. *J Appl Phys* 1963; 34:2722-2727
- Cormack AM. Representation of functions by its line integrals with some radiological applications-II. *J Appl Phys* 1964; 35:2908-2913
- Data specification manual: Charge sensitive pre-amplifier model RL-723. Rel-labs Inc.
- D'Amico DA, Contour detection in computed tomographic images of bone. Msc thesis, Department of Physics at U of A, 1986.
- Dequeker J. Problems in measuring the amount of bone: reproducibility, variability, sequential evaluation. In Meunier PJ, ed. *bone histomorphometry*. Toupouse, France: Soc Nouv Imprim Fourmé, 1917:19-37.
- Frost HM. Pathogenic mechanisms of the osteoporosis. *Current Concepts of Bone Fragility* 1986. pp329-361.
- Frost HM. Mechanical determinants of bone modeling. *Metab Bone Dis and Rel Res* 1982; 4:217-229.
- Frost HM. *The physiology of Cartilaginous, Fibrous and Bony Tissue*. Springfield, C C Thomas, 1972
- FUG Electronic GmbH, Nieder- Und Hochspannungs- Netzgeräte: Technische Unterlagen.
- Ganant HK, Boyd D. Quantitative bone mineral analysis using dual energy computed tomography. *Invest Radiol* 1977; 12:545-551.

- Garg A, Walker PS. The effect of the interface on the bone stresses beneath tibial components. *J Biomechanics*, 1986; 19(12):957-967
- Goodsitt MM, Rosenthal DI. Quantitative computed tomography scanning for measurement of bone and bone marrow fat content: A comparison of single- and dual-energy techniques using a solid synthetic phantom. *Invest Radiol* 1987; 22:799-810.
- Greitz T, Bergström M. Stereotactic computed tomography of the head. *Radiology of skull and brain: Technical aspects of computed tomography*. ed by Newton TH, Potts DG. The C.V. Mosby Company, 1981; pp 4286-4295
- Hamamatsu Technical Manual. Photomultiplier Tubes p1-32.
- Hangartner TN. Correction for scatter in computed tomography images of bone. *Med Phys* 1987; 14(3):335-340.
- Hangartner TN, Battista JJ, Overton TR. Performance evaluation of density measurements of axial and peripheral bone with X-ray and gamma-ray computed tomography. *Phys Med Biol* 1987; 32(11):1393-1406.
- Hangartner TN. Review: The radiological measurement of bone. *J of Canadian Association of Radiologists* 1986; 37:143-152.
- Hangartner TN, Overton TR. Variable resolution fan-beam CT scanner for peripheral bone evaluation. *J Comput Assist Tomogr* 1985; 9(3):612-613.
- Hangartner TN, Overton TR. Quantitative measurement of bone density using gamma-ray CT. *J Comput Assist Tomogr* 1982; 6(6):1156-1162.
- Herman GT. Correction for beam hardening in computed tomography. *Phys Med Biol* 1979; 24(1):81-106.
- Herman GT, Lakshminarayanan AV, Naparstek A. Convolution reconstruction techniques for divergent beams. *Comput Biol Med* 1976; 6:259-271.
- Hounsfield GN. Computerized transverse axial scanning (tomography): Part 1. Description of system. *Br J Radiol* 1973; 46:1016-1022.

- Jelinek J, Overton TR. Simulation of CT reconstruction artifacts associated with multiple-rotation fan-beam data collection. *Comput Radiol* 1986; 10(1):23-26.
- Jelinek J, Overton TR. Reordering schemes for multiple-rotation fan-beam CT scanner. *IEEE Trans Medi Imaging* 1985; MI-4(4):215-221
- John HE, Cunningham JR. *The Physics of Radiology*, 4th ed. Charles C Thomas, Publisher. Springfield, 1983; pp177. *ibid*; pp719-740
- Joseph PM, Spital RD. The exponential edge gradient effect in X-ray computed tomography. *Phys Med Biol* 1981; 26(3):473-487.
- Joseph PM. Artifacts in computed tomography. *Radiology of skull and brain: Technical aspects of computed tomography*. ed by Newton TH, Potts DG. The C.V. Mosby Company, 1981; pp 3956-3992
- Kennett TJ, Webber CE. Bone density measured by photon scattering. (II) Inherent sources of error. *Phys Med Biol* 1976; 21:770-780.
- Knoll F. *Radiation Detection and Measurement*. John Wiley and Sons Inc. 1979; pp95-102.
- Kohman TP. General method for determining coincidence corrections of counting instruments. U.S. Atomic Energy Commission, MDMC-905, 1945.
- Laval-Jeantet AM et al. Influence of vertebral fat content on quantitative CT density. *Radiology* 1986; 159:463-466.
- Laval-Jeantet AM et al. A post processing dual energy technique for vertebral CT densitometry. *J Comput Assist Tomogr* 1984; 8(6):1164-1167.
- LeCroy Research Systems: Technical data. Charge/Current pulse pre-amplifier -type TRA1000, 1978; pp1-7.
- Lehmann LA et al. Generalized image combinations in dual KVP digital radiography. *Med Phys* 1981; 8(5):659-667.
- Mazess RB. Error in measuring trabecular bone by computed tomography due to marrow and bone composition. *Calcif Tissue Int* 1983; 35:148-152.

- McBroom RJ, Hayes WC, Edwards WT, Goldberg RP, White AA. Prediction of vertebral body compressive fracture using computed tomography. *J. Bone Joint Surg*, 1985;67A(8): 1206-1213.
- McCracken DD, Dorn WS. Numerical methods and FORTRAN programming. John Wiley Press, New York, 1964. pp144-145.
- McDavid WD, Waggner RG, Payne WH, Dennis MJ. Correction for spectral artifacts in cross-sectional reconstruction from X-rays. *Med Phys* 1977; 4:54-57.
- McCullough EC. Computed tomography in radiation therapy treatment planning. *Radiology of skull and brain: Technical aspects of computed tomography*. ed by Newton TH, Potts DG. The C.V. Mosby Company, 1981; pp4301-4311.
- Müller A, Rügsegger P, Seitz P. Optimal CT settings for bone evaluations. *Phys Med Biol* 1985; 30(5):401-409.
- NE technology ltd. data manual on plastic scintillators.
- Nickoloff EL, Feldman F. Bone mineral assessment with dual energy computed tomography (CT) imaging. *Medical Imaging and Inst* 1985; SPIE 555:178-187.
- Parfitt AM. Bone remodeling in pathogenesis of osteoporosis. Bone and mineral research lab report. *Medical times*, November 1981; pp1-9.
- Parfitt AM and Kleerekoper M. The divalent ion homeostatic system: Physiology and metabolism of calcium, phosphorus, magnesium and bone. *In* Maxwell M and Kleeman CR (eds.) New York, McGraw-Hill, 1979, pp: 269-398
- Parfitt AM. Quantum concept of bone remodeling and turn over: Implications for pathogenesis of osteoporosis. *Calcif Tissue Int* 1979; 28:1-5 (Editorial).
- Peppler WW, Mazess RB. Total body bone mineral and lean body mass by dual-photon absorptiometry. I Theory and measurement procedure. *Calcif Tissue Res Int* 1981; 33:353-359.
- Peters TM, Lewitt RM. Computed tomography with fan-beam geometry. *J Comput Assist Tomogr* 1977; 1(4):429-436.

- Radon J. Ueber die Bestimmung von Funktionen durch ihre Integralwerte längs gewisser Mannigfaltigkeiten. Ber Verh Saechs Akad Wiss 1917; 69:262-277.
- Rao GU, Yoghmai I, Wist AO, Arora G. Systematic errors in bone-mineral measurements by quantitative computed tomography. Med Phys 1987; 14(1):62-69.
- Riggs BL, Seeman E, Hodgson SF, Taves DR, O'Fallen WM. Effect of fluoride/calcium regimen on vertebral fracture occurrence in post-menopausal osteoporosis: Comparison with conventional therapy. N Engl J Med 1982; 306:446-450.
- Rosenfeld A, Kak AC. Digital Picture Processing, 2nd Ed. Academic Press, New York, 1982; 2:138-145.
- Rüegsegger P, Hangartner TN, Keller HV, Hinderling T. Standardization of computed tomography images by means of a material-selective beam hardening correction. J Comput Assist Tomogr 1978; 2:184-188.
- Rüegsegger P, Elsassner U, Anliker M et al. Quantification of bone mineralization using computed tomography. Radiology 1976; 121:93-97.
- Rüegsegger P, Niederer P, Anliker M. An extension of classical bone mineral measurement. Ann Biomed Eng, 1974; 2:194-205
- Rutt B, Fenster A. Split-filter computed tomography: A simple technique for dual energy scanning. J Comput Assist Tomogr, 1980; 4(4):501-509.
- Schulz E et al. Bone density in the spine by CT and in the radius by photon absorption in osteoporosis. J Comput Assist Tomogr 1983; 7:555-556.
- Seitz P, Rüegsegger P. Fast contour detection algorithm for high precision quantitative CT. IEEE Trans Medi Imaging 1983; M1-2(3):136-141.
- Shepp LA, Logan BF. The Fourier reconstruction of a head section. IEEE Trans. Nucl. Sci. 1974; 21:21-43.
- Shimmins J, Anderson JB, Smith DA, Aitken M. The accuracy and reproducibility of bone mineral measurements in vivo. (a) The measurement of metacarpal mineralization using an X-ray generator. Clin Radiol 1972; 23:42-46.

- Sorenson JA, Mazess RB. Effect of fat on bone mineral measurements. In JR Cameron(ed): Proc Bone Measurement Conference. U.S. Atomic Energy Comm. Conf. 700515. 1970; pp255-262
- Stebler BG et al. Signal processing and data acquisition system for multielement germanium detectors. J Comput Assist Tomogr 1985; 9(3):610-611.
- Stockham CD. A simulation study of aliasing in computed tomography. Radiology 1979; 132:721-726.
- Vetter JR et al. Evaluation of prototype dual-energy computed tomography apparatus. II. Determination of vertebral mineral content. Med Phys 1986; 13(3):340-343.
- Webber CE, Kennett TJ. Bone density measured by photon scattering. (I) A system for clinical use. Phys Med Biol 1976; 21:760-769.
- Wells DM. Design, Implementation and Calibration of a specialized X-ray-CT scanner for bone evaluation. Msc. Thesis in department of Applied Sciences in Medicine at U of A, 1986.
- Wong CK, Huang HK. Calibration procedure in dual-energy scanning using the basis function technique. Med Phys 1983; 10(5):628-635.
- Woodard HQ. The composition of human cortical bone: Effect of age and some abnormalities. Clin Ortho 1964; 37:187-193.
- Yester MW, Barnes GT. Geometrical limitations of computed tomography (CT) scanner resolution. Proc. SPIE Appl Opt Instr in Medicine V1. 1977; (127):296-303.
- Zatz LM. General overview of computed tomography instrumentation. Radiology of skull and brain: Technical aspects of computed tomography . ed by Newton TH, Potts DG. The C.V. Mosby Company, 1981; pp 4025-4032.